

BRIDGING BETWEEN PLASMONICS AND SPINTRONICS
THE SPIN PLASMONS IN TOPOLOGICAL INSULATORS

by

Yong Wang

A dissertation submitted to the Faculty of the University of Delaware in partial fulfillment of the requirements for the degree of Doctor of Philosophy in Materials Science and Engineering

Summer 2020

© 2020 Yong Wang
All Rights Reserved

BRIDGING BETWEEN PLASMONICS AND SPINTRONICS
THE SPIN PLASMONS IN TOPOLOGICAL INSULATORS

by

Yong Wang

Approved: _____
Darrin Pochan, Ph.D.
Chair of the Department of Materials Science and Engineering

Approved: _____
Levi Thompson, Ph.D.
Dean of the College of Engineering

Approved: _____
Douglas J. Doren, Ph.D.
Interim Vice Provost for Graduate and Professional Education and
Dean of the Graduate College

I certify that I have read this dissertation and that in my opinion it meets the academic and professional standard required by the University as a dissertation for the degree of Doctor of Philosophy.

Signed:

Stephanie Law, Ph.D.
Professor in charge of dissertation

I certify that I have read this dissertation and that in my opinion it meets the academic and professional standard required by the University as a dissertation for the degree of Doctor of Philosophy.

Signed:

Matthew Doty, Ph.D.
Member of dissertation committee

I certify that I have read this dissertation and that in my opinion it meets the academic and professional standard required by the University as a dissertation for the degree of Doctor of Philosophy.

Signed:

Anderson Janotti, Ph.D.
Member of dissertation committee

I certify that I have read this dissertation and that in my opinion it meets the academic and professional standard required by the University as a dissertation for the degree of Doctor of Philosophy.

Signed:

John Xiao, Ph.D.
Member of dissertation committee

ACKNOWLEDGMENTS

I would like to express my deepest appreciation to my advisor Professor Stephanie Law, for her kind support of my Ph.D. research and dissertation. She is knowledgeable, elegant, considerate, and always willing to help, I would not have achieved so much without her insightful guidance throughout my Ph.D. career.

I would like to thank the rest members of my thesis committee: Professor Matthew F. Doty, Professor John Q. Xiao, and Professor Anderson Janotti. Special thanks to Professor Doty and Professor Xiao for their insightful suggestions in our collaborative research projects.

It is my pleasure to have worked with many outstanding colleagues who collaborated with me in many research projects. I would like to thank the members of the material growth facility (MGF): Professor Joshua M. O. Zide, Dr. Christopher Schuck, Dr. Theresa P. Ginley, Patrick Sohr, Yuejing Wang, Lauren McCabe, James Bork, Md Nazmul Alam, Zhengtianye Wang, Vishnuvardhan Mambakkam, Saadia Nasir, Wilder Acuna (Gonzalez), and Yongchen Liu. I will always remember the days when we worked together to maintain the MBE systems. I would like to thank Yang Wang, Dr. Tao Wang, Dr. Yu-sheng Ou, Hongshu Ke, Professor Tingyi Gu, Dr. Qiu Li, Dr. Tiantian Li, for their collaborative works in multiple research projects. Without them, my Ph.D. career would have been much less productive. I would like to thank other members of the Law research group: Dr. Desalegn Debu, Dr. Greeshma Chandan, Dr. Dongxia Wei, for their kind helps and valuable suggestions.

Many thanks go to my friends who have accompanied me through my Ph.D. career: Nicholas Valdes, Olivia George, Yuying Zhang, Vivek Subramanian, Chinmay Pawar, Jiayi Wang, Yukun Dong, and all.

Finally, but most importantly, I would like to express my deepest gratitude and love to my parents and my elder sister. I would not have gone this far without their unconditional support.

TABLE OF CONTENTS

LIST OF TABLES	viii
LIST OF FIGURES	ix
ABSTRACT	xv

Chapter

1	INTRODUCTION	1
1.1	Topological Insulators	3
1.2	Plasmons	9
1.2.1	Collective Oscillations of an Electron Gas	9
1.2.2	The Dirac Plasmons in TIs	11
1.2.3	The Spin Plasmons	13
1.3	An outline of this dissertation	15
2	GROWTH, FABRICATION AND CHARACTERIZATION TECHNIQUES	16
2.1	Molecular Beam Epitaxy	16
2.2	Nano-fabrication techniques	26
2.2.1	Lithography	27
2.2.2	Lift off	29
2.3	Characterization techniques	31
2.3.1	Structural characterization	31
2.3.2	Optical measurements	34
2.3.3	Transport measurements	37
2.4	Summary	39
3	THE GROWTH OF TOPOLOGICAL INSULATORS WITH MOLECULAR BEAM EPITAXY	41

3.1	The ternary alloy: $\text{Bi}_2(\text{Se}_{1-x}\text{Te}_x)_3$ (BST).....	43
3.1.1	The structural analysis of the epitaxial BST thin films	46
3.1.2	The exploration of the growth parameter space	49
3.1.3	The characterization of transport properties	52
3.2	The epitaxial growth of Bi_2Se_3 on a $(\text{Bi}_{1-x}\text{In}_x)_2\text{Se}_3$ (BIS) buffer layers ...	55
3.2.1	Co-deposition of BIS	56
3.2.2	The sequential growth for BIS	58
3.2.3	The characterization of indium content	61
3.2.4	BIS as a buffer layer	63
3.3	Summary.....	72
4	THE OBSERVATION OF DIRAC PLASMON POLARITONS IN TOPOLOGICAL INSULATORS	73
4.1	Optical properties of $(\text{Bi}_{1-x}\text{In}_x)_2\text{Se}_3$ thin films	77
4.1.1	Optical bandgaps	77
4.1.2	The simulation of permittivity in IR.....	83
4.2	The observation of the Dirac plasmon polaritons.....	90
4.3	Summary.....	102
5	THE SPIN PLASMONS	103
5.1	THz source.....	104
5.2	Magneto-optical Kerr effect (MOKE).....	106
5.3	Progress in the detection of spin plasmons.....	111
5.4	Summary.....	112
6	CONCLUSIONS AND FUTURE WORKS	113
	REFERENCES	116
	Appendix	
	FIGURE REPRINT PERMISSION	125

LIST OF TABLES

Table 3.1. Flux ratio during growth and resulting composition of samples shown in figure 3.4 and figure 3.5.	50
Table 3.2. Room temperature carrier mobility and sheet concentration of BST samples. Samples are arranged in the order of Bi_2Se_3 , near $\text{Bi}_2\text{Se}_2\text{Te}$, near Bi_2SeTe_2 , and Bi_2Te_3 . All samples are n-type.	53
Table 3.3. Film thickness, In content by growth rate and In content by RBS measurement.	61
Table 3.4. Growth parameters for all $\text{Bi}_2\text{Se}_3/\text{BIS}$ films, including sample name, sample number, seed layer type (none, co-deposition, or sequential deposition seed layer), substrate temperature during BIS buffer growth (T_{sub}), BIS buffer composition (x), room temperature Bi_2Se_3 mobility (μ), and room temperature Bi_2Se_3 sheet density (n_s). All films are n-type. We use an error bar of 5% for Hall mobility and 6% for Hall sheet concentration. The error range of each is determined by the mean deviation from the average among multiple measurements on the same film.	64
Table 4.1. Mean values and standard deviations of all the fitting parameters for all the samples.	88

LIST OF FIGURES

Figure 1.1. (a)-(c) The insulating state. (a) An atomic insulator. (b) A simple model insulating band structure. (d)-(f) The quantum Hall state. (d) The cyclotron motion of electrons. (e) The Landau levels, which may be viewed as a band structure. (c) and (f) Two surfaces which differ in their genus, g . (c) $g=0$ for the sphere and (f) $g=1$ for the donut. Figure used with permission from [21].	4
Figure 1.2. A schematic of the spin-polarized edge state conducting channels in a 2D topological insulator. Figure used with permission from [31].	5
Figure 1.3. A schematic of the band inversion theory for understanding the formation of TI band structures. Figure used with permission from [32].	6
Figure 1.4. The calculated band structure of Bi_2Se_3 showing the bulk band gap and the linear surface states. Figure used with permission from [33].	8
Figure 1.5. Crystal structure of tetradymite Bi_2Se_3 . (a) View from the a-b plane. (b) View from the c axis. Figure used with permission from [36].	8
Figure 1.6. A schematic of SPP with charge density oscillation and the electric field in the surrounding dielectric media.	11
Figure 1.7. Schematics of (a) optical mode and (b) acoustic mode for coupled Dirac plasmons. Figure used with permission from [32].	14
Figure 2.1. A schematic of an MBE system. Figure made by Dr. Theresa P. Ginley.	17
Figure 2.2. The Veeco GENxplor system.	19
Figure 2.3. A schematic of a typical RHEED measurement	20
Figure 2.4. A schematic of the three major growth modes. (a) The FM (layer-by-layer) mode; (b) The VW mode (island mode). (c) The SK mode. From top to bottom are the cases when growing the 1 st monolayer, the 2 nd monolayer and the 3 rd monolayer, respectively.	21

Figure 2.5. The reciprocal lattice (purple dots), the Ewald sphere (black circle), the wavevectors of the incident and diffracted electron beam (black arrows).....	23
Figure 2.6. (a) side view and (b) top view of the Laue condition of RHEED.....	24
Figure 2.7. Characteristic RHEED patterns of epitaxial Bi_2Se_3 when looking at the orientation of (a) $[1\ 1\ \bar{2}\ 0]$ and (b) $[2\ \bar{1}\ \bar{1}\ 0]$	25
Figure 2.8. Top view of a TI lattice showing the two major orientations that are observed in RHEED. Figure used with permission from [73].	26
Figure 2.9. A schematic of a typical lithography process.	29
Figure 2.10. SEM image of the samples (a) before liftoff and (b) after liftoff.	30
Figure 2.11. A typical XRD spectra of an MBE Bi_2Se_3 film. The peak around 42° is from the Al_2O_3 substrate.....	32
Figure 2.12. A typical AFM image of Bi_2Se_3 with a area of $2\mu\text{m} \times 2\mu\text{m}$. The color scale ranges from 0nm to 25nm.	33
Figure 2.13. A schematic of an FTIR instrument with a transmission measurement geometry.....	34
Figure 2.14. The FTIR transmission data (a) before Fourier transformation and (b) after Fourier transformation.	36
Figure 2.15. A schematic of the Hall measurement geometry.	37
Figure 2.16. The van der Pauw four-point probe geometry. The blue triangles in the corners are the contacts, and black lines are the wires.	38
Figure 3.1. Lattice constants of various substrates compared to lattice constants of binary TIs. The crystal phase is (111) for zincblende and cubic lattices and (0001) for wurtzite and hexagonal lattices. Figure used with permission from [36].	42

Figure 3.2. Lattice configuration of the proposed Bi_2SeTe_2 . (a) View along the a- b plane showing two quintuple layers (QLs). Tellurium preferentially occupies the outside sites (small dark blue atoms) while selenium preferentially occupies the middle site (small light blue atoms). Bismuth sits between (large gray atoms). (b) View along the c-axis showing the three-fold in-plane symmetry. Figure used with permission from [107].	44
Figure 3.3. The top part of the figure is the atomic-resolution STEM (white and gray) and the associated EDS (blue, red and green). The blue, red and green atoms are Bi, Te and Se atoms revealed by EDS, respectively. The bottom part of the figure is the DFT simulation. Figure used with permission from [106].	45
Figure 3.4. RHEED images of $\text{Bi}_2(\text{Se}_{0.8}\text{Te}_{0.2})_3$ films taken during the growth. (a) Diffraction pattern along $[1\ 0\ \bar{1}\ 0]$; (b) Diffraction pattern along $[\bar{1}\ \bar{1}\ 0]$.	46
Figure 3.5. The coupled theta-two theta scan spectra from $(10^\circ$ to $70^\circ)$ for the epitaxial BST samples with a selenium concentration from 0 to 100%, determined by the diffraction peak positions and Vegard's Law. All intensities are normalized, and data is offset for clarity. Figure used with permission from [107].	47
Figure 3.6. The coupled theta-two theta scan spectra from $(63^\circ$ to $70^\circ)$ for the same epitaxial BST samples as those in figure 3.4. Figure used with permission from [107].	48
Figure 3.7. XRD spectrum of samples grown with a fixed flux ratio and a variable substrate temperature. Figure used with permission from [107].	51
Figure 3.8. A typical RHEED image during the co-deposition growth of BIS with $x=0.5$.	56
Figure 3.9. The XRD spectra for BIS samples by co-deposition with an indium concentration from 0 to 1.	57
Figure 3.10. A schematic of a sequential growth process for BIS films.	59
Figure 3.11. RHEED images of In_2Se_3 growth on seed layers.	60
Figure 3.12. The XRD spectra for the BIS films grown with sequential method.	60

Figure 3.13. RBS data vs simulation with the three-layer approximation. Inset is the zoom in of the spectra to make the Se, In and Bi peak clear.....	62
Figure 3.14. Carrier density (filled symbols) and mobility (open symbols) for samples A (black square), B (black circle), and C (black triangle). Error bars are shown, but for many samples are smaller than the size of the symbol. AFM images are shown at top for samples A and C, as indicated. The AFM images are both $2 \times 2 \mu\text{m}$ and on a color scale of 0–40 nm. Figure used with permission from [126]......	65
Figure 3.15. AFM images of the 10QL seed layer after annealing (a), and 50nm 30% BIS buffers grown on the seed layer at 425°C (b), 375°C (c), and 325°C (d). All scans are $2 \times 2 \mu\text{m}$ and the color scales are shown at right for each image. Figure used with permission from [126]......	67
Figure 3.16. Carrier density (filled symbols) and mobility (open symbols) for samples D (red square), E (red circle), and F (red triangle). AFM images are shown at top for samples D, E, and F, as indicated. The AFM images are all $1 \times 1 \mu\text{m}$ and on a color scale of 0–25 nm. Figure used with permission from [126]......	69
Figure 3.17. Carrier density (filled symbols) and mobility (open symbols) for sample D (red square), C (black triangle), and G (green circle). AFM images are shown at top for samples D, C, and G, as indicated. The AFM images are all $1 \times 1 \mu\text{m}$ and on a color scale of 0–40 nm. Figure used with permission from [126]......	71
Figure 4.1. A schematic of the spin plasmon: a spin density fluctuation (green surface) and the transverse spin amplitude S (red arrows). The angles of the two incident pump beams (brown arrows and purple curves) are defined by θ and ϕ . \mathbf{q} is the grating vector required to compensate the mismatch between the plasmons and the light wavevector. Figure used with permission from [49]......	74
Figure 4.2. A schematic of a device for the excitation of Dirac plasmon polaritons. The black arrow is the incident light with the electric field (red curve and red arrows) polarized perpendicular to the grating couplers.	76
Figure 4.3. The absorption coefficients as a function of the energy of the light ranging across 1eV (visible) to 6eV (ultraviolet). x is the content of indium in the BIS alloys. Figure used with permission from [128]......	78
Figure 4.4. (a)-(j) The Tauc plots for all five samples with both $r=2$ (red lines) and $r=1/2$ (blue lines).	81

Figure 4.5. The direct and indirect bandgap as a function of indium concentration in the alloys extracted from the Tauc plots. Figure used with permission from [128].	82
Figure 4.6. (a) Reflection spectra for sample B ($x=0.32$) with TE polarization and (b) TM polarization. (c) Fitted curve for sample B with TE polarization and (d) TM polarization at different incident angles. Figure used with permission from [128].	84
Figure 4.7. The data (red line) and simulation results (blue line) of the 45° TE reflection of a substrate.	87
Figure 4.8. The fitted high frequency permittivity as a function of indium concentration. The black and red lines are the linear fittings of $\epsilon_{\infty,xy}$ and $\epsilon_{\infty,z}$, respectively. Figure used with permission from [128].	89
Figure 4.9. An SEM image of a typical sample with a grating period of 550nm.	92
Figure 4.10. The normalized extinction spectra for samples A-E.	93
Figure 4.11. The zoomed in of the extinction spectra for samples A-E in the range of 3-5 THz. Data are offset so each peak can be seen clearly. Colored arrows are the maxima of each spectra around the probable DPP frequency.	94
Figure 4.12. Extinction spectra for sample F-H.	95
Figure 4.13. Dispersion relation (wavevector q as a function of frequency) of data extracted from extinction spectra in figure 4.11(color dots), simulation results for coupled Dirac plasmons (gray line), and simulation results for 2D massive plasmons (orange line).	97
Figure 4.14. The extinction spectra for sample I (yellow line), J (green line) and K (blue line).	101
Figure 5.1. A schematic of the spin plasmon detection method.	104
Figure 5.2. A schematic of the THz emission setup.	105
Figure 5.3. A schematic showing the Kerr rotation angle θ_K of a light beam reflected from a surface with a magnetization \mathbf{M} .	107
Figure 5.4. A simplified schematic of the MOKE measurement setup.	108

Figure 5.5. Expected MOKE signal – delay time function assuming sinusoidal spin wave. (a) Scanning of the distance at a fixed time delay t_1 . (b) Scanning of the delay time at a fixed distance d_1 110

ABSTRACT

Conventionally, the research of plasmonics and spintronics share little in common due to different physics and applications. The connection of these two fields is seemingly promising in creating advanced devices involving both optical and spintronic applications. To date, there are still limited attempts in connecting the two fields. In this dissertation, we propose to excite and observe the spin plasmons in topological insulators, which is, theoretically, a perfect bridge between plasmonics and spintronics.

Topological insulators (TI) are a group of materials that have unique band structures: the surfaces show linearly dispersed bands, while the bulk shows normal conduction bands and valence bands. The carriers located in the surface states are spin-momentum locked, meaning the spin of the surface carriers are dependent on the direction of their motions. Plasmons are the collective oscillations of electrons, affecting the way how electrons in the materials interact with external electromagnetic waves. Thus, the optical property of a material is largely dependent on the plasmons in it. Due to the spin-momentum locking, the plasmons that are formed by TI surface carriers (known as the Dirac plasmons), are correlated electron density waves as well as spin density waves. These spin density waves are essentially spin plasmons. The direct experimental evidences of this prediction remain unveiled. Therefore, the ultimate goal of this dissertation is to experimentally reveal the charge density oscillations and spin density oscillations at the mean time.

This dissertation first demonstrates the optimization of the growth of TI Bi_2Se_3 with molecular beam epitaxy (MBE). A buffer layer of $(\text{Bi}_{1-x}\text{In}_x)_2\text{Se}_3$ between the substrates and the Bi_2Se_3 films are utilized to enhance the crystal quality of the films. We established an optimized growth procedure for growing high quality $(\text{Bi}_{1-x}\text{In}_x)_2\text{Se}_3$ buffer layers. The TI films grown with the enhanced buffer layer show a sheet carrier density down to $\sim 1 \times 10^{13} \text{ cm}^{-2}$, decreased by a factor of 1/2 compared with the Bi_2Se_3 films grown without the buffer layer. The optical properties of BIS, including the optical bandgaps and the permittivity in the IR range, were also characterized for further analysis of the plasmons from the devices created with BIS.

A structure of $\text{BIS}(5\text{nm})/\text{Bi}_2\text{Se}_3(50\text{nm})/\text{BIS}(50\text{nm})/\text{sapphire}$ substrate was grown with the optimized growth procedure for the excitations of TI Dirac plasmons. Linear gold grating couplers with various periodicities (400nm- 700nm) were fabricated to enable the excitation of propagating Dirac plasmons. TM extinction spectra taken by Fourier transform IR spectroscopy (FTIR) showed a series of plasmonic absorption peaks shifting with the grating periodicity. The plasmonic absorptions were reported to be located in the Terahertz (THz) range. Simulation showed a good agreement between the data and the theoretical dispersion relation of the TI Dirac plasmons.

This dissertation proposed a possible method to observe the propagating spin plasmons using a THz-pump IR-probe method with a magneto-optical Kerr effect (MOKE) system. The direct observation of the spin plasmons were not achieved due to the limitations of the time resolution and the low signal of the plasmonic responses. Future works can still be applied in this direction as we refine the quality of the devices, and also the time resolution of MOKE system.

Chapter 1

INTRODUCTION

Nowadays, plasmonic and spintronic devices are playing significant roles in our lives in a variety of ways. Conventionally, plasmonics and spintronics have very little in common, showing different physics and different applications.

It has been reported that specially designed plasmonic devices can be used to guide and confine light[1]–[3], leading to better optical detectors. The plasmons in many novel materials like graphene and some metamaterials[4]–[6] have oscillation frequencies in the terahertz (THz) range, which is relatively unexplored. THz is the frequency region in which molecular resonances are located, the absorption spectra of THz exhibit distinct signatures for many substances such as water vapor, DNA, biofuel, and explosives[7]. While being able to penetrate many material systems, THz causes no known harm to the human body and the materials being examined as opposed to the X-ray. These advantages make THz a particularly attractive characterization tool in the areas of automotive, food, energy, pharmaceuticals and medical diagnosis[8]. The study of THz plasmonics broadens our utilization of this technologically important spectrum.

Research in spintronics, however, mostly aims to improve memory and storage devices in terms of size and energy efficiency[9]. The discovery of Giant Magneto-Resistance (GMR)[10], [11] had led to the emergence of magnetic disk drives. Recent progress in the magneto-resistive random access memory (MRAM) combined with the spin-moment-transfer effect (SMT-MRAM) had brought the memory unit scales down

to ~30nm[9], [12]. The frontier of modern day spintronics research focuses largely on topics like superconducting[13], molecular spintronics for small-scale memory and computation devices[14]. The distinct physics and applications have traditionally kept spintronics and plasmonics unrelated. People have reported the generation of spin currents with surface plasmons by making metal nanoparticles/ferromagnet heterostructures[15], but the number of similar studies is still limited.

Plasmons are the collective oscillations of the electron density. When light travels into a material, the electrons in the material will be driven by the electric field of the light and start to oscillate, resulting in a plasmon polariton[16]. More interestingly, a spin polarization oscillation can also be generated by external electric field in materials that have large spin-orbit coupling (SOC). That leads to new plasmonic oscillations: the spin plasmon polaritons[17]–[19]. One can imagine that the existence of spin plasmons will immediately connect the plasmonics and spintronics together, making it possible for lots of new physics and applications. However, due to the inconspicuousness of the effects and the limitations of the detection techniques, these theoretical predictions were not proved experimentally. Therefore, plasmons are conventionally not considered spin polarized. This remains unchallenged until the discovery of topological insulators (TIs).

After many years of searching for a system with the quantum spin Hall effect, scientists predicted and eventually discovered a group of materials that have unique band structures: the surface bands are linearly dispersed, while the bulk exhibits a normal bandgap. Moreover, the electrons on the surfaces are spin-momentum locked, which means that the spin of the electrons is determined by the direction of motion[20], [21]. This novel material is called a topological insulator (TI). TIs have

drawn a lot of attention since they opened up a whole new physics frontier, resulting in many unprecedented devices with an incredible efficiency[22], [23]. For more information about TIs, please see chapter 1.1. In theory, the plasmons on TI surfaces are simultaneously charge density waves and spin density waves[24], [25]. That is why we call them spin plasmons. Chapter 1.2 provides a more detailed description of the spin plasmons.

Based on the properties of the spin plasmons, we can conclude that the spin plasmons intrinsically provide a bridge between plasmonics and spintronics. Therefore, the observation of the spin plasmons will not only complete our understandings of the TI plasmons, but also open up the possibilities to devices with both terahertz responses as well as memory and computing abilities. Motivated by the significance of the spin plasmons, this dissertation will mainly focus on the growth and characterization of TIs, and the methods to excite and detect spin plasmons in TIs.

1.1 Topological Insulators

The discovery of topological insulators stems from the study of the integer quantum hall effect (IQHE), which occurs when electrons confined to two dimensions are placed in a strong magnetic field[26]. Under low temperatures and strong magnetic field, the motions of the electrons in the 2D electron gas can be seen as local cyclotron motions. This cyclotron motion is quantized with leveled frequencies, leading to quantized conductance. Moreover, the cyclotron motion of the electrons also results in an edge conduction in such a system. In pursuing the difference between the quantum hall states and the normal insulators, the idea of topology was introduced[27]. Gapped band structures can be classified topologically with a characteristic invariant called the Chern invariant $n \in Z$ (Z denotes the integers)[28]. The Chern number n that

distinguishes the two type of states is a topological invariant similar to the genus. Figure 1.1 demonstrates the topology difference of the normal insulator states and quantum hall states.

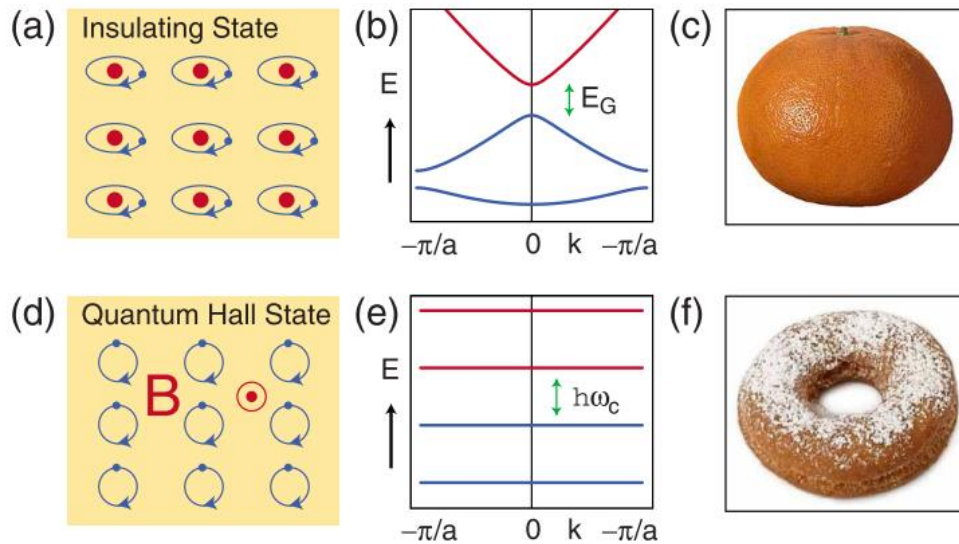


Figure 1.1. (a)-(c) The insulating state. (a) An atomic insulator. (b) A simple model insulating band structure. (d)-(f) The quantum Hall state. (d) The cyclotron motion of electrons. (e) The Landau levels, which may be viewed as a band structure. (c) and (f) Two surfaces which differ in their genus, g . (c) $g=0$ for the sphere and (f) $g=1$ for the donut. Figure used with permission from [21].

In the studies of the quantum hall effect, people predicted a type of material which has intrinsically quantized surface states similar to QHE. They were theorized in graphene[29], 2D semiconductor systems with a strain gradient[20], and then HgTe quantum wells[30]. They are called the quantum spin hall insulator, or 2D topological insulators. Due to the spin-orbit-coupling, the edge states of a 2D topological insulator become spin polarized while traveling in different directions. Further experiments

proved the existence of topological states of the HgTe/HgCdTe quantum wells[31]. Figure 1.2 shows the schematic of the spin-polarized edge states in a 2D topological insulator.

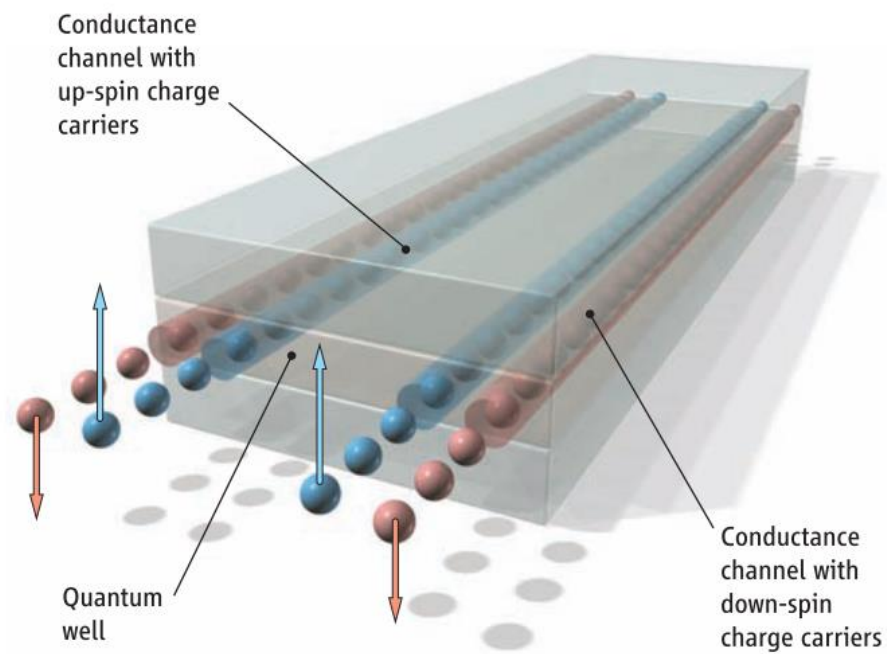


Figure 1.2. A schematic of the spin-polarized edge state conducting channels in a 2D topological insulator. Figure used with permission from [31].

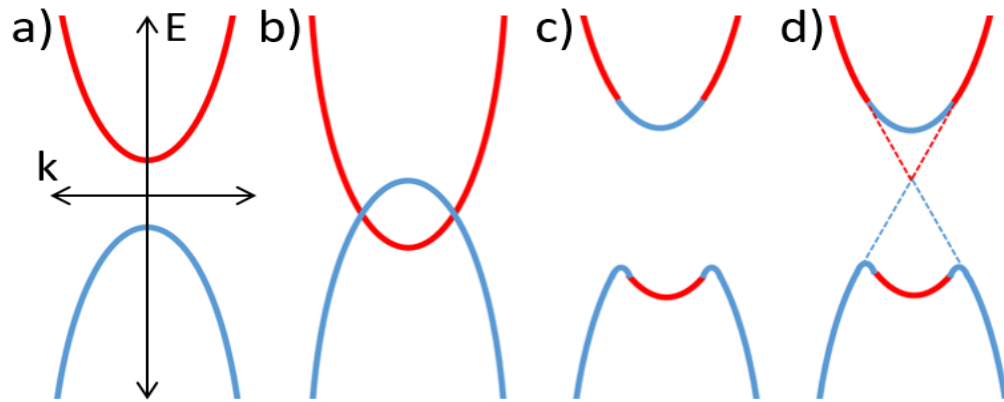


Figure 1.3. A schematic of the band inversion theory for understanding the formation of TI band structures. Figure used permission from [32].

The band structure of TIs can be understood more intuitively by a ‘band inversion’ theory[33]. A schematic of this band inversion theory is shown in figure 1.3. In the materials where the conduction band and valence band have opposite parities (Figure. 1.3(a), the conduction band is marked in red and valence band marked in blue), the energy splitting caused by the strong spin orbital coupling closed the band gap (Figure. 1.3(b)). This is where the so called ‘band inversion’ occurs. As a result, the band structure of TIs then deforms into a structure where the bottom of the conduction band partly preserves the parity of the valence band, and vice versa (Figure. 1.3(c)). At the surface of TI where the topological invariants are different on the two sides, the connection between the bottom of the conduction band and the top of the valence band shows up as the linear surface bands (Figure. 1.3(d)). Based on the ‘band inversion’ theory, it is not hard to get the criterion for the formation of TIs: 1) semiconductors with relatively small band gap and 2) large spin-orbital-coupling

effects. This leads us to heavy metal composites, which turns out to be the correct direction in later research.

The further efforts in searching of TIs had led to the emergence of the 3D topological insulators: first the $\text{Bi}_x\text{Sb}_{1-x}$ [34], and later the bismuth/antimony chalcogenides ($\text{Bi}_2\text{Se}_3/\text{Bi}_2\text{Te}_3/\text{Sb}_2\text{Te}_3$, and their alloys)[33], [35]. Since then, a lot of efforts have been put into the study of the newly identified 3D topological insulators, leading to a great enhancement in the understanding of the band structures as well as the crystal structures of these 3D TIs.

Among all these 3D TIs, Bi_2Se_3 draw the most attention mainly for three reasons: 1) it has a relatively large band gap of 0.3eV; 2) the Dirac cone is centered at the Γ point; 3) the Dirac point is not buried in the valance band[33]. These features made Bi_2Se_3 more tunable and controllable than the other species. Figure 1.4 shows the calculated band structure of Bi_2Se_3 .

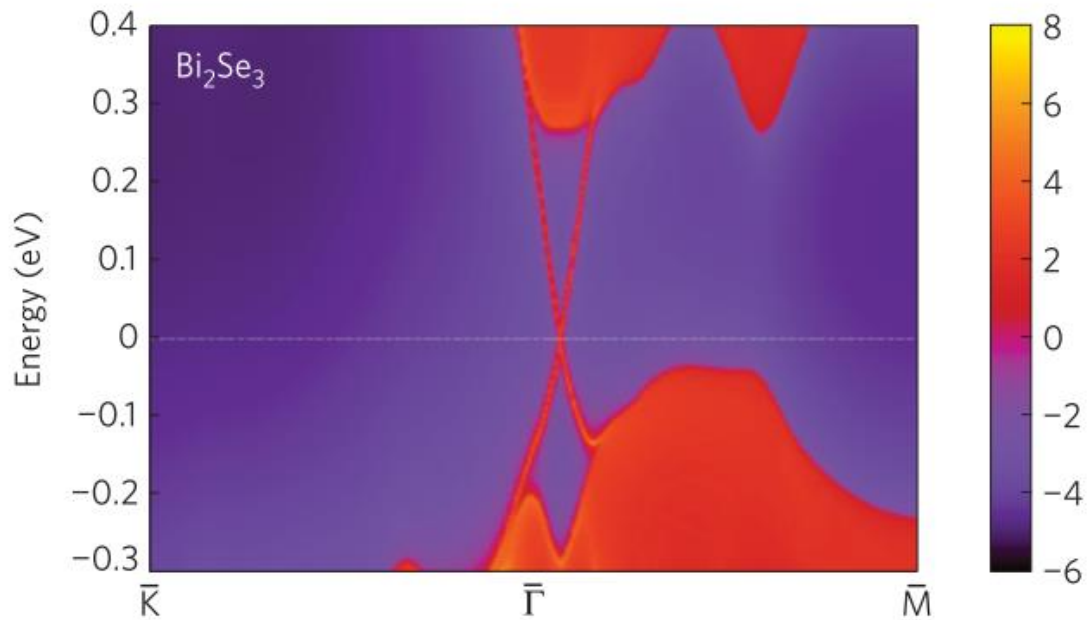


Figure 1.4. The calculated band structure of Bi_2Se_3 showing the bulk band gap and the linear surface states. Figure used with permission from [33]

The 3D TIs, bismuth/antimony chalcogenides, all share similar crystal structures: the tetradymite structure. The crystal structure of tetradymite Bi_2Se_3 is demonstrated in figure 1.5. In such structures, the five atomic layers of Se1-Bi-Se2-Bi-Se1 are chemically bonded into a unit called a ‘quintuple layer (QL)’. Each QL is $\sim 1\text{nm}$. 2 QLs are shown in figure 1.5(a) viewing from the a-b plane. The selenium atoms at the top and bottom of a QL is noted Se1, and the selenium atom at the center of a QL is noted Se2. This is to distinguish the two type of selenium atoms since they are under different chemical circumstances. Figure 1.5(b) shows the configurations of the atoms viewing from the c direction. The crystal is then formed by the QLs stacking with van der Waals interactions.

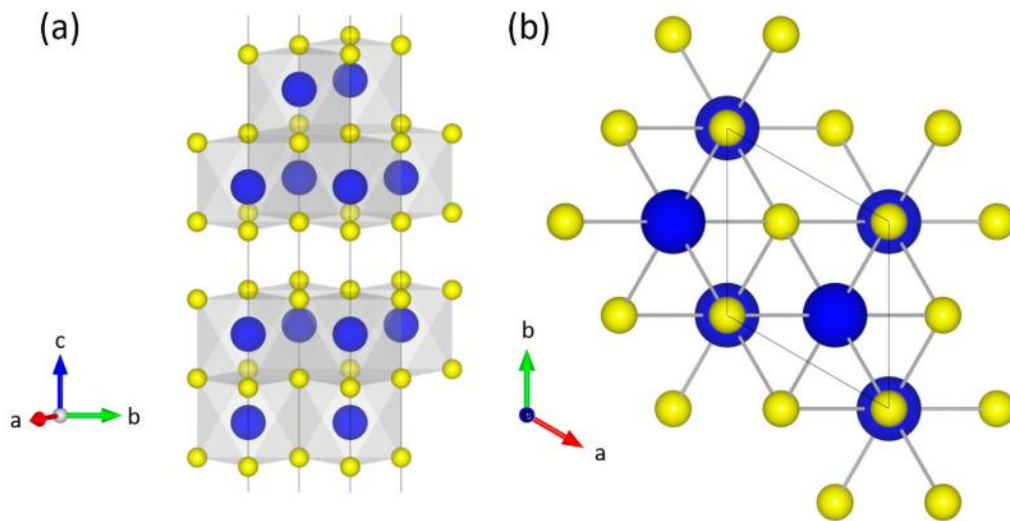


Figure 1.5. Crystal structure of tetradymite Bi_2Se_3 . (a) View from the a-b plane. (b) View from the c axis. Figure used with permission from [36].

The unique properties of TIs have made TIs popular in many research topics. The major topic of this dissertation is the plasmons in TIs. We will cover some basic knowledge of plasmons in the next section.

1.2 Plasmons

1.2.1 Collective Oscillations of an Electron Gas

The plasmons are first proposed by D. Pines and D. Bohm in 1952 when analyzing the behavior of the electrons in an electron gas[37]–[39]. The electron density fluctuation in an electron gas was decomposed into a short-range random motion due to the thermal energy, and a long-range collective oscillation caused by the joint coulomb potential from surrounding electron gas. The quanta of these collective oscillations were then called ‘plasmons’.

Using the free electron model, the plasma frequency, ω_p , of an electron gas can be easily approximated with the electron density n , the electron charge e , the electron mass m , and free space permittivity ϵ_0 :

$$\omega_p = \sqrt{\frac{ne^2}{m\epsilon_0}} \quad \text{Eq. 1.1}$$

The oscillation of the electrons play a large role in the optical properties of many materials. The light with a frequency below the plasma frequency will be reflected by the material due to the screening of the electric field. On the contrary, the light with a frequency higher than the plasma frequency will be transmitted since the electrons in the material cannot respond fast enough. This explains many phenomena in our lives. For example, most metals are shiny to human eyes because the plasma

frequencies of those metals are in the ultraviolet, making them reflective in the visible range.

Surface plasmons are those plasmons that are confined to surfaces, for example, nano metal particles embedded in a dielectric media or a continuous metal-dielectric interface. They interact strongly with the light resulting in a polariton[40]. There are many forms of polaritons depending on the distribution of the metal and dielectric material. Here we mainly focus on the Surface Plasmon Polariton (SPP), which comes in a continuous metal-dielectric interface. The SPPs are propagating charge density waves with electric field exponentially decays into the dielectric media, which means that SPPs can be highly concentrated at the interface. Figure 1.6 shows the schematic of SPP with the charge density oscillation and the electric field in the surrounding dielectric media. The green curves with arrows are the electric field of the SPP along the interface. The pink curve represents the evanescent wave that exponentially decays into the dielectric media.

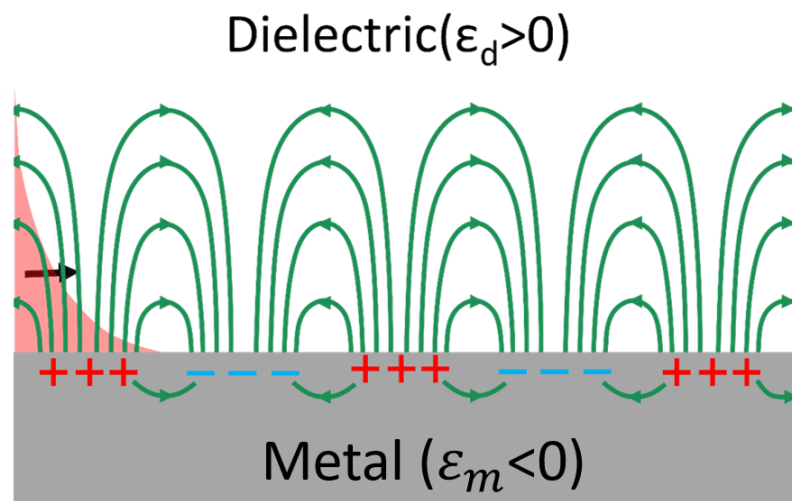


Figure 1.6. A schematic of SPP with charge density oscillation and the electric field in the surrounding dielectric media..

The resonance frequency of plasmons is dependent on the properties of the material where the plasmons reside. Therefore, a change of the absorption frequency and intensity carries information of the material and the environment[41]. This makes the plasmonic materials highly applicable for sensing. Furthermore, the high frequency (THz and higher) of the plasmonic oscillation makes the plasmons also promising for conducting information with low loss, leading to computing applications[42].

1.2.2 The Dirac Plasmons in TIs

The Dirac plasmons are the collective oscillations of Dirac electrons, which can be found in a Dirac system like graphene or topological insulator surface states[25]. The Dirac carriers are massless as opposed to the massive electrons in a normal material, making the Dirac plasmons behave differently from the normal plasmons. Then the following question we would ask is that: what are the differences between different types of plasmons and how do we quantify them?

A characteristic way to describe the plasmons is the frequency (ω_p)-momentum (q) relation, or the dispersion relation. For examples, Eq. 1.2 and 1.3 show the dispersion relation for 2D massive plasmons and 2D Dirac plasmons, respectively.

$$\omega_{massive}^2 = \frac{e^2}{4\epsilon_r\epsilon_0} \frac{n_M}{m^*} q \quad \text{Eq. 1.2}$$

n_M is the 2D carrier density and m^* the effective mass of the electron in the 2D electron gas.

$$\omega_{Dirac}^2 = \frac{e^2}{4\epsilon_T\epsilon_0} \frac{v_F\sqrt{2\pi n_D}}{h} q \quad \text{Eq. 1.3}$$

v_F is the fermi velocity of the Dirac carriers, n_D the density of the Dirac carriers. From the equations we can see that, plasmon frequencies for both 2D massive electrons and Dirac carriers are proportional to \sqrt{q} . The 2D massive plasmon frequency is proportional to \sqrt{n} , while the Dirac plasmon frequency is proportional to $n^{1/4}$.

When it comes to the TIs, things get even more complicated. The first part of the complexity comes from the coupling between the top and bottom surfaces of the TIs. The wavelength of the Dirac plasmons in TI surfaces is in the scale of hundreds of micrometers, a lot longer than the thickness of TIs (100nm or below). In this case, the incident light will interact with both interfaces, resulting in the coupled Dirac plasmon modes.

Theoretical works had point out that the coupling of the TI surfaces had caused the Dirac plasmons to be splitted into an optical mode (ω_+) and an acoustic mode (ω_-), as shown in Eq. 1.4 and 1.5[25], [43]–[45].

$$\omega_+^2 = \frac{e^2}{4\epsilon_T\epsilon_0} \frac{v_F\sqrt{2\pi n_D}}{h} \frac{q}{\epsilon_T + \epsilon_B + qd\epsilon_{TI}} \quad \text{Eq. 1.4}$$

$$\omega_-^2 = \frac{2\epsilon_0\epsilon_{TI}h v_F + e^2\sqrt{2\pi n_D}d}{\sqrt{4\epsilon_0^2\epsilon_{TI}^2h^2v_F^2 + 2\epsilon_0\epsilon_{TI}e^2\sqrt{2\pi n_D}d}} q^2 \quad \text{Eq. 1.5}$$

ϵ_T is the permittivity of the material on top of the TI, ϵ_B the permittivity of the material below the TI, d the thickness of TI and ϵ_{TI} the permittivity of TI. This energy splitting caused by the interaction between the two plasmon waves is similar to that of the coupling between the wavefunctions of two quantum wells.

The optical mode consists of electron density waves traveling in phase, making it permitted for optical excitations. The acoustic mode, however, consists of electron

density waves traveling out of phase, making it prohibited from optical excitation. Later experiments on TI Dirac plasmons had proven that the coupled Dirac plasmon model worked well with the data from optical measurement[46]–[48].

The second part of the complexity comes from the spin-momentum-locking of the electron in TI surfaces. This part of the problem will be described in the next section.

1.2.3 The Spin Plasmons

As mentioned previously, it has been predicted that in a system where spin orbit coupling is significant, the spin degree of freedom shows up in the interactions between electrons and external electric field. This leads to new plasmonic oscillations: the spin plasmon polaritons[17]–[19]. However, in III-V semiconductors where spin plasmons are originally analyzed, the effects are too small to be experimentally observed. Therefore, plasmons are conventionally not considered spin polarized.

After the discovery of the TIs, the idea of a spin plasmon comes back to our mind. In TIs, the electron spin is intrinsically correlated with the electron motion. It is fairly natural to conclude that the collective oscillations of the TI surface electrons are correlated with spin oscillations. This draws our attention to the spin plasmons for that the high oscillation frequency and spin polarization combined will give rise to a new generation of communicating and computing applications, which may be far beyond our imagination.

From previous discussions, we know that the Dirac plasmons in TIs are derived to be coupled, and an optical mode and an acoustic mode are distinguished due to the coupling. Given the spin-momentum-locking of the TI surface electrons, one can immediately realize that the charge density waves are correlated with spin

density waves. The schematics for the optical and acoustic modes of TI Dirac plasmons are shown in Figure 1.7. The yellow curves are the charge density waves, and the purple arrows are the spin density waves. The optical mode is a charge-like mode where the charge density oscillation travels in phase, but the spin density oscillation travels out of phase, and vice versa for the acoustic mode.

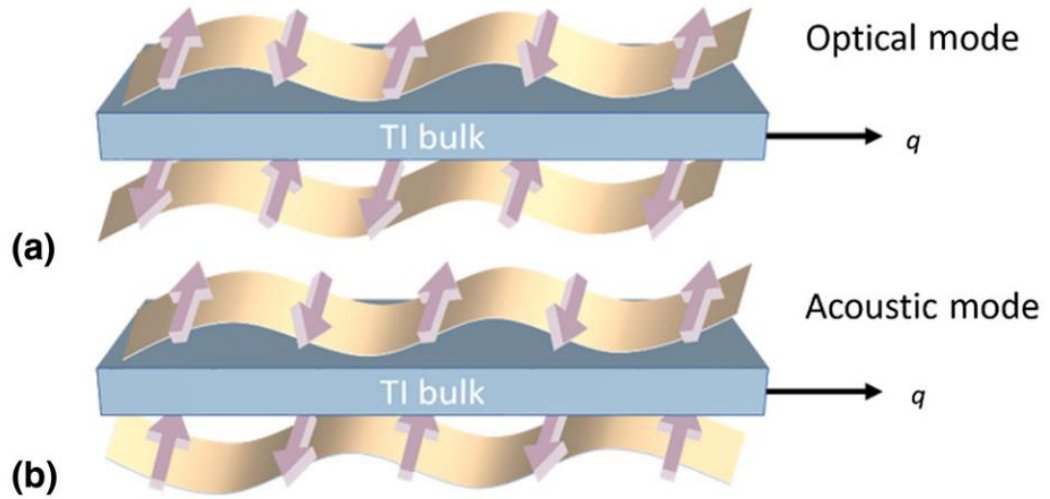


Figure 1.7. Schematics of (a) optical mode and (b) acoustic mode for coupled Dirac plasmons. Figure used with permission from [32].

In the early theoretical works of spin plasmons in TIs, multiple beams of circular polarized light are needed to launch the alternating spin oscillations[49]. However, the analysis of the Dirac plasmon shows that, by exciting a charge density wave with an incident light, we will be able to excite a spin plasmon as well.

1.3 An outline of this dissertation

So far, we have introduced the motivation in studying the spin plasmons and covered some basic knowledge that helps us understand the spin plasmons in topological insulators. In the next chapter, I will briefly describe the techniques that are used in this dissertation for material growths, device fabrications and characterizations. Chapter 3 demonstrates the optimization of the material growth process with molecular beam epitaxy (MBE), laying the foundation for the fabrication of the plasmonic devices. Chapter 4 focuses on the excitation and observation of the propagating Dirac plasmons, which is a prerequisite for direct observations of the spin plasmons in TIs. Chapter 5 shows some attempts to detect the spin plasmons with a magneto-optical Kerr effect (MOKE) system, along with some improving methods that can be carried out in the future.

Chapter 2

GROWTH, FABRICATION AND CHARACTERIZATION TECHNIQUES

In the last chapter, we briefly introduced the motivation of this dissertation and some basic knowledge in understanding the spin plasmons in topological insulators. This chapter will demonstrate the techniques that are used in this dissertation for the growths, fabrications and characterizations.

2.1 Molecular Beam Epitaxy

The materials that will be discussed in this dissertation, bismuth/indium chalcogenides, are all grown by molecular beam epitaxy (MBE). MBE is a popular tool in growing thin films with high crystal quality[50]. MBE can be seen as an upgraded version of vacuum evaporation in which directed molecular beams impinge on a heated substrate under ultra-high vacuum (UHV, $<10^{-9}$ torr) conditions[51]. A schematic of an MBE system is shown in figure 2.1.

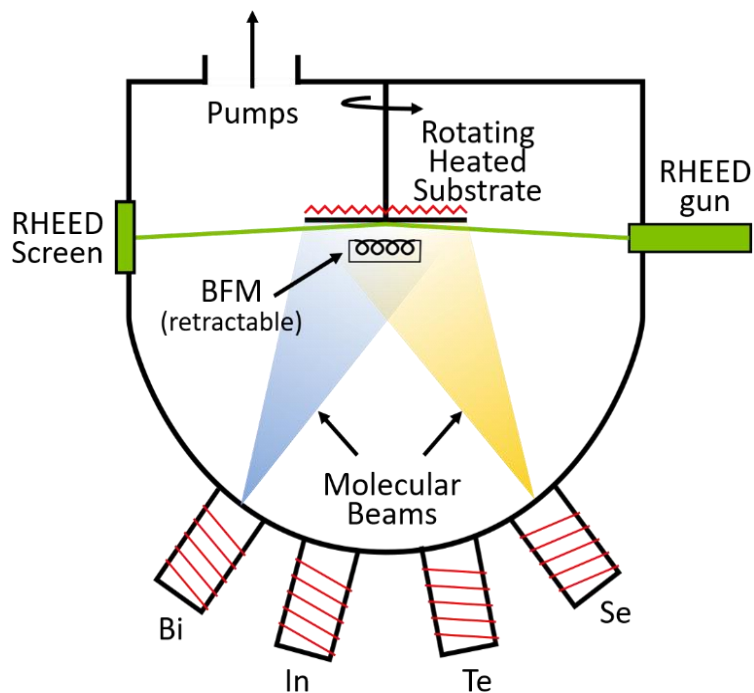


Figure 2.1. A schematic of an MBE system. Figure made by Dr. Thereasa P. Ginley.

The MBE system that was used for this dissertation is based on a three chamber (a growth chamber, a buffer chamber, and a load lock chamber) stainless steel UHV system. The UHV is ensured by an ionization pump and a cryopump connected to the growth chamber. The Knudsen effusion cells are used for bismuth source and indium source, in which the inner crucibles are made of pyrolytic boron nitride. The Knudsen effusion cell was developed by Martin Knudsen that are later widely used in material growth systems including MBE. A typical Knudsen cell contains a crucible, heating filaments, water cooling system, heat shields, and an orifice shutter. The valved-cracker cells are used for selenium and tellurium sources. The cracking zone of a cracker cell heats the selenium or tellurium to a high temperature, typically 900°C for Se and 1000°C for tellurium, to break the large

molecules into smaller species, which will be easier to react with bismuth or indium molecules. The usage of a cracking selenium cell is proved to enhance the crystal quality of the grown Bi_2Se_3 [52].

The beam fluxes of a molecular flow coming out of a Knudsen cells are determined by the cell temperatures

$$J_i = \frac{ap_i}{\pi d^2 \sqrt{2\pi m_i kT}} \cos\theta \quad \text{Eq. 2.1}$$

where J_i is the flux per unit area at a distance d from the source, which has an area of a . The source atom has a mass of m_i , and a vapor pressure of p_i at temperature T . θ is the angle between the beam and the substrate surface normal. The growth rate of the materials is directly proportional to the beam flux of the source materials. Thus, a precise monitor of the growth rate is enabled by a beam flux monitor (BFM), which is integrated in the MBE system as shown in Figure 2.1. The BFM is essentially an ionization gauge that ionizes, collects and then counts the molecules moving around it. The BFM signals are reported in the form of currents, and then transformed into pressure (torr) by calibration with N_2 gas. The typical growth rate for TIs are $\sim 0.8\text{nm}/\text{min}$.

The advantages of MBE make it a popular tool in growing III-V semiconductors since its invention in the 1970s. Typical MBE grown III-V semiconductors are arsenides (GaAs , InAs , AlAs , etc.)[53], [54], antimonides (GaSb , InSb , AlSb , etc.)[55], nitrides (GaN , AlN , etc.)[56] and phosphites(InP , etc.)[57]. Unsurprisingly, MBE became popular in the growth of many other materials where the crystal quality and the controllability of the growth are important, including oxides[58]–[60], group IV semiconductors(Si , Ge)[61], transition metal chalcogenides(MoS_2 , WSe_2 , etc.)[62], [63], and TIs(Bi_2Se_3 , Bi_2Te_3 and Sb_2Te_3)[64].

Figure 2.2 shows a picture of the MBE that is used for this dissertation, a dedicated Veeco GENxplor system.



Figure 2.2. The Veeco GENxplor system.

Other analytic tools that are integrated in the chamber include a mass spectrometer for residual gas analysis (RGA) and a reflection high energy electron diffraction (RHEED) system. RGA is used to analyze the species of the gas molecules in the chamber. Abnormal molecule species found in RGA scans could indicate a leak of the chamber. RHEED is designated for the in-situ analysis of the surface quality of the films. A high-energy electron beam (15keV) is incident to the growth surface at a very shallow angle and gets diffracted from the growth surface. The diffraction patterns of the electrons demonstrate the crystallinity information of the surface of the

sample. Figure 2.3 demonstrates a schematic of a typical RHEED measurement. A detailed description of the RHEED analysis is covered later in the chapter.

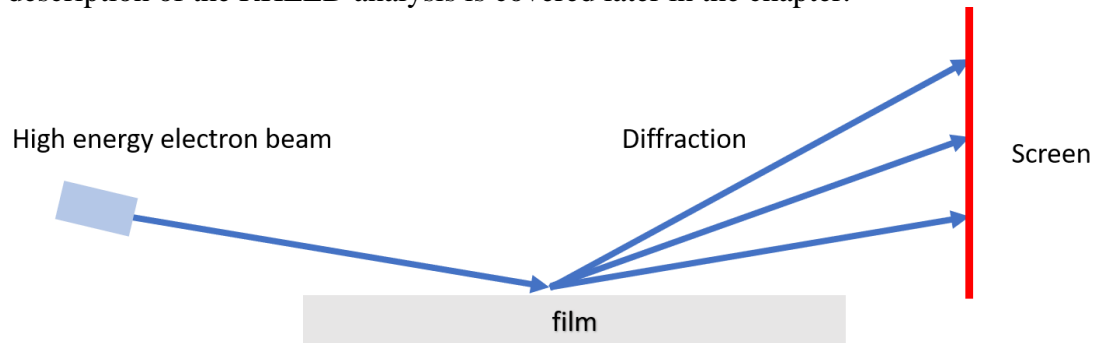


Figure 2.3. A schematic of a typical RHEED measurement

The growth mechanism

When molecules from the cells join together at the substrate and react, there are many ways that a film can be formed. Depending on the mechanism of the film formation, the MBE growths can be differentiated into several modes:

The **Frank-van der Merwe (FM)** mode, or the layer-by-layer mode. In an FM mode growth, the adatoms preferably attach to the surface sites, resulting in atomically smooth, fully formed layers. A complete film forms prior to the growth of a new layer[65], [66]. Many of the III-V semiconductor growths on lattice matched substrates are layer-by-layer growths.

The **Volmer-Weber (VW)** mode, or island mode. Adatom-adatom interactions are stronger than those of the adatom with the surface, leading to the formation of three-dimensional adatom clusters or islands[66]. VW growth modes are usually seen in group IV (Si/Ge) growths[67].

The **Stranski–Krastanov (SK)** mode. The SK mode is a combination of the layer-by-layer and island growth. The transition between the two regime is dependent on many factors, such as the film thickness, the surface energies and lattice mismatch, etc[68]. The growth of InGaAs on GaAs usually fall into this regime as islands form due to the strains of the lattices after the initial FM growth. SK growth modes are widely found in fabricating quantum dots[69].

A schematic for the three major growth modes are shown in figure 2.4.

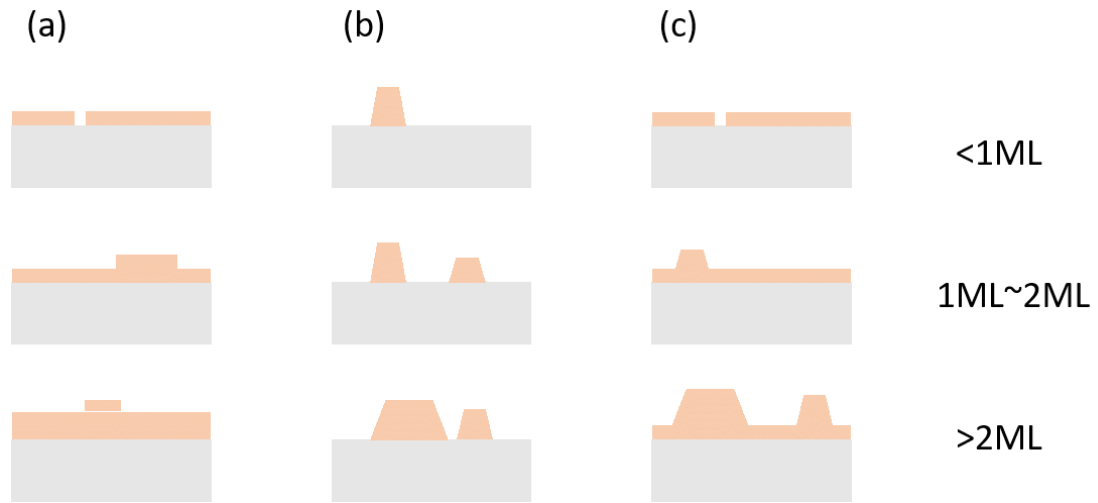


Figure 2.4. A schematic of the three major growth modes. (a) The FM (layer-by-layer) mode; (b) The VW mode (island mode). (c) The SK mode. From top to bottom are the cases when growing the 1st monolayer, the 2nd monolayer and the 3rd monolayer, respectively.

Most of the growth of conventional III-V semiconductors fall into these three major growth modes, with transitions from one to another due to the change of growth parameters. In the year of 1984, Atsushi Koma et al. demonstrated a new type of epitaxial growth for NbSe₂ films on MoS₂, and selenium on cleaved bulk crystals of

tellurium, and called this technique ‘**van der Waals epitaxy**’[70]. As opposed to conventional semiconductors, van der Waals materials do not have dangling bonds on the surface, leading to a drastically different growth mechanism. Since the van der Waals bonds between the film and the substrate are weak, people had believed that when the epitaxial layer is deposited on the lattice mismatched substrates, it immediately grows unstrained[71]. Given the van der Waals bonded crystal structure as described in the previous chapter, the epitaxial growth of TIs falls into this regime.

A thorough discussion on the epitaxial growth of TIs can be found in the next chapter.

RHEED analysis

RHEED is one of the most important analysis methods with epitaxial growth since the crystal structure of the surface can be observed as growing. The principle of a RHEED analysis is the electron diffraction off the surface of the sample with a very small penetration depth at a glancing angle. The diffraction happens when the Bragg condition is met

$$2d\sin\theta = n\lambda \quad \text{Eq. 2.2}$$

where d is the spacing between the crystal planes, θ the incident angle, n an integer number, and λ the wavelength of the electron wave.

The Bragg condition is equivalent to the Laue condition when we think of the reciprocal lattice

$$k_0 - k_d = G \quad \text{Eq. 2.3}$$

where k_0 is the wavevector of the incident electron beam, k_d the wavevector of the diffracted electron beam, G a wavevector of the reciprocal lattice of the material. A

more intuitive way to think about the Laue condition is that the diffraction happens at the intersection of the Ewald sphere (a sphere in the reciprocal space with a radius of k_0) with the reciprocal lattice, as is shown in figure 2.5.

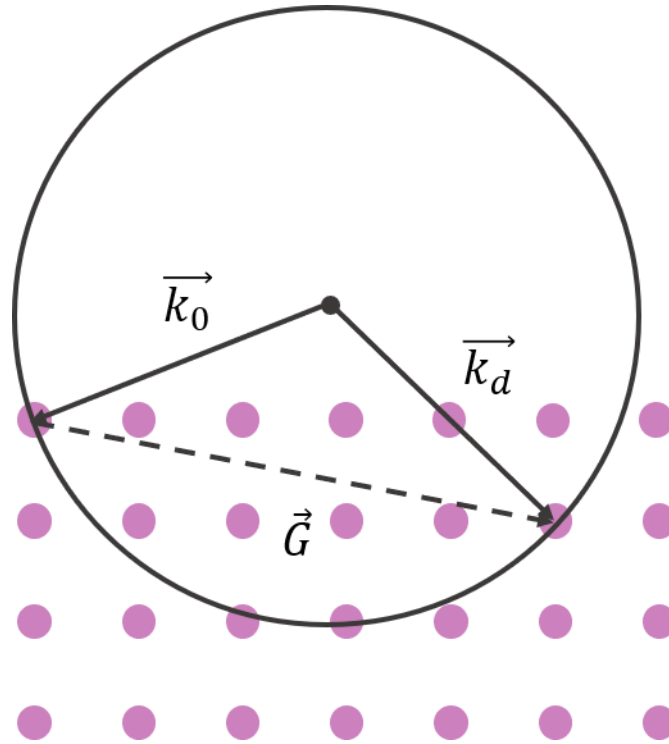


Figure 2.5. The reciprocal lattice (purple dots), the Ewald sphere (black circle), the wavevectors of the incident and diffracted electron beam (black arrows).

In the case of the RHEED, the reciprocal lattice becomes reciprocal rods given the small penetration depth of the electron beam. Since the k_0 is extremely large compared with the spacing of reciprocal rods, the curvature of the Ewald sphere turns out to be extremely small. These facts result in a line-shape intersection between the reciprocal rods and the Ewald sphere than dots. Figure 2.6 demonstrates the Laue

condition of RHEED, showing how a streak pattern is created by electron diffraction off a single crystal lattice.

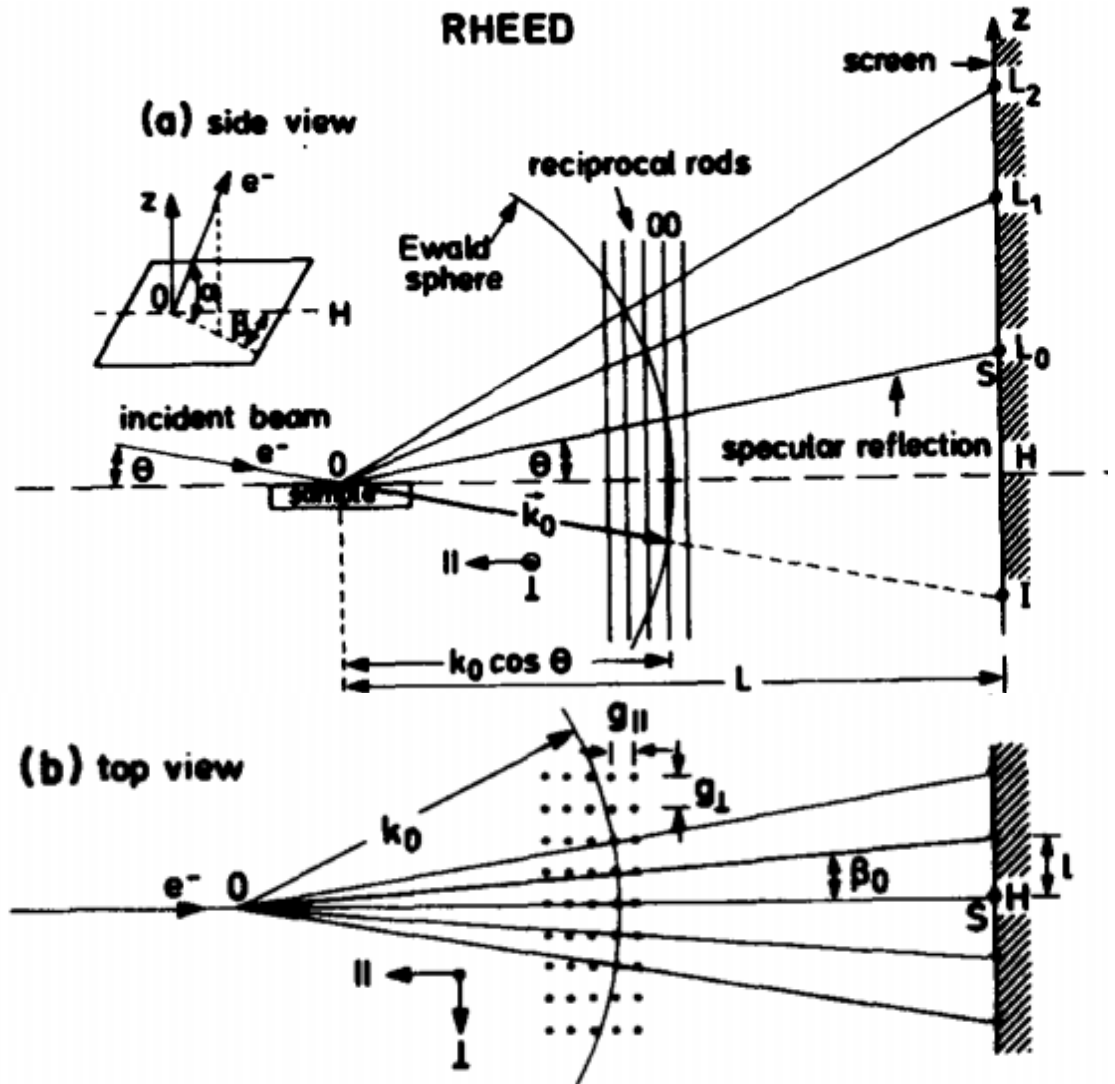


Figure 2.6. (a) side view and (b) top view of the Laue condition of RHEED.

Examples of streaky RHEED patterns during the growth of Bi_2Se_3 are shown in Figure 2.7. Two alternating patterns are always observed for single crystals as

substrate rotates caused by two major orientations in the a-b plane of the crystal, which are demonstrated in Figure 2.8. The wider spacing in the RHEED pattern corresponds to a smaller atomic spacing, and vice versa, because the reciprocal space is inverse of the real space.

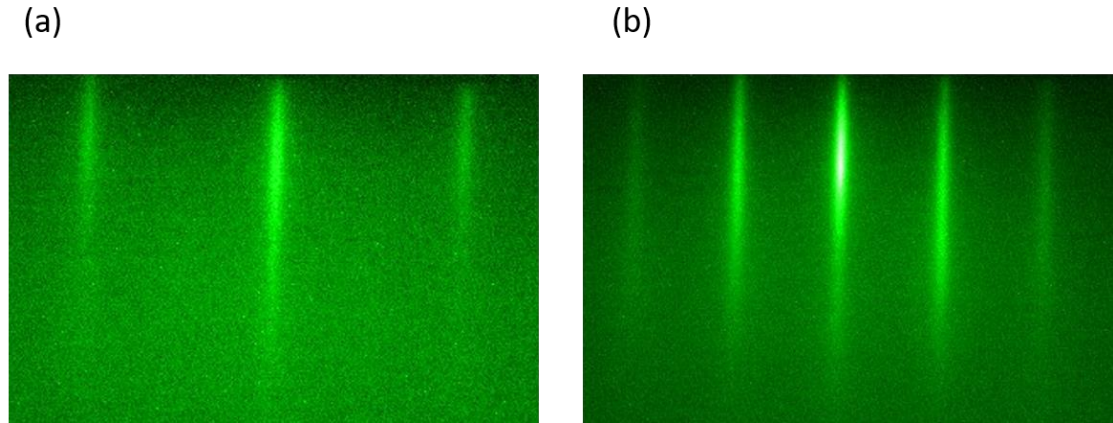


Figure 2.7. Characteristic RHEED patterns of epitaxial Bi_2Se_3 when looking at the orientation of (a) $[1\ 1\ \bar{2}\ 0]$ and (b) $[2\ \bar{1}\ \bar{1}\ 0]$.

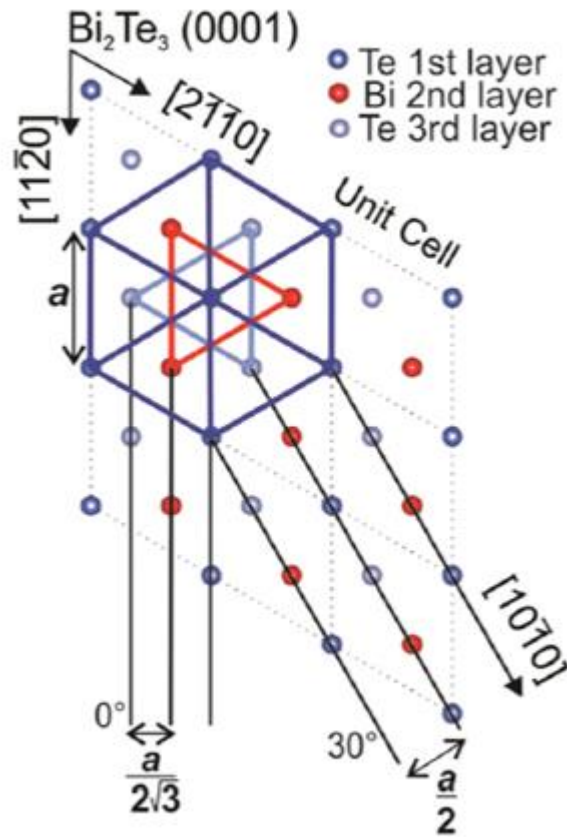


Figure 2.8. Top view of a TI lattice showing the two major orientations that are observed in RHEED. Figure used with permission from [73].

2.2 Nano-fabrication techniques

As discussed in the previous chapter, the coupling between the photons and the TI Dirac plasmons requires a grating coupler on top to compensate the wavevector mismatch. To fabricate such a structure, we use an Electron Beam Lithography (EBL), Electron Beam Deposition and Lift-off procedure.

2.2.1 Lithography

Lithography is a widely used technique capable of fabricating devices with fine structures both in academia and industries. Photolithography is now the most common way to fabricate transistors on silicon chips for many of the electronic devices that we use in our daily life.

Nowadays most of the lithography tasks are carried out in cleanrooms since most of the steps requires an ultraclean environment. The specific procedure for a lithography task may vary from case to case. For example, the industrial production of microchips includes complicated treatments to improve the yield and repeatability, while many of the laboratory tasks requires only basic procedures. The procedures that are used in this dissertation are listed below. All the fabrication procedures were conducted in the nanofabrication facility at University of Delaware.

Cleaning and preparation

The surface of the wafer needs to be as clean as possible since contaminations on the surface may damage the photoresist or lead to adhesion problems. Wet chemical treatments (solvents or oxidizers) are usually applied to remove contaminations. In the case of TIs, the fragility of TIs makes them incompatible with sonication and many types of oxidizers and solvents. In this dissertation, the surfaces of TI samples are gently rinsed with N-Methyl-2-pyrrolidone (NMP) and Isopropyl alcohol (IPA).

Photoresist (PR)

PRs are some polymers that are sensitive to light or electrons. After being exposed to light (photolithography) or electrons (EBL), the structures of the PRs are changed so they are more soluble (positive PR) or less soluble (negative PR) in some certain developers. PRs are usually spin-coated onto the wafer at a rate of 2000rpm to

6000rpm. Different spin rates result in different thickness of the PR layer. The wafers are then baked to a certain temperature to remove the solvents, as so the PR layer got hardened. In this dissertation, a single layer Poly(methyl methacrylate) (PMMA) A4 PR was used for the electron beam exposure. The spin rate is at 2000rpm for a PMMA thickness of 300nm. The wafers with PR are then baked at 170°C for 2 minutes.

Exposure

The wafers with PR layers are then exposed to a UV light beam (photolithography) or an electron beam (EBL) in a designated pattern. Depending on specific tasks, this step can be carried out in a mask aligner where the exposure (to UV light or to electron beam) patterns are defined by a photomask (a piece of glass with parts of it covered to block UV light) that attaches closely to the surface of the wafer, or by computer programs in a laser-writer or an EBL system. Depending on the type of PRs, a post-exposure bake may be required. In this dissertation, we use EBL tool Raith EBPG 5200 for electron beam writing.

Development

After the exposure, the wafers will be then treated with a developer, usually a type of alkaline solution, to remove the part of PR layer that is either exposed (positive) or not exposed (negative). The wafer is now ready for further fabrications, such as etching or metal depositions for a lift-off process. An Methyl isobutyl ketone (MIBK): IPA = 1:3 solvent was used as the developer for the PMMA PR. The process was kept for 4 minutes to ensure thorough removal of the exposed region.

A schematic of a typical lithography task is shown in figure 2.9.

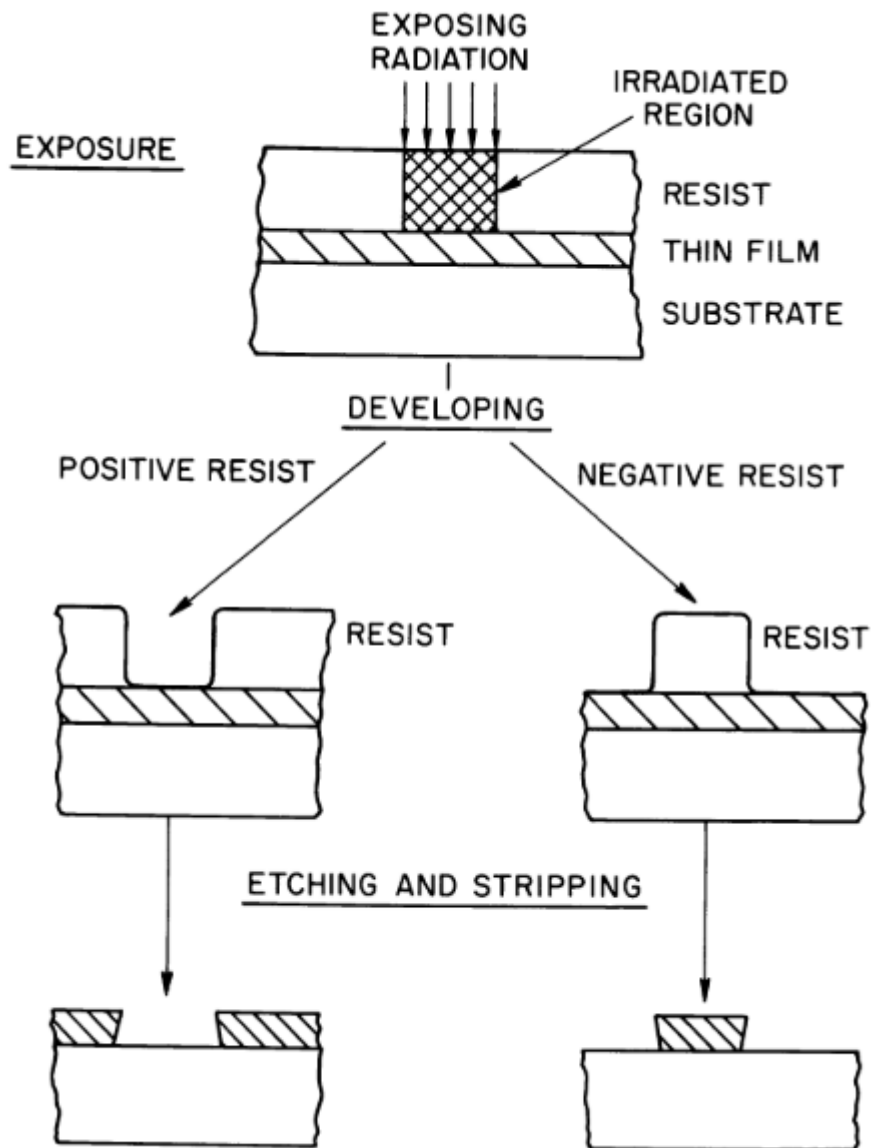


Figure 2.9. A schematic of a typical lithography process.

2.2.2 Lift off

After the lithography process, a part of the wafer is covered with PR, and the other part is not. A layer of metal will be then deposited onto the wafer uniformly.

An E-beam evaporator is used for the uniform metal layer deposition. E-beam evaporation is a physical deposition technique conducted in a high vacuum (1×10^{-8} torr to 1×10^{-6} torr). Unlike MBE where the source materials are evaporated by heating, the metal targets in an E-beam evaporator are bombarded by a high energy electron beam to create metal vapors. In this dissertation, we use an E-beam evaporator from PVD Product to coat the films with 50nm Au/10nm Ti. The angle of the film is adjusted directly facing to the target to avoid coating the vertical parts of the PR.

The metal-coated wafer will be then treated with a solvent, in our case NMP, in a hot water bath. In this step, the PR that is left on the surface of the wafer will be completely removed along with the metal on top of it, leaving the designated metal patterns resting on the wafer. The whole process is now finished. Figure 2.10 shows SEM images of a typical film before and after the liftoff process.

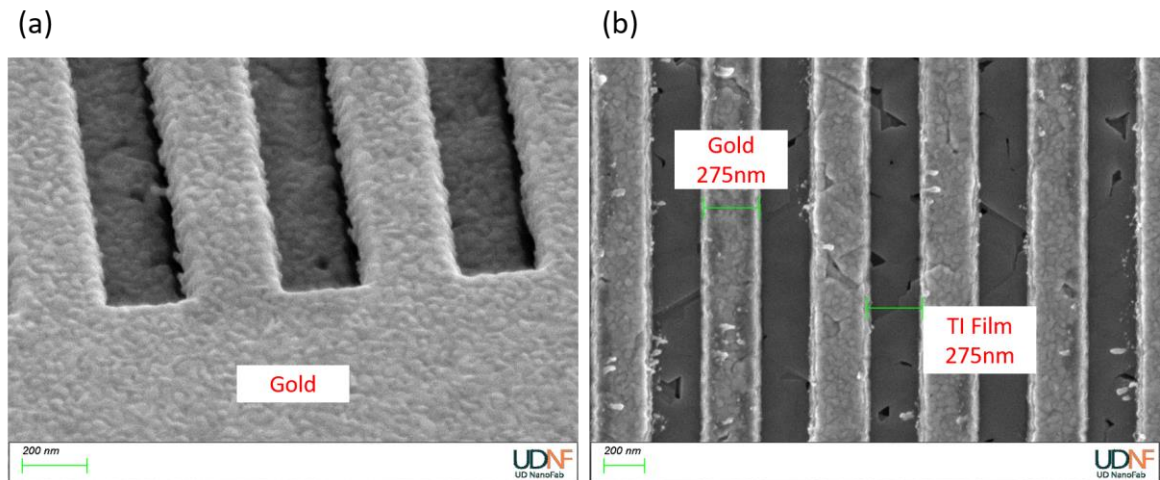


Figure 2.10. SEM image of the samples (a) before liftoff and (b) after liftoff.

2.3 Characterization techniques

2.3.1 Structural characterization

X-ray diffraction (XRD) is used to determine the crystal quality of our grown films.

XRD is a common tool for crystal structure characterization. The principle of a diffraction is discussed previously in 2.1. We will recall the Bragg's equation (Eq. 2.2)

$$2d\sin\theta = n\lambda \quad \text{Eq. 2.2}$$

where d is spacing between the lattice planes, θ the incident angle of the X-ray beam, n an integer number, and λ the wavelength of the X-ray (1.5406 Å for a Cu K- α X-ray source). By conducting a coupled θ - 2θ scan we get the crystallinity information of the sample along the c -plane. A typical θ - 2θ scan spectra of an MBE Bi₂Se₃ film is shown in Figure 2.11. The diffraction peaks that show up in the spectra are the [0 0 0 3 m] peaks of the hexagonal lattice, where m is an arbitrary integer.

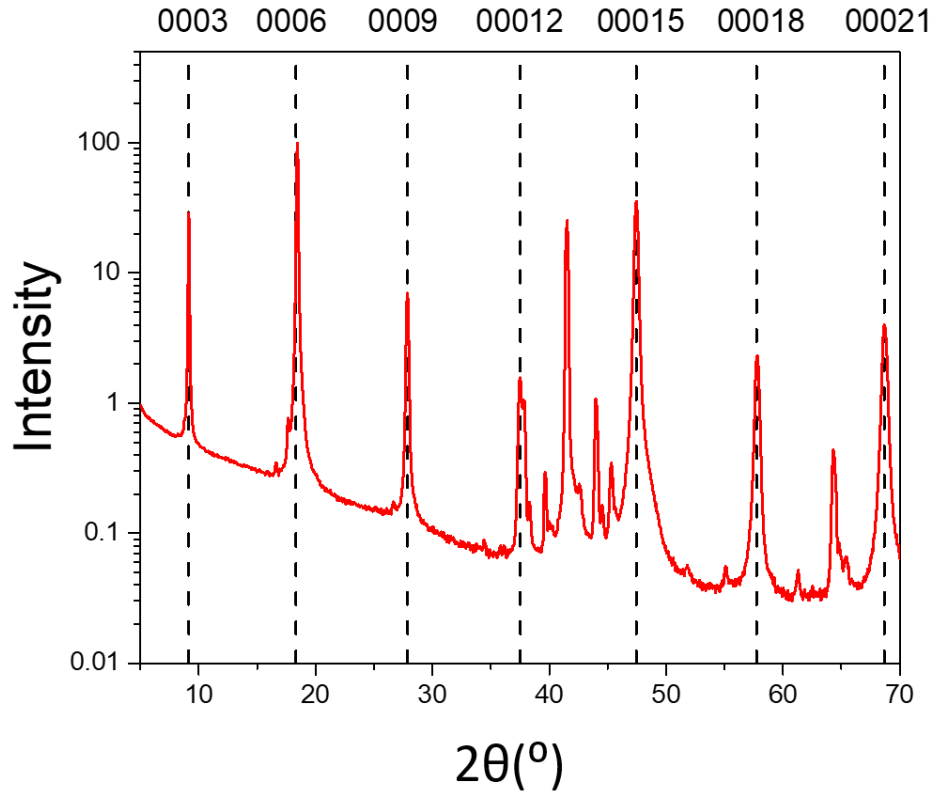


Figure 2.11. A typical XRD spectra of an MBE Bi_2Se_3 film. The peak around 42° is from the Al_2O_3 substrate.

The quality of the films can be seen from the diffraction peaks. A smaller FWHM of the diffraction peak indicates a better crystallinity. By applying the plane indexes into the Bragg's equation, we can extract the lattice constant from the diffraction peak positions.

$$d^2 = \frac{a^2}{\frac{4}{3}(h^2+k^2+hk)+\frac{a^2}{c^2}l^2} \quad \text{Eq. 2.4}$$

where h, k, l are the plane indexes, a and c are the lattice constants for a hexagonal lattice. In our case, $h, k = 0, l = 3m$, which immediately leads to

$$d = \frac{c}{3m} = \frac{\lambda}{2\sin\theta} \quad \text{Eq. 2.5}$$

Atomic force microscopy (AFM) is used to characterize the surface morphology of the MBE films. AFM has a cantilever with a sharp tip with a radius in the order of nanometers. When the sharp tip is in the near field of the sample surface, the force, determined by Hooke's law, between the tip and sample surface atoms are measured through the deflection of the cantilever. A laser beam is reflected off the back of the cantilever and is collected by a position detector whose output signal could provide us with the deflection of the cantilever. Figure 2.12 shows a typical AFM image of an MBE Bi_2Se_3 film, showing its characteristic pyramid morphology.

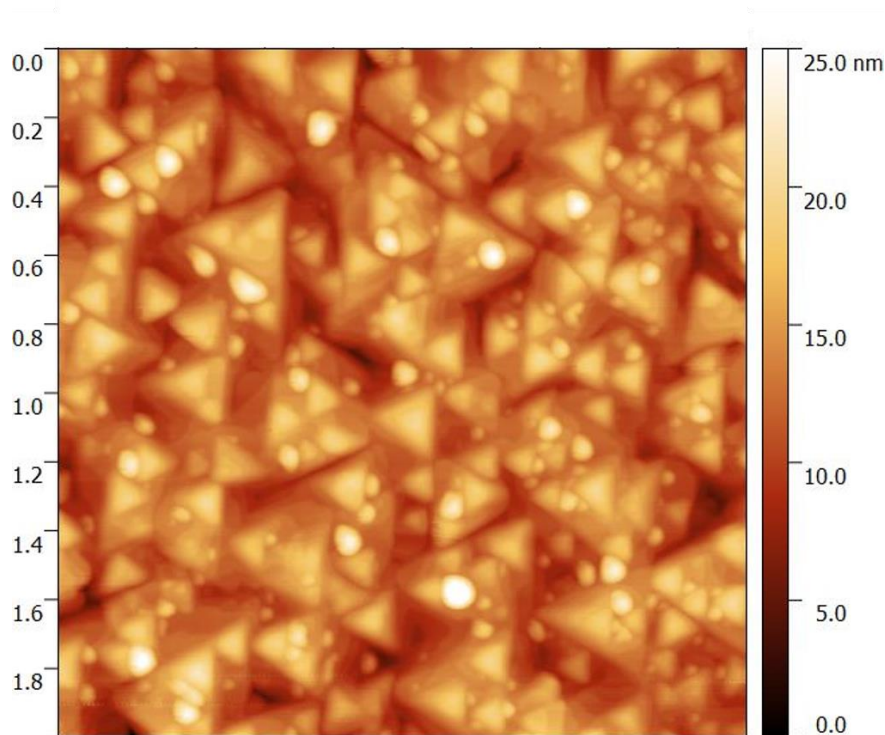


Figure 2.12. A typical AFM image of Bi_2Se_3 with a area of $2\mu\text{m} \times 2\mu\text{m}$. The color scale ranges from 0nm to 25nm.

2.3.2 Optical measurements

Fourier transform infrared spectroscopy (FTIR)

We use the FTIR instrument to characterize the optical responses of the samples in the THz range as well as in the mid-IR. The FTIR emits and detects a wide spectral range of light as opposed to dispersive spectrometers. The machine we use is a Bruker Vertex 70V Fourier transform infrared spectrometer. Figure 2.13 shows a simplified version of the FTIR instrument with a geometry of transmission measurement.

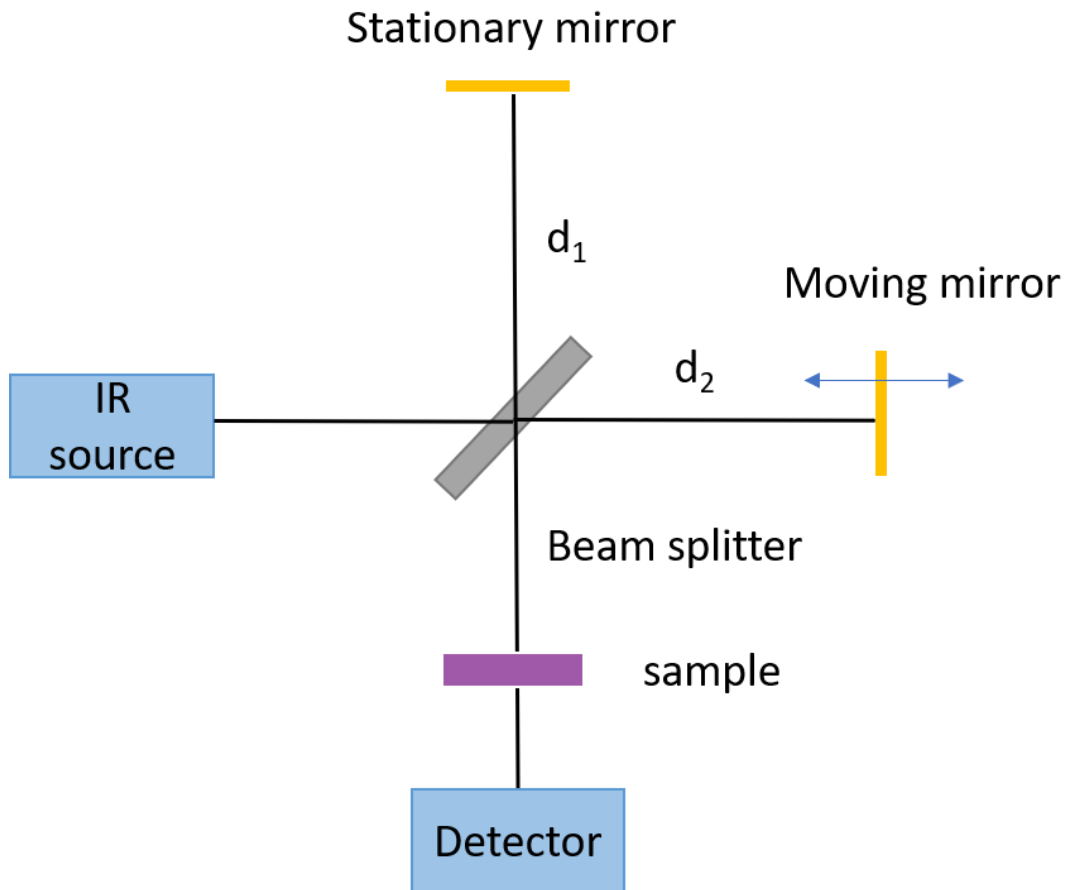


Figure 2.13. A schematic of an FTIR instrument with a transmission measurement geometry.

The IR source generates a wide-spectrum IR beam. Upon incident on the beam splitter, the beam is separated into two beams. One will be reflected by the stationary mirror, while the other will be reflected by the moving mirror. The two beams will recombine at the beam splitter again. For a specific light wavelength λ , constructive interferences will happen when optical path difference of the two beams $2(d_1 - d_2) = n\lambda$, n is an integer. The signal of this wavelength reaches maximum. Similarly, when $2(d_1 - d_2) = (n + 1/2)\lambda$, destructive interferences will happen, and the signal of this wavelength will reach its minimum.

The recombined beams will then transmit through and interact with the sample, and then reach the detector. Given that the IR beams contain a wide range of the spectrum, we would expect that the signals collected by the detectors will contain components from all wavelengths, which is difficult to interpret directly. The Fourier transformation can be used to transform the data into frequency domain by Eq. 2.6:

$$f(v) = \int_{x_0}^{x_1} f(x)e^{-2\pi i v x} dx \quad \text{Eq. 2.6}$$

where v is frequency, x is the position of the moving mirror. $f(v)$ and $f(x)$ are the signals in frequency and mirror position, respectively. Figure 2.14 shows the transmission data through air before and after the Fourier transformation.

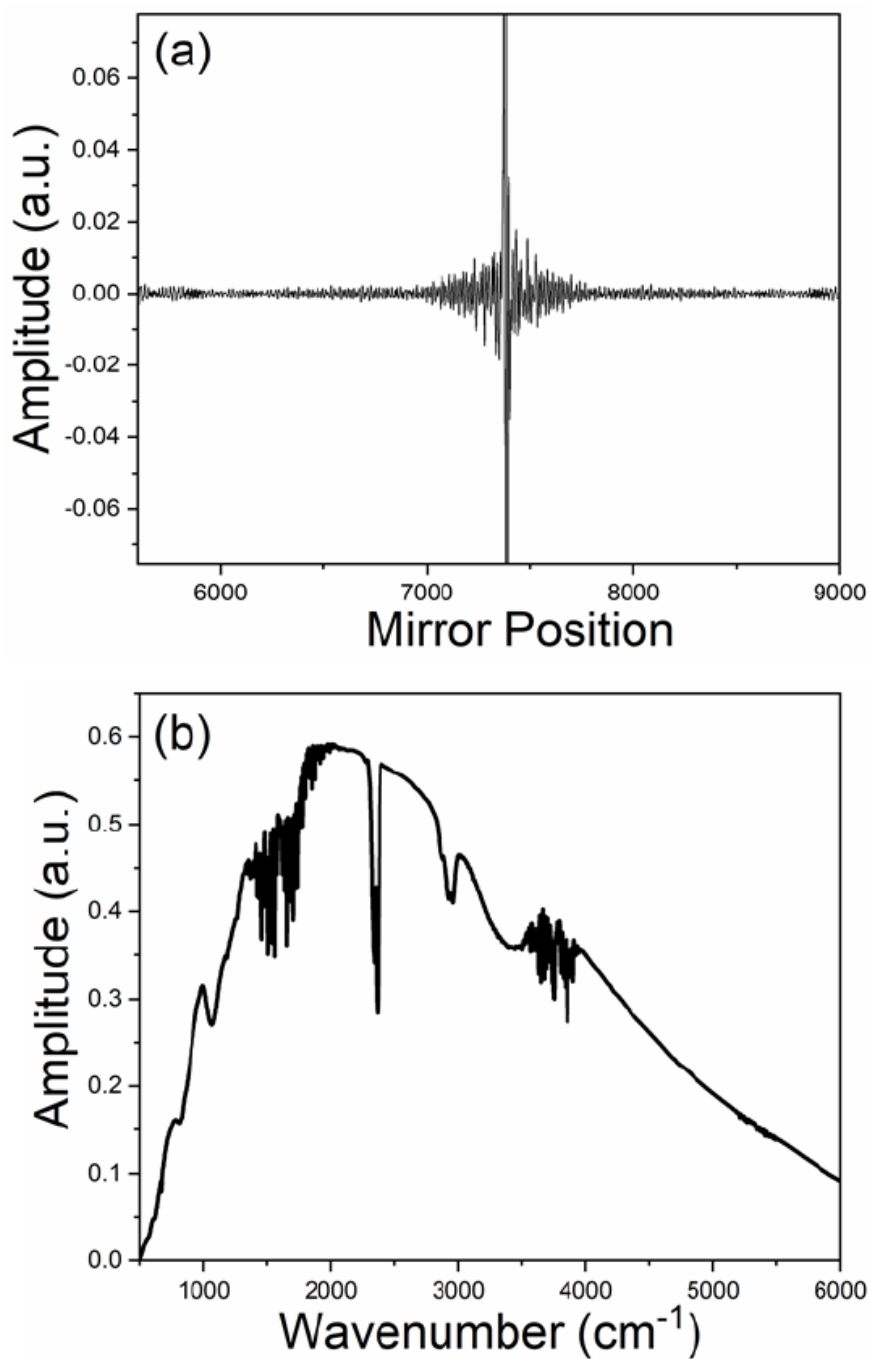


Figure 2.14. The FTIR transmission data (a) before Fourier transformation and (b) after Fourier transformation.

2.3.3 Transport measurements

We use Hall measurement to determine the transport properties of our films.

Charge carriers passing through a material under an external magnetic field perpendicular to the current path get bent by the Lorentz force. The accumulation of charges creates a voltage across the material. By measuring this voltage, one gets the information of the carriers in the material, such as the density and the mobility of the carriers. Equation 2.3 describes the qualitative relationship between the Hall voltage V_H , carrier density n , current I , external magnetic field B , film thickness t and electron charge e :

$$V_H = \frac{I B}{n t e} \quad \text{Eq. 2.3}$$

The geometry is demonstrated in figure 2.15.

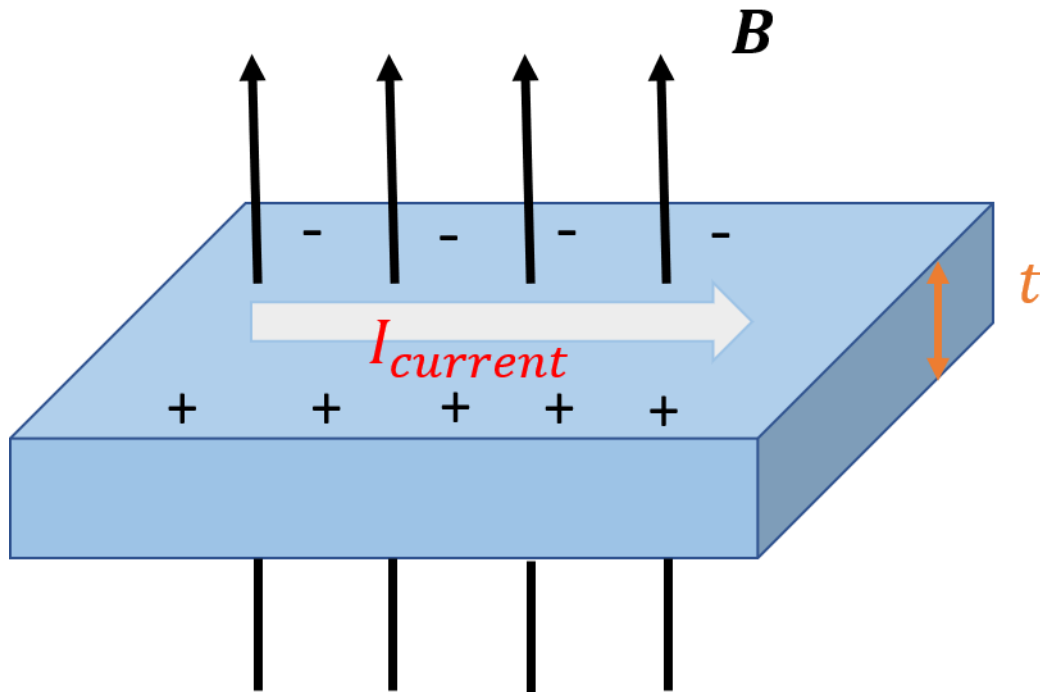


Figure 2.15. A schematic of the Hall measurement geometry.

For our samples which are grown on square substrates, a van der Pauw geometry is utilized as is shown in figure 2.16. The basic idea of a van der Pauw measurement is equivalent to a normal Hall effect, but the efforts in fabricating an applicable device are significantly reduced. One gets a quick precise measurement of the carrier concentration and the mobility with such a geometry[75].

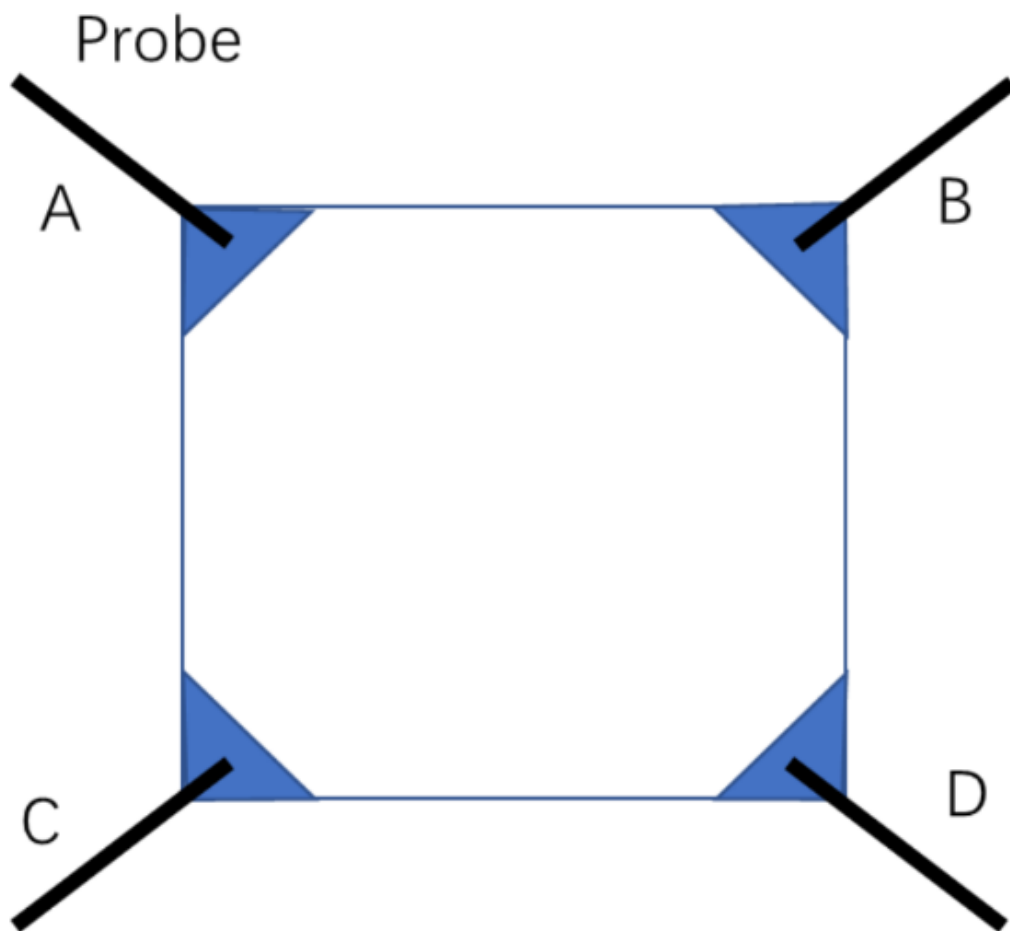


Figure 2.16. The van der Pauw four-point probe geometry. The blue triangles in the corners are the contacts, and black lines are the wires.

By running current I_{AB} through probe A and B and measuring the voltage V_{CD} , we get

$$R_A = \frac{V_{CD}}{I_{AB}} \quad \text{Eq. 2.6.}$$

Similarly, we get

$$R_B = \frac{V_{AC}}{I_{BD}} \quad \text{Eq. 2.7.}$$

R_A and R_B are the two characteristic resistances that are defined in the fundamental van der Pauw equation:

$$e^{-\frac{\pi R_A}{R_S}} + e^{-\frac{\pi R_B}{R_S}} = 1 \quad \text{Eq. 2.8}$$

where R_S is the sheet resistance of the sample.

The sheet resistivity can be calculated as

$$\rho = \frac{R_S}{t} \quad \text{Eq. 2.9.}$$

Hall measurement is then conducted with an external magnetic field B applied.

The two characteristic Hall voltage H_A and H_B are determined as follow:

$$H_A = \frac{V_{BC}}{I_{ADB}} \quad \text{Eq. 2.10.}$$

$$H_B = \frac{V_{AD}}{I_{BCB}} \quad \text{Eq. 2.11.}$$

Then the sheet carrier concentration can be determined as

$$n_s = -\frac{1}{2e} \left(\frac{1}{H_A} + \frac{1}{H_B} \right) \quad \text{Eq. 2.12.}$$

and the mobility μ as

$$\mu = \frac{1}{en_s \rho} \quad \text{Eq. 2.13.}$$

2.4 Summary

For a brief summary of this chapter, we introduced the growth (MBE), fabrication (lithography, lift-off), and characterization (RHEED, XRD, AFM, FTIR and MOKE) techniques that are used in this dissertation. This information would help

understand better of the experimental details that will be discussed in the following chapters.

Chapter 3

THE GROWTH OF TOPOLOGICAL INSULATORS WITH MOLECULAR BEAM EPITAXY

Tetradymite bismuth chalcogenides were known as thermoelectric materials with large Seebeck effect long before the discovery of their topological electronic properties[76]. The prevailing methods for the growth of bismuth chalcogenides were the bulk crystal methods when the thermoelectric properties were the major research topic[77], [78]. The synthesis of bismuth chalcogenide thin films or nanostructures for optical or electronic property related research were also explored including reactive thermal evaporation[79], Magnetron sputtering[80], bulk crystal exfoliation[81], chemical vapor deposition (CVD) [82]and solvothermal method[83].

In the first ever experimental work where the single Dirac cone surface states were observed in Bi_2Se_3 , the samples were cleaved from a bulk crystal[84]. The results from the angle resolved photoemission spectroscopy (ARPES) indicated that the fermi level was located in the conduction band, making transport measurements on TIs overwhelmed by the bulk currents[21]. Since then, many efforts on reducing bulk carriers have been reported, for example, by calcium doping[85] or by making Bi_2Se_3 ribbons and wires[86]. Epitaxial growth of Bi_2Se_3 and Bi_2Te_3 became particularly promising due to the high crystal quality, low surface roughness, large sample area, and the controllability over the thickness, enabling the observations of many characteristic TI surface properties[87]–[89].

The optimization of TI MBE growth has been a popular topic among the experimentalists regarding large numbers of non-topological electrons and the film aging effects[36]. People explored a wide variety of substrates, including c-plane Al_2O_3 [90], GaAs[91], SrTiO_3 [92], BaF_2 [93], Si[94], etc. One of the major constraints of using a type of substrate is the lattice mismatch with the epitaxial films, which leads to a variety of structural defects[95]–[97]. Figure 3.1 demonstrates the lattice mismatch between the TIs and a wide choice of epitaxial substrates.

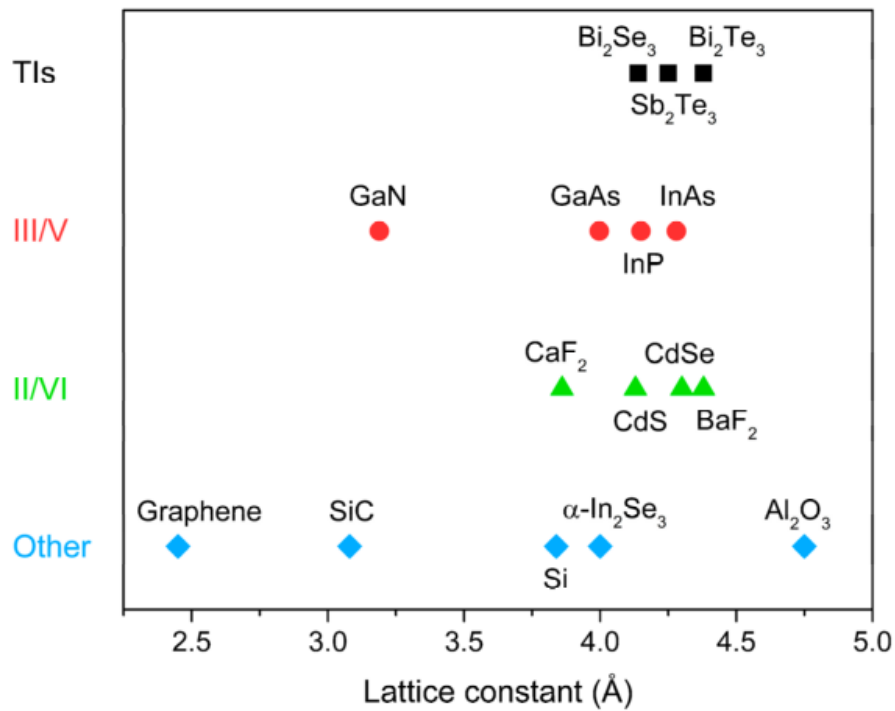


Figure 3.1. Lattice constants of various substrates compared to lattice constants of binary TIs. The crystal phase is (111) for zincblende and cubic lattices and (0001) for wurtzite and hexagonal lattices. Figure used with permission from [36].

Among all types of substrates, Al_2O_3 (0001) have been the most popular choice due to its low cost, easy availability, high surface quality and relatively inert chemical properties[36]. The films for this dissertation were all grown on Al_2O_3 (0001).

Despite many common manipulations of growth parameters, the problem still remains: the large numbers of bulk carriers in epitaxial TI films result in a low sensitivity of the surface transport properties[21]. In our MBE system, the lowest sheet carrier concentration for TI Bi_2Se_3 films directly grown on Al_2O_3 (0001) substrates are limited to $3 \times 10^{13} \text{cm}^{-2}$, which indicates a large bulk doping shown by ARPES measurements on Bi_2Se_3 with similar carrier density[98]. Thus, new routes for growing epitaxial TI films with low bulk doping are needed.

3.1 The ternary alloy: $\text{Bi}_2(\text{Se}_{1-x}\text{Te}_x)_3$ (BST)

Tetradymite $A_2^V B_3^{VI}$ including Bi_2Se_3 and Bi_2Te_3 generally show non-stoichiometry with an excess of bismuth atoms[99]. The non-stoichiometry is commonly believed to be associated with the following defects: i) B^{VI} vacancies where atoms are missed in the B lattice and ii) A^V/B^{VI} antisite defects where atoms in the B lattice are replaced by A atoms. As was discussed above, epitaxial Bi_2Se_3 films grown directly on Al_2O_3 (0001) substrates are n-type. Bi_2Te_3 can be controlled as p-type or n-type in both single crystals[100], [101] and thin films[102], [103], due to the competition between p-type Bi/Te antisites and n-type Te vacancies. It is generally believed that in bulk crystals, point defects due to Se vacancies and Bi/Te antisites are the dominant source of doping in bulk crystals. Thus, it is reasonable to assume the same for thin films.

Following this trend, one possible proposal to tune down the carrier density in TIs would be to grow $\text{Bi}_2(\text{Se}_{1-x}\text{Te}_x)_3$ alloys where n-type Se vacancies and p-type

Bi/Te antisites compensate each other. There have been studies on the ternary alloy $\text{Bi}_2(\text{Se}_{1-x}\text{Te}_x)_3$ single crystals showing that a specific composition of the ternary alloy, Bi_2SeTe_2 , has a reduced bulk doping than other species[104], [105]. As is demonstrated in scanning transmission electron microscopy (STEM)[106], bulk crystal Bi_2SeTe_2 has a lattice configuration where the selenium layer is confined in the center of a QL (shown in Figure 3.2).

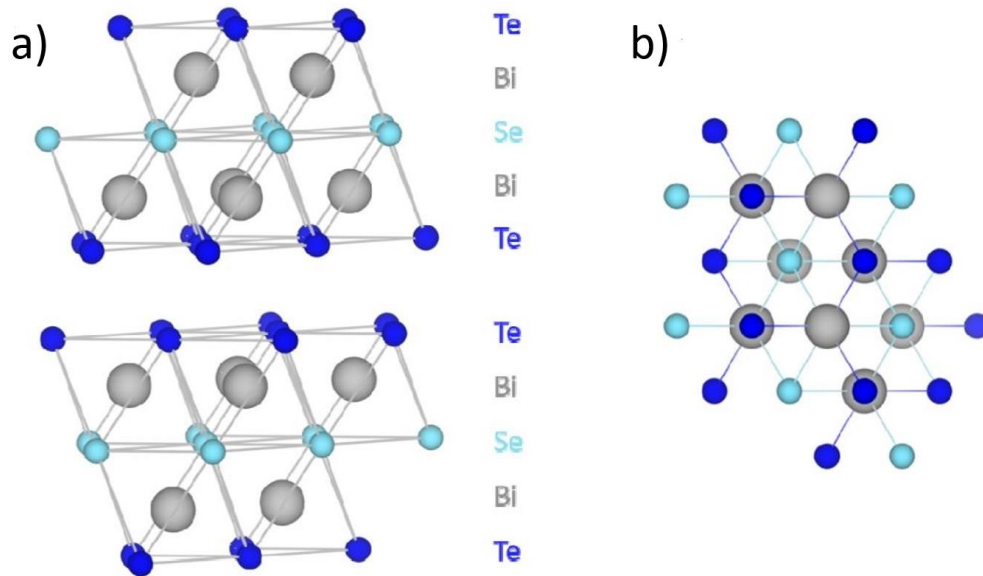


Figure 3.2. Lattice configuration of the proposed Bi_2SeTe_2 . (a) View along the a- b plane showing two quintuple layers (QLs). Tellurium preferentially occupies the outside sites (small dark blue atoms) while selenium preferentially occupies the middle site (small light blue atoms). Bismuth sits between (large gray atoms). (b) View along the c-axis showing the three-fold in-plane symmetry. Figure used with permission from [107].

Figure 3.3 shows the STEM and an associated energy dispersive spectroscopy (EDS) results on the single crystal Bi_2SeTe_2 , indicating the preferential segregation of different elements.

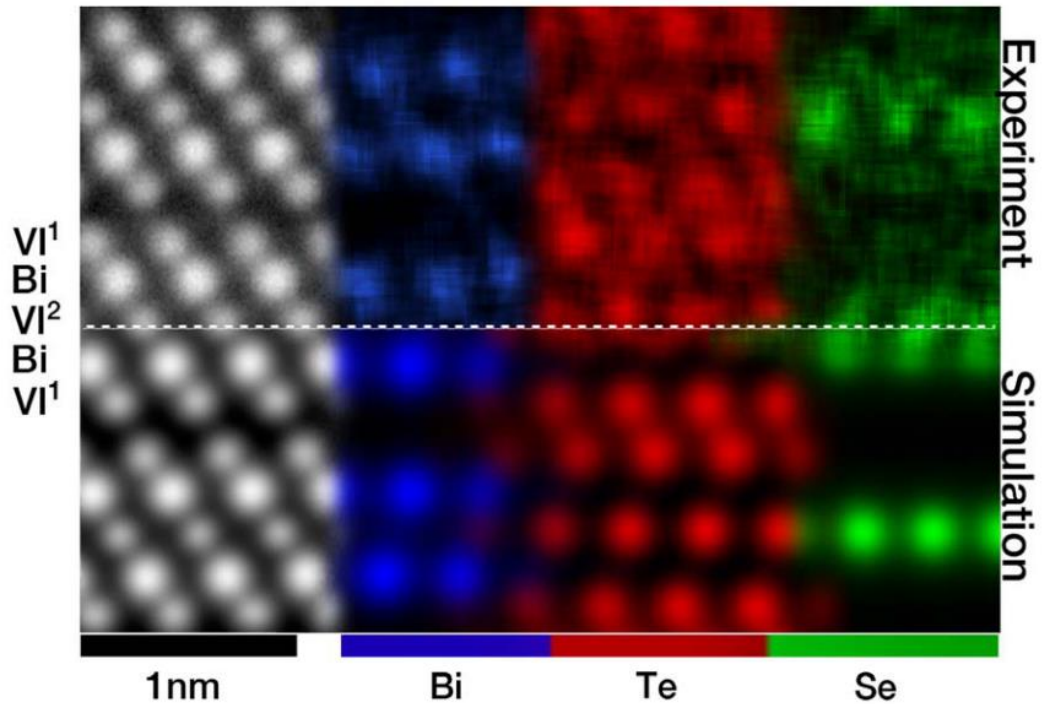


Figure 3.3. The top part of the figure is the atomic-resolution STEM (white and gray) and the associated EDS (blue, red and green). The blue, red and green atoms are Bi, Te and Se atoms revealed by EDS, respectively. The bottom part of the figure is the DFT simulation. Figure used with permission from [106].

There have also been previous reports of $\text{Bi}_2(\text{Se}_{1-x}\text{Te}_x)_3$ grown by MBE using traditional effusion cells[108], [109]. In these studies, atomic force microscopy (AFM), scanning transmission microscopy (STM), and angle resolved photoemission spectroscopy (ARPES) data were shown. The ARPES data in both cases indicated an ability to control the band structure of the film by adjusting the composition. Some evidence for a shift in Fermi energy relative to the Dirac point was also shown as the film composition was changed. However, transport data can be hardly found in these epitaxial BST studies, making it difficult to determine the suitability of these materials

for electrical devices or discover if indeed the trivial carrier density is reduced. Thus, a transport property analysis on epitaxial BST films becomes significant to see whether the bulk carriers are reduced by growing the ternaries.

In this dissertation, we first conducted structural analysis of the epitaxial BST thin films with different Se/Te composition (3.1.1). Then we explored the growth parameter space, including Bi: Se: Te ratio and substrate temperatures. The optimal growth window is reported (3.1.2). We then present Hall data showing the sheet density and mobility of these films as a function of alloy composition (3.1.3).

3.1.1 The structural analysis of the epitaxial BST thin films

A series of BST films were grown on c-plane sapphire substrates using a variety of growth parameters. The *in situ* surface quality of the films was confirmed by streaky RHEED patterns. A detailed discussion of RHEED can be found in chapter 2. Figure 3.4(a) and 3.4(b) show a typical RHEED images during growth of BST films. The different spacing in RHEED stripes comes from different spacing between planes in a hexagonal lattice.

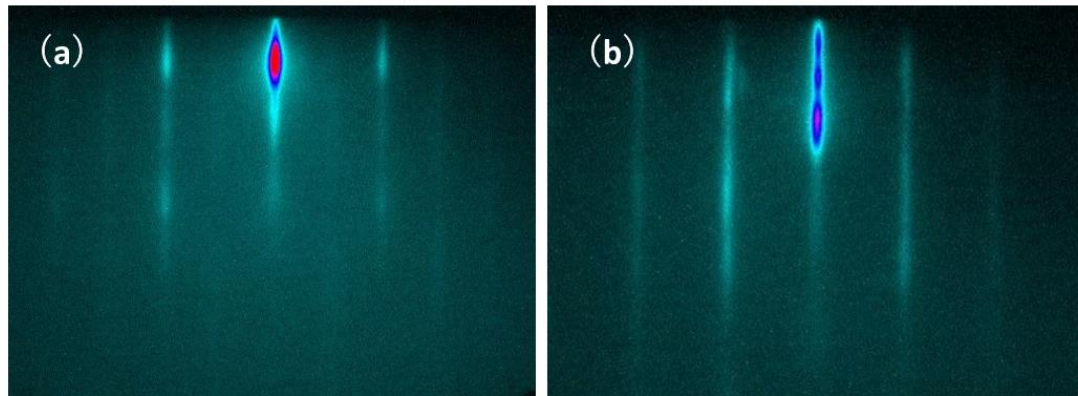


Figure 3.4. RHEED images of $\text{Bi}_2(\text{Se}_{0.8}\text{Te}_{0.2})_3$ films taken during the growth. (a) Diffraction pattern along $[1\ 0\ \bar{1}\ 0]$; (b) Diffraction pattern along $[2\ \bar{1}\ \bar{1}\ 0]$.

XRD was employed to determine the crystal structure as well as the chemical composition of the films. Assuming that Vegard's law holds, the lattice constant of the samples along the c-direction varies linearly between Bi_2Se_3 and Bi_2Te_3 . As discussed in the previous chapter, the lattice constants can be directly calculated from peak positions in the XRD spectrum.

In figure 3.5, the XRD spectra from (10° to 70°) for a set of films with different compositions are shown. The peak near 42 degrees is from the sapphire substrate. Most other peaks shift to smaller angles as the tellurium content is increased. The data were all normalized to the highest peak of each spectrum and offset so that each sample can be seen clearly.

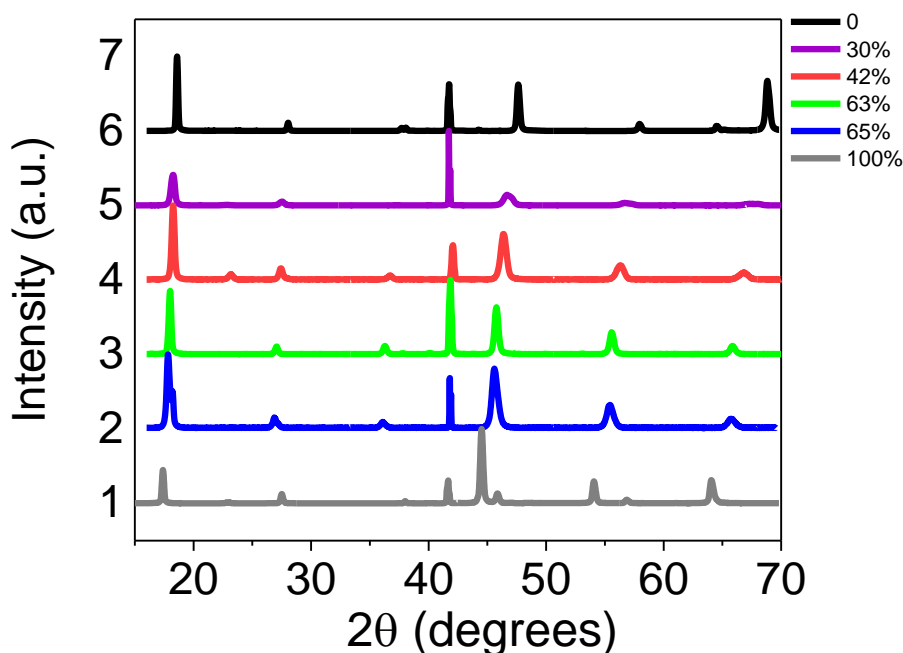


Figure 3.5. The coupled theta-two theta scan spectra from (10° to 70°) for the epitaxial BST samples with a selenium concentration from 0 to 100%, determined by the diffraction peak positions and Vegard's Law. All intensities are normalized, and data is offset for clarity. Figure used with permission from [107].

Figure 3.6 shows only the $[000\bar{2}1]$ peak (60° - 70°) for these same films, demonstrating the shift in peak position with changing composition. The peaks were normalized for better demonstration.

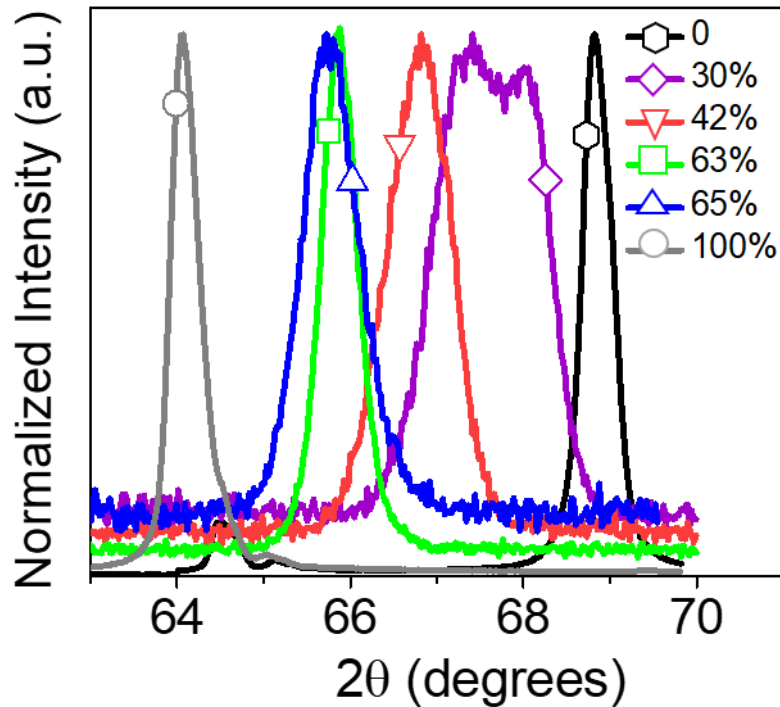


Figure 3.6. The coupled theta-two theta scan spectra from (63° to 70°) for the same epitaxial BST samples as those in figure 3.4. Figure used with permission from [107].

We can see from figure 3.5 that, the X-ray spectra for binary Bi_2Se_3 and Bi_2Te_3 both show good signal-to-noise ratio and low FWHM, indicating good crystal qualities. However, lower signal-to-noise ratios and larger FWHMs are observed in the ternary samples, indicating the reduction in crystal qualities. For the $\text{Bi}_2(\text{Se}_{0.7}\text{Te}_{0.3})_3$ sample a double peak appears, indicating two separate compositions, a feature which is only present in some selenium-rich growth attempts. These observations led to the

conclusion that the $\text{Bi}_2\text{Se}_3\text{-Bi}_2\text{Te}_3$ incorporation caused a reduction in the crystal qualities in the epitaxial growths. This reduction of crystal quality can be attributed to the phase segregation between a Se-rich phase and a Te-rich phase due to the competition of Bi-Se bonds and Bi-Te bonds.

3.1.2 The exploration of the growth parameter space

To figure out the growth conditions for the BST thin films with different composition, we explored the source flux ratios as well as the substrate temperatures.

We first compared a series of samples grown at a substrate temperature of 300°C , with different Se: Te :Bi ratios. The Se: Bi flux ratios were measured with BFM, and Te fluxes were recorded by bulk temperature and valve positions. Bismuth fluxes were kept the same. The lattice constants and the calculated tellurium composition from XRD are listed in table 3.1.

Table 3.1. Flux ratio during growth and resulting composition of samples shown in figure 3.4 and figure 3.5.

Se: Bi	Te Bulk (°C)	Te Valve (mils)	Lattice Constant(Å)	% Te
4:1	200	0	28.7	0
4:1	200	150	29.18±0.18	30.16±0.18
1:1	210	150	29.39±0.17	42.22±0.24
1:1	215	300	29.76±0.10	62.58±0.22
1.4:1	230	150	29.80±0.15	65.04±0.41
0:1	260	100	30.5	100

From Table 3.1, we can see that in order to increase the tellurium content of the films, a much lower selenium flux and larger tellurium flux are required than would be expected based on the growth parameters for pure Bi₂Se₃ films. This trend is

commonly seen in II/VI systems including CdSeTe and ZnSeTe[110], [111] and can be understood by considering the stability of the binary compounds. The bond length of Bi_2Se_3 is shorter than that of Bi_2Te_3 , implying that the binding energy is larger for Bi_2Se_3 than Bi_2Te_3 . In addition, the enthalpy of formation for Bi_2Se_3 at 273K is 28 kJ/(g atom) while for Bi_2Te_3 at 273K is 15.7 kJ/(g atom)[112]. These data indicate that Bi_2Se_3 is the more stable of the two compounds, which would account for the preferential incorporation of selenium in the alloy.

The Substrate temperatures were also explored with a fixed source flux ratio (Se: Bi = 1.4:1, Te bulk at 230°C, Te valve position at 150 mils) aiming for 67% of Te composition. Data are shown in figure 3.7.

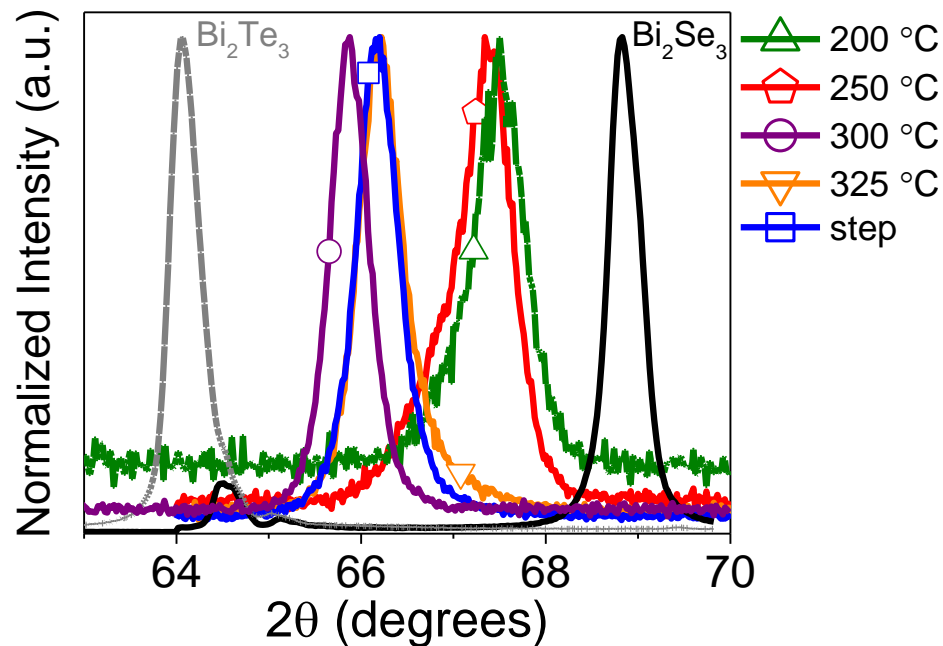


Figure 3.7. XRD spectrum of samples grown with a fixed flux ratio and a variable substrate temperature. Figure used with permission from [107].

The blue line with a square represents the sample grown with a two- step procedure: a substrate temperature of 200°C for first 4 QLs and followed by a ramp up to 300°C for the rest of the growth.

As we can observe, the sample grown using the lowest substrate temperature of 200°C has the lowest tellurium incorporation. As the substrate temperature is increased up to 300°C, the tellurium incorporation also increases. This behavior demonstrates that outside the optimal growth window (substrate temperature of 300°C[52]), the Bi_2Se_3 compound will form more readily than the Bi_2Te_3 compound, again due to the greater stability of this material. Two other substrate temperatures were tried: 325°C, and a two-step procedure in which the first four QLs were grown at 200°C followed by a ramp up to 300°C for the rest of the growth, inspired by work on other TI materials[113]–[115]. Both samples showed a similar composition, with less tellurium than the sample grown at the optimal growth temperature of 300°C. When growing pure Bi_2Se_3 , a substrate temperature of 325°C was found to show significant degradation as selenium readily outgasses from a film grown at this relatively hot temperature. These results show that the growth parameters for the BST alloy must be chosen carefully to ensure the desired composition.

3.1.3 The characterization of transport properties

As described above, we undertook this growth study with the expectation that Bi_2SeTe_2 would exhibit a lower sheet concentration and a higher mobility than the pure Bi_2Se_3 or Bi_2Te_3 , due to a reduction in selenium vacancies and Bi/Te antisite defects. Room temperature Hall measurements were taken on films with a variety of compositions and growth parameters including substrate temperature and Bi:VI flux

ratio, and the sheet density and mobility extracted. The data were presented in table 3.2.

Table 3.2. Room temperature carrier mobility and sheet concentration of BST samples. Samples are arranged in the order of Bi₂Se₃, near Bi₂Se₂Te, near Bi₂SeTe₂, and Bi₂Te₃. All samples are n-type.

	Tellurium Content %	Mobility cm ² /(V·s)	Sheet Carrier Concentration (x 10 ¹³ cm ⁻²)
Bi ₂ Se ₃	0	622.82±31.14	3.65±0.22
	0	622.16±31.10	3.67±0.22
Bi ₂ Se ₂ Te	30.16±0.18	190.17±9.51	6.78±0.41
	31.06±0.16	164.46±8.22	7.43±0.45
	31.96±0.16	287.74±14.39	5.97±0.36
	35.76±0.26	200.78±10.04	6.07±0.36
Bi ₂ SeTe ₂	61.15±0.30	117.58±5.88	8.76±0.53
	62.58±0.22	186.29±9.31	4.70±0.28
	64.98±0.33	142.98±7.15	6.02±0.36
	65.04±0.41	131.49±6.57	7.34±0.44
Bi ₂ Te ₃	100	136.50±6.82	9.27±0.56
	100	109.89±5.49	11.44±0.69

The data in the table is organized by film composition. The multiple films in each composition bracket were grown with different substrate temperatures and different flux ratios, in an attempt to optimize the growth of this compound. This data,

unfortunately, did not show the anticipated behavior: the mobility of the films decreases, and the sheet density increases as the tellurium content increases, with no significant change at the desired Bi_2SeTe_2 composition. Despite exploring a wide range of substrate temperature and flux ratio parameter space, all alloy films showed much worse transport properties than our original Bi_2Se_3 films, though some growth parameter combinations did show a local improvement in transport properties.

Noticeably, the carrier concentration and mobility data for pure Bi_2Te_3 show that the epitaxial Bi_2Te_3 films are heavily n-type doped, opposite to what was observed in many single crystal studies. There are also previous findings that the sheet density of our Bi_2Se_3 films was independent of film thickness[52]. These findings imply that the bulk carriers in our films are not the dominant carrier pathway. A reasonable hypothesis is that defects in the first few QLs of the sample are dominating the sample properties.

It has previously been observed that the first few QLs of TIs grown on mismatched substrates are defective, despite the expected van der Waals bonding between the film and substrate[113], [114]. As noted above, Bi_2Te_3 is less stable than Bi_2Se_3 and therefore more likely to form defects at the film/substrate interface when grown on a mismatched substrate. Bi_2Te_3 may also have a stronger interaction with the substrate than the more-stable Bi_2Se_3 . These higher-defect density layers can then lead to a larger sheet carrier density and a lower mobility in Bi_2Te_3 compared to Bi_2Se_3 . When tellurium is alloyed into the Bi_2Se_3 crystal, similar effects are expected since tellurium will preferentially occupy sites on the outside of the QL, while selenium will preferentially occupy the inner site.

As a summary of section 3.1, we demonstrated the growth of BST alloys by MBE. A variety of Se: Te flux ratios were explored, enabling the composition of the film to be tuned from pure Bi_2Se_3 to pure Bi_2Te_3 . It was found that selenium preferentially incorporates into the film, necessitating a reduction in the selenium flux to obtain films with a large tellurium content. The substrate temperature was also found to have a significant effect on the film composition, with films grown at lower substrate temperatures exhibiting a preferential selenium incorporation. Transport data was also collected on the films. Contrary to expectations, the films with the best transport properties (largest mobility and smallest sheet density) were pure Bi_2Se_3 films. Any alloying of tellurium caused a sharp decrease in mobility and an increase in sheet density, even at the desired Bi_2SeTe_2 composition. This result leads us to conclude that the transport properties of our TI films are dominated by the film/substrate interface.

3.2 The epitaxial growth of Bi_2Se_3 on a $(\text{Bi}_{1-x}\text{In}_x)_2\text{Se}_3$ (BIS) buffer layers

From the previous discussion, we see that the growth of BST has turned out to be less helpful. These results brought us to a new path in enhancing the transport properties of TIs: enhancing the quality of the TI/non-TI interfaces. Our proposal is to use $(\text{Bi}_{1-x}\text{In}_x)_2\text{Se}_3$ (BIS) as a buffer layer in the epitaxial growths of Bi_2Se_3 films.

There have been some efforts to grow In_2Se_3 by molecular beam epitaxy[116], [117]. In_2Se_3 is a trivial bulk insulator with the same crystal structure and similar lattice constant to Bi_2Se_3 . This makes In_2Se_3 a good candidate for use as a buffer layer between the TI and the substrate and for use in heterostructure devices[118]–[120]. However, the lattice match between In_2Se_3 and Bi_2Se_3 is not perfect (~3.4% lattice mismatch). In addition, indium is known to diffuse into Bi_2Se_3 at the $\text{Bi}_2\text{Se}_3/\text{In}_2\text{Se}_3$

interface[121]. For indium concentrations above 30%, BIS is a trivial band insulator with a gap size dependent on indium concentration[122]. We have therefore chosen to investigate the use of the BIS alloy as a buffer layer.

Despite the many advantages of the BIS alloy, literature describing the optimal growth procedure is scarce. In this section, we will present the optimization of the epitaxial growth of BIS films, and then the growth of Bi_2Se_3 films on the optimized buffer layer.

3.2.1 Co-deposition of BIS

Initially, we attempted to grow BIS films of a variety of concentrations directly on sapphire substrates using a co-deposition method supplying bismuth, indium, and selenium simultaneously. Despite a detailed exploration of growth parameter space, in all cases, the RHEED pattern did not show the sharp lines characteristic of good film growth. An example is shown in figure 3.8 for a film with $x=0.5$.

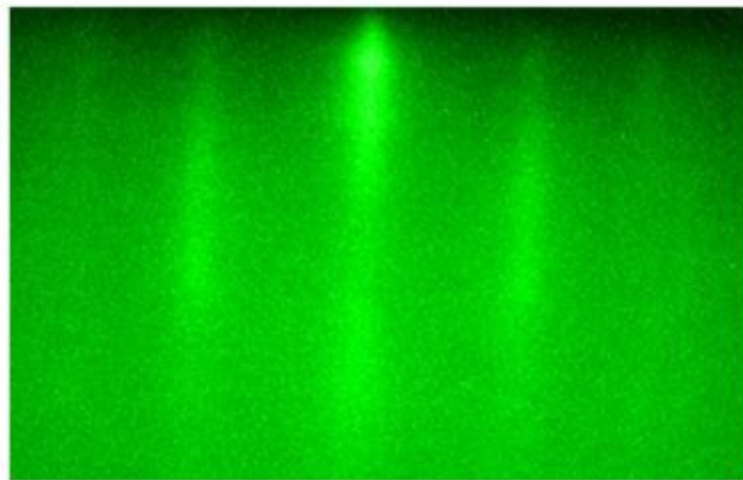


Figure 3.8. A typical RHEED image during the co-deposition growth of BIS with $x=0.5$.

Diffuse, spotty streaks appear which are indicative of poor-quality growth. In addition, the same RHEED pattern was observed for all substrate rotations, indicating a polycrystalline film. XRD measurements taken on these films are presented in figure 3.9, with indium concentration increasing from bottom to top. The indium compositions at this stage were determined by beam flux - growth rate calibration, which will be covered in 3.2.3.

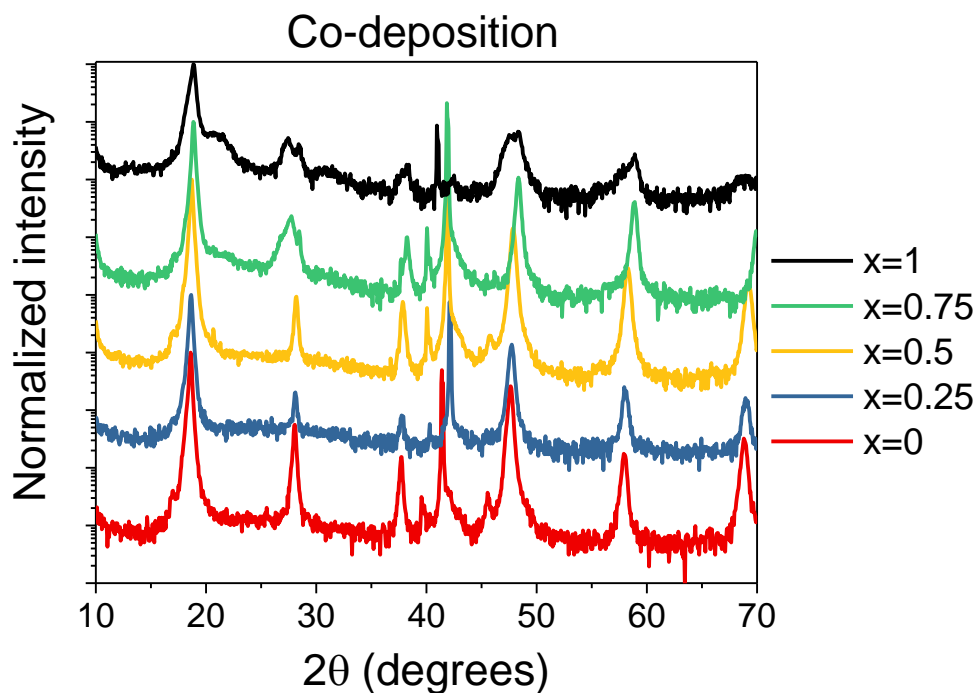


Figure 3.9. The XRD spectra for BIS samples by co-deposition with an indium concentration from 0 to 1.

For pure Bi_2Se_3 films, we observe the family of peaks corresponding to the $[000m]$ (m is an integer, as discussed in chapter 2) direction, as well as peaks near 42° from the Al_2O_3 substrate. The full FWHM of the Bi_2Se_3 peaks is small, indicating good film quality.

However, as the indium content increases, the film quality degrades. The FWHM becomes larger and, especially for the pure In_2Se_3 film, double peaks arise. We believe this degradation of the crystal quality is primarily due to the multiple polymorphs of In_2Se_3 , as well as the many other In-Se phases. In_2Se_3 has at least five polymorphs, usually denoted α , β , γ , δ , and κ [123]–[125]. The α phase is generally considered to be the only stable phase at room temperature in bulk crystals, though the β and γ phases have been observed at room temperature in thin films. Although all four polymorphs share the same R3m structure as Bi_2Se_3 , they exhibit different lattice constants. The literature on this compound is inconsistent, but most reports agree that the β phase has a slightly smaller in-plane lattice constant than the α phase, while the γ phase is much larger. We are aiming to grow only the β -phase of In_2Se_3 , as it mostly resembles the crystal structure of the tetradymite Bi_2Se_3 .

3.2.2 The sequential growth for BIS

In order to achieve high-quality growth of large indium content BIS films, we moved to a thin seed layer grown with sequential deposition. In this method, we deposited 5QL of Bi_2Se_3 on the sapphire substrate at 300°C , followed by 5QL of In_2Se_3 at the same temperature[122]. The bilayer was then heated under a selenium overpressure to 425°C and annealed. This annealing step resulted in the indium diffusing into the Bi_2Se_3 layers[121], leading to a 10QL 50% BIS seed layer with good structural quality (AFM shown in Fig. 3.12(a)). The seed layer was then cooled to the desired growth temperature, and subsequent BIS films grown using the standard co-deposition method. A schematic of the sequential growth process is shown in figure 3.10.

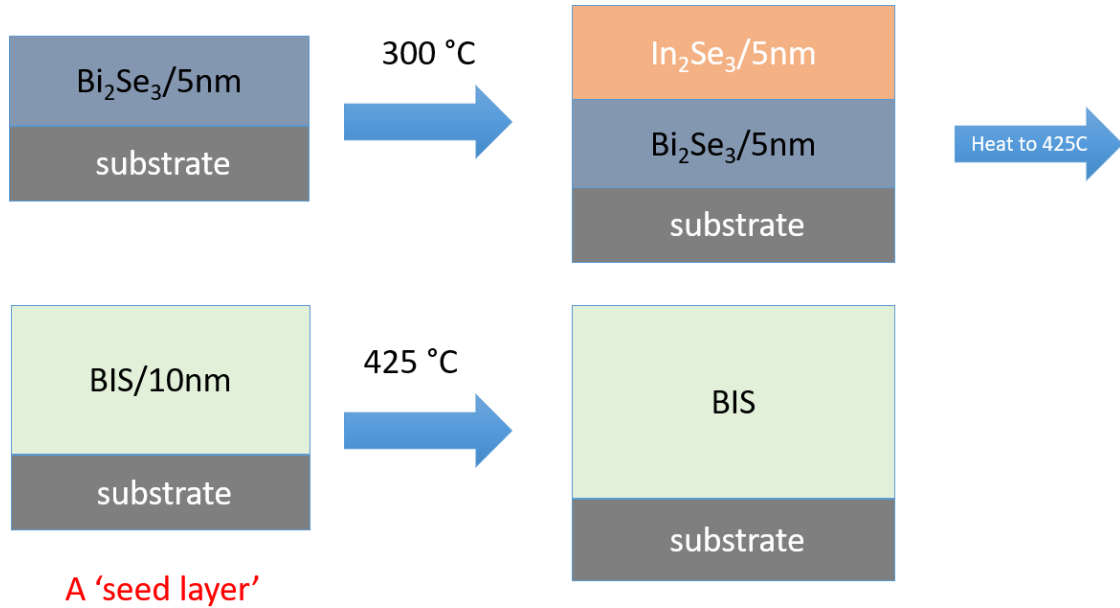


Figure 3.10. A schematic of a sequential growth process for BIS films.

It is worth noting that the seed layer formed after the annealing will not be completely chemically homogeneous. Evidences can be found in the rutherford backscattering measurement data (see next section). However, Hall measurements performed on a sample of only the seed layer were completely insulating, indicating that the transport channels through Bi_2Se_3 are eliminated. RHEED images of a pure In_2Se_3 film grown on this seed layer are shown in figure 3.11. The streaks are narrow, and we observe different streak spacing in the $[10\bar{1}0]$ and $[2\bar{1}\bar{1}0]$ directions, indicating flat, single-crystal growth.

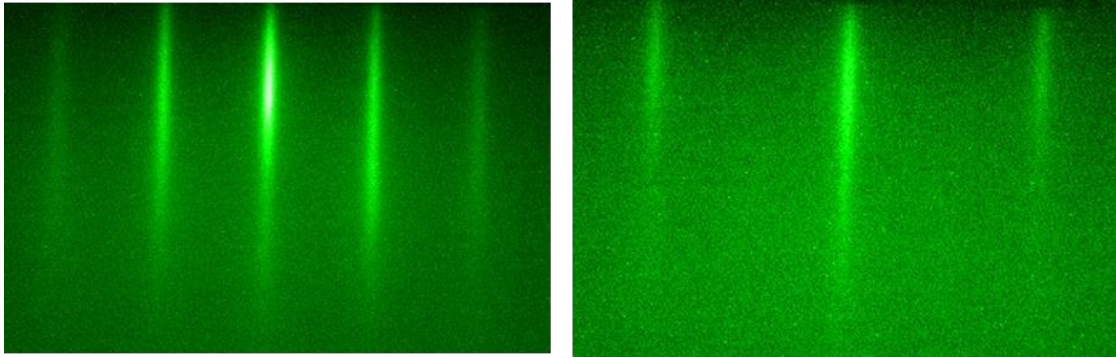


Figure 3.11. RHEED images of In_2Se_3 growth on seed layers.

Figure 3.12 presents XRD data for five BIS films grown using this sequential deposition technique. All films show narrow linewidths, with the FWHM varying only from 0.18° to 0.24° . For higher indium content films, no peak splitting is observed, indicating successful growth of a single In_2Se_3 polytype. We therefore determine that the subsequent deposition seed layer technique provides a good template for the growth of BIS films of all compositions.

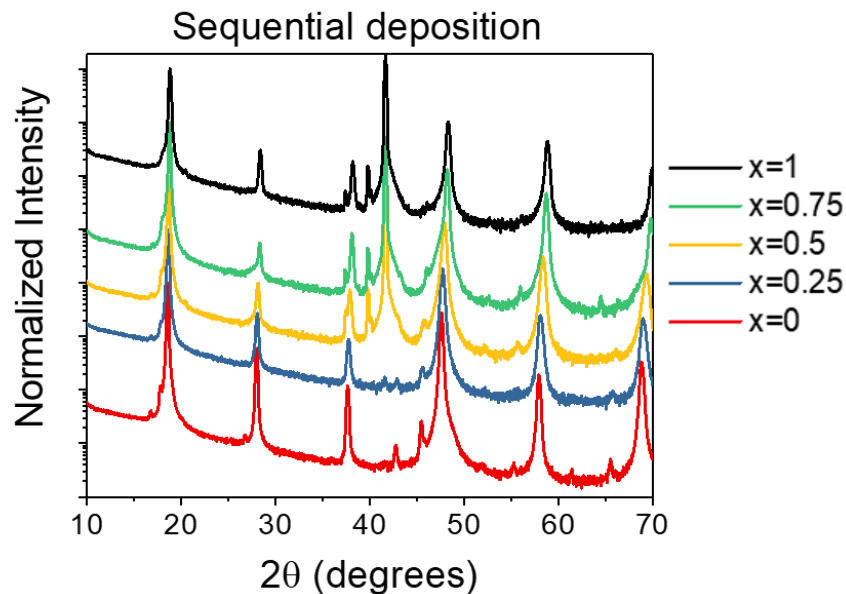


Figure 3.12. The XRD spectra for the BIS films grown with sequential method.

3.2.3 The characterization of indium content

In the discussion of the two BIS growth methods, the indium content for all the samples discussed in this chapter were characterized by a beam flux - growth rate calibration. We first calibrate the growth rate of Bi_2Se_3 (In_2Se_3) with a variety of Bi (In) fluxes measured by BFM. The growth rates were determined after the growth by taking an X-ray reflectivity (XRR) measurement. Then the Bi/In ratio in the BIS samples can be determined by the growth rate ratio, assuming that bismuth and indium have a similar rate of incorporation during a BIS ternary growth.

To verify this assumption, we conducted RBS measurements (as mentioned in the last section) on three samples with an indium content of 25%, 50% and 75% determined by the growth rate calibration. Film thickness and Bi/In ratio Data are shown in table 3.3. Measurements were done at the 1.7 MV Ion Beam Analysis Facility at Rutgers University.

Table 3.3. Film thickness, In content by growth rate and In content by RBS measurement.

Film thickness by RBS (nm)	In content by growth rate (%)	In content by RBS (%)
79	25	31
109	50	53
116	75	74

From the table above, we can see that the indium content measured by RBS are not far from what we expected from the growth rate, indicating that our assumption holds. However, the simulation of the RBS data indicates a non-homogeneity across the films. Taking the BIS50 sample as an example: a three-layer approximation (67nm

$\text{Bi}_{0.89}\text{In}_{1.19}\text{Se}_3$, 24nm $\text{Bi}_{0.91}\text{In}_{1.06}\text{Se}_3$, and 18nm $\text{Bi}_{1.50}\text{In}_{0.77}\text{Se}_3$) fitted better than a homogenous BiInSe_3 film, as shown in figure 3.13.

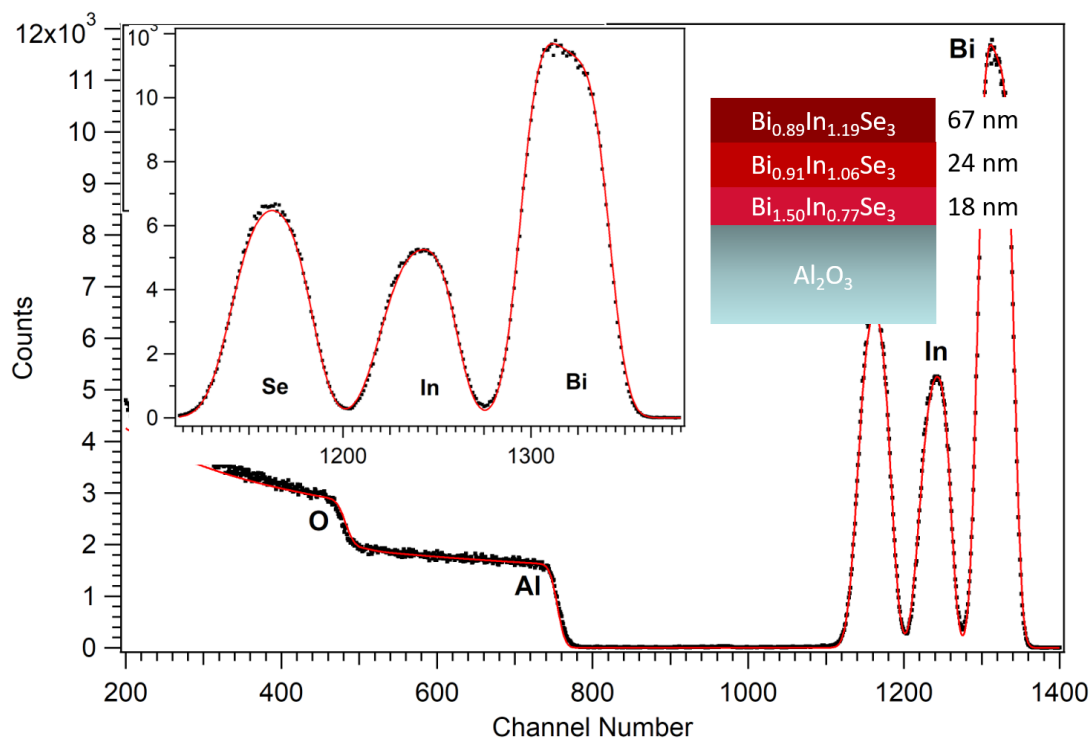


Figure 3.13. RBS data vs simulation with the three-layer approximation. Inset is the zoom in of the spectra to make the Se, In and Bi peak clear.

As we can see, indium gets more concentrated closer to the top surface, while bismuth gets more concentrated closer to the bottom surface. This indicates a strong interdiffusion between the Bi and In atoms in the films.

These results may lead to concerns about heavy indium diffusion into the Bi_2Se_3 films on the BIS buffer layers. However, XRR data on the Bi_2Se_3 films grown on seed layers show that an interface between the seed layer and the Bi_2Se_3 can still be distinguished, with the thickness of each layer close to what we expect. Although we do not have a thorough analysis on the Bi/In interdiffusion, a couple of reasons can

still be proposed to help understand this observation. Firstly, we annealed the seed layer at 425°C to ensure a good mixture of Bi_2Se_3 and In_2Se_3 , but the subsequent BIS buffer layer and Bi_2Se_3 layer were grown at 100 degrees lower. This could significantly reduce the diffusion rate. Secondly, the RBS data were usually taken months after the films were grown, while the X-ray, AFM and Hall measurements were conducted immediately after growth. Thus, it is expected to see heavier diffusion in RBS data. We should admit that there will be some degree of interdiffusion inevitably, but the effects are considered small and do not affect our later conclusions too much.

3.2.4 BIS as a buffer layer

The ultimate goal of this study is to use BIS as a buffer layer for the growth of high-quality Bi_2Se_3 . Therefore, we compared the morphology and electrical properties of a Bi_2Se_3 film deposited directly on sapphire to one grown on a co-deposition BIS buffer and one grown using the BIS sequential deposition technique. We judge the quality of the overgrown Bi_2Se_3 films by their room temperature electrical properties: films with a higher mobility and a lower sheet density (indicating a Fermi energy closer to the Dirac point) are of better quality. It should be noted that every BIS film we have tested is insulating at room temperature. Presumably BIS films with indium content lower than 3% will be conductive, but all our films are above 25%, which is far beyond the threshold. We are therefore confident that the electrical properties for Bi_2Se_3 grown on BIS come only from the Bi_2Se_3 film. In Table 3.4, we provide the growth details for all the films we will be discussing in this section.

Table 3.4. Growth parameters for all Bi₂Se₃/BIS films, including sample name, sample number, seed layer type (none, co-deposition, or sequential deposition seed layer), substrate temperature during BIS buffer growth (T_{sub}), BIS buffer composition (x), room temperature Bi₂Se₃ mobility (μ), and room temperature Bi₂Se₃ sheet density (n_s). All films are n-type. We use an error bar of 5% for Hall mobility and 6% for Hall sheet concentration. The error range of each is determined by the mean deviation from the average among multiple measurements on the same film.

Sample	Number	Seed	T_{sub} ($^{\circ}\text{C}$)	x	μ ($\text{cm}^2/\text{V s}$)	n_s ($\times 10^{13} \text{ cm}^{-2}$)
A	257	None			434 ± 21.7	2.6 ± 0.16
B	279	Co.	425	0.5	314 ± 15.7	1.1 ± 0.07
C	298	Sub.	425	0.5	659 ± 32.9	1.4 ± 0.08
D	311	Sub.	425	0.3	601 ± 30.0	1.8 ± 0.11
E	312	Sub.	375	0.3	686 ± 34.3	1.4 ± 0.08
F	313	Sub.	325	0.3	365 ± 18.2	2.3 ± 0.14
G	314	Sub.	425	0.75	690 ± 34.5	1.4 ± 0.08

We begin our discussion by considering films A, B, and C. These comprise 50nm of Bi₂Se₃ grown directly on sapphire (A), 50nm of Bi₂Se₃ grown on 50nm of 50% BIS grown with co-deposition (B), or 50nm of Bi₂Se₃ grown on 50nm of 50% BIS grown on the seed layer (C). In all cases, after the growth of the BIS buffer, the substrate temperature was reduced to 300 $^{\circ}\text{C}$ for the growth of the Bi₂Se₃ layer. The properties of sample A are fairly standard for Bi₂Se₃ films grown on sapphire; a sheet density of $3 \times 10^{13} \text{ cm}^{-2}$ is indicative of a Fermi energy near the bottom of the conduction band. If the Fermi energy were within the bandgap (resulting in transport only through the topological surface states), we would expect a sheet density in the 10^{12} cm^{-2} range. Sample B grown using co-deposition shows a significant reduction in sheet density, but also a reduction in mobility. The improvement in sheet density can

be attributed to a reduction in defects in the first few Bi_2Se_3 QLs due to the presence of the buffer layer, while the reduction in mobility is due to the poor surface morphology of the co-deposition buffer. For sample C, we observe a significant increase in mobility, while the sheet density remains low, approximately half that of the Bi_2Se_3 film grown directly on sapphire. A plot of these results is shown in figure 3.14.

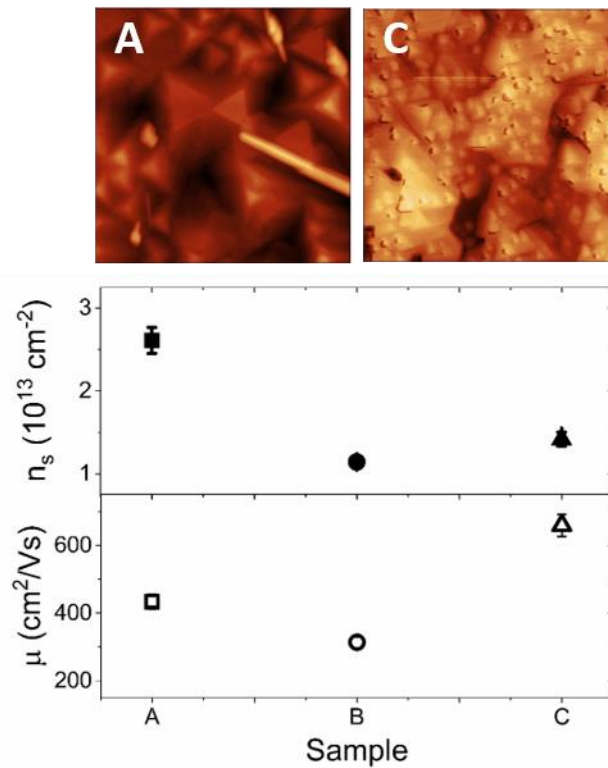


Figure 3.14. Carrier density (filled symbols) and mobility (open symbols) for samples A (black square), B (black circle), and C (black triangle). Error bars are shown, but for many samples are smaller than the size of the symbol. AFM images are shown at top for samples A and C, as indicated. The AFM images are both $2 \times 2 \mu\text{m}$ and on a color scale of 0–40 nm. Figure used with permission from [126].

In figure 3.14, we also show AFM images for samples A and C. Sample A shows many triangular domains and significant twinning, as expected for these films grown by van der Waals epitaxy[127]. However, film C shows a wider range of domain sizes but a smaller overall surface roughness. In addition, the extent of twinning as judged by the variation in orientation of the triangular domains is drastically reduced, leading to an overall improvement in mobility. We can therefore clearly conclude that growing Bi_2Se_3 on a BIS buffer with a seed layer significantly improves the film properties. In the rest of this section, we will describe how various growth parameters for the buffer layer grown on the seed layer affect the quality of the buffer and thus electrical properties and morphology of the overgrown Bi_2Se_3 films.

Effect of substrate temperature

We first studied the effect of substrate temperature on the properties of the BIS buffer. Three samples with a buffer thickness of 50nm and a 30% indium concentration were grown: D buffer ($T_{\text{sub}} = 425^\circ\text{C}$), E buffer ($T_{\text{sub}} = 375^\circ\text{C}$), and F buffer ($T_{\text{sub}} = 325^\circ\text{C}$). AFM images of the buffers alone are shown in Fig. 3.15.

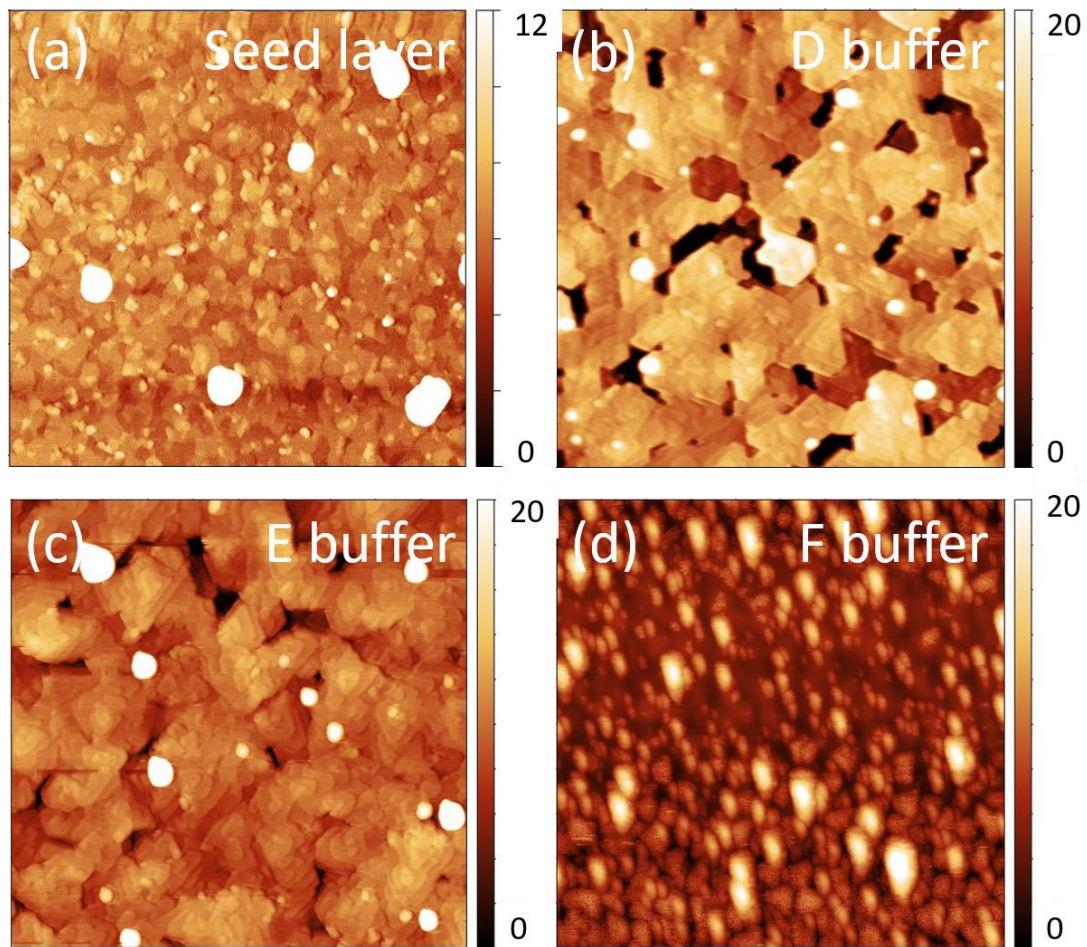


Figure 3.15. AFM images of the 10QL seed layer after annealing (a), and 50nm 30% BIS buffers grown on the seed layer at 425°C (b), 375°C (c), and 325°C (d). All scans are $2 \times 2 \mu\text{m}$ and the color scales are shown at right for each image. Figure used with permission from [126].

Figure 3.15(a) shows the surface morphology of the seed layer after annealing. The surface is generally smooth, with many small domains of 1–2QL in height. It should be noted that the tall dots observed on some AFM images are attributed to environmental contamination and are not believed to be intrinsic to the film. Figures 3.15(b)–(d) show AFM images for the three buffer layers with no overgrown Bi_2Se_3 . It

is clear that the substrate temperature significantly affects the structural quality of the buffer. For the buffer grown at 425°C (figure 3.15(b)), large hexagonal and triangular domains are observed, as expected. The pit-like features in this sample are caused by incomplete layer growth, most likely due to thermal roughening. For the buffer grown at 375°C (figure 3.15(c)), we primarily observe triangular domains and spiral growth with layer step heights of 1QL, similar to what occurs during growth of pure Bi₂Se₃[127]. There are also fewer pit-like features in this buffer than in the one grown at 425°C, which supports thermal roughening as their cause. Finally, figure 3.15(d) shows the buffer grown at 325°C. The morphology for this sample is quite different than the others, comprising only hillocks with no observable crystalline domains. In addition, the single QL step heights that were observed in figure 3.15(b) and 3.15(c) are not present in this buffer. This was somewhat surprising, since we grow pure Bi₂Se₃ at 300°C, and these buffers only contain 30% indium. We hypothesize that the lower growth temperature led to indium aggregation in this film, which leads to the observed hillocks. Overall, it is clear that the substrate temperature has a strong effect on buffer morphology.

We now consider films D, E, and F, comprising 50nm Bi₂Se₃ grown on these buffer layers. The electrical properties of these samples are shown graphically in Fig. 3.16. Sample E, with the buffer grown at 375°C shows the highest mobility and lowest sheet concentration, while sample D (425°C buffer) is only slightly worse. However, sample F (325°C buffer) shows a significant reduction in mobility and increase in sheet concentration. This is consistent with the buffer morphology: the buffer for sample E showed the best morphology, with large triangular domains, while the buffer for sample D was similar though showed more pits between domains. The poor-

quality buffer for sample F resulted in a poor quality overgrown Bi_2Se_3 film. This can also be observed in the AFM images of the overgrown Bi_2Se_3 , also shown in Fig. 3.16. Sample E has the largest domains and highest mobility, while sample D has only slightly smaller domains and reduced mobility. Sample F, however, has much smaller domains and a correspondingly low mobility.

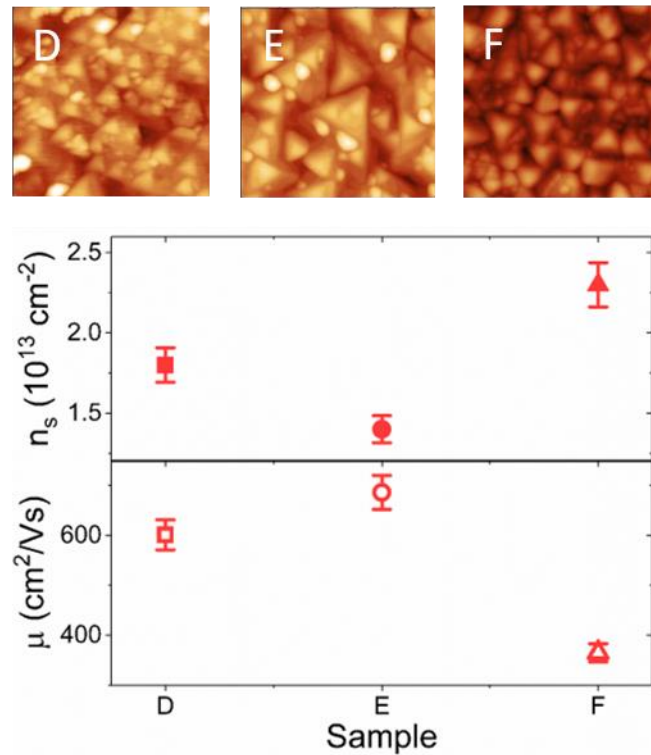


Figure 3.16. Carrier density (filled symbols) and mobility (open symbols) for samples D (red square), E (red circle), and F (red triangle). AFM images are shown at top for samples D, E, and F, as indicated. The AFM images are all $1 \times 1 \mu\text{m}$ and on a color scale of 0–25 nm. Figure used with permission from [126].

It can be concluded from the data above that the optimal growth temperature for BIS films (425°C) are higher than that of Bi_2Se_3 (300°C). For Bi_2Se_3 growth, we

generally grow in the lower temperature regime where we get selenium overpressure without excess selenium sticking on the film surface and leading to a growth rate determined purely by the bismuth flux. However, for the case of BIS growth, somewhat higher growth temperatures are clearly beneficial. We attribute this to the stability of the In_2Se_3 compound as well as the smaller surface mobility of indium compared to bismuth. In_2Se_3 melts at ~ 1160 K, while Bi_2Se_3 melts at only 979 K. It is therefore not surprising that the optimal growth temperature of BIS is higher than for pure Bi_2Se_3 .

Effect of composition

Next, we studied the effect of indium concentration in the BIS buffer on the quality of the overgrown Bi_2Se_3 film. Three samples were considered, all with buffer layers grown at a substrate temperature of 425°C : D ($x=0.3$), C ($x=0.5$), and G ($x=0.75$). In Fig. 3.17, we present AFM images and electrical properties for 50nm Bi_2Se_3 grown on these three buffer layers. From the Hall data, it is clear that the composition of the buffer does not have a strong effect on the quality of the overgrown Bi_2Se_3 film. Sample D, with the lowest indium concentration, has a slightly higher sheet density and lower mobility, but samples C and G are identical to within error bars. This is consistent with the AFM images of the overgrown films. The AFM for sample D shows many small domains, while samples C and G show reasonably large, flat domains. We therefore have the freedom to choose our buffer composition to fit our needs without drastically affecting the quality of the TI film.

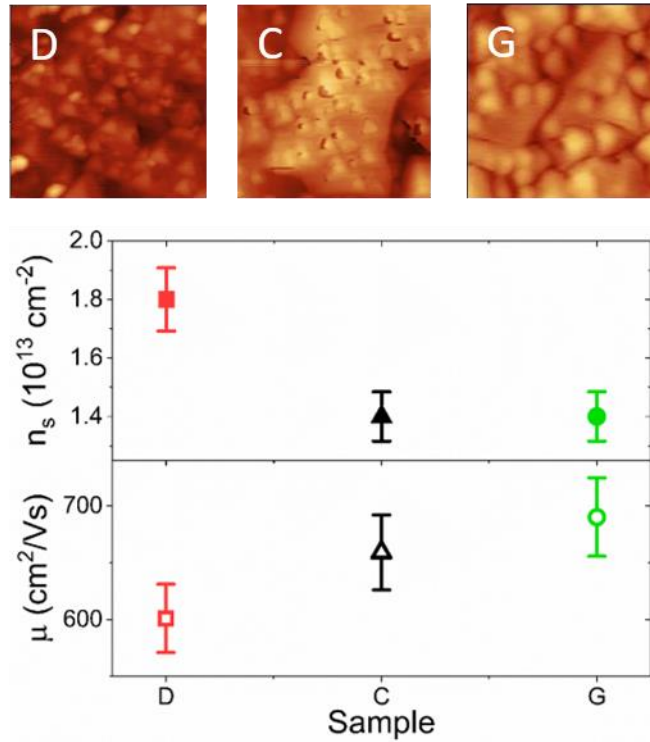


Figure 3.17. Carrier density (filled symbols) and mobility (open symbols) for sample D (red square), C (black triangle), and G (green circle). AFM images are shown at top for samples D, C, and G, as indicated. The AFM images are all $1 \times 1 \mu\text{m}$ and on a color scale of 0–40 nm. Figure used with permission from [126].

As a summary of section 3.2, we have described the growth of high-quality Bi_2Se_3 topological insulator thin films on a trivially insulating $(\text{Bi}_{1-x}\text{In}_x)_2\text{Se}_3$ buffer layer. In order to grow a flat, single-crystal film of BIS on the sapphire substrates, we used a 10QL seed layer in which 5QL of Bi_2Se_3 was grown followed by 5QL of In_2Se_3 . This bilayer was then annealed to form a BIS seed layer, after which BIS films with a variety of compositions and growth parameters were grown. BIS films grown at relatively high temperatures exhibited larger domains and overall superior morphology compared to those grown at colder temperatures. We found that Bi_2Se_3 films grown on the best quality BIS buffer layers exhibited a reduced carrier density and increased

mobility at room temperature, indicating a Fermi energy closer to the Dirac point and an overall reduction in trivial carriers. Although these films likely still contain some trivial carriers, the overall density is reduced by more than a factor of two, with significant implications for electrical and spintronic device designs. These results clearly indicate that Bi_2Se_3 films are highly sensitive to the quality of the underlying surface, despite the use of van der Waals epitaxy.

3.3 Summary

In this chapter, we discussed the optimization of the epitaxial growth of TIs. Two methods were tried on this end, the growth of BST (section 3.1) and the growth of Bi_2Se_3 on BIS buffers (section 3.2). The results of the BST growths were somewhat disappointing, as the proposed Bi_2SeTe_2 crystal configuration did not reduce the carrier density in the TI films as expected. However, we had a great success in the latter method. We established a sequential growth method to grow BIS films with enhanced quality as compared to the direct co-deposition. Then we grew Bi_2Se_3 on these quality enhanced BIS buffers. The carrier concentration reduced by more than a factor of 1/2 compared to the Bi_2Se_3 that were not grown on buffers. These results confirmed our theory that the major source of the bulk carriers in our TI films is the TI/substrate interface. Moreover, being able to grow TI films with enhanced transport properties, we are now in a better position in conducting research related to TI plasmonics and spintronics. These will be the topics of the next chapter.

Chapter 4

THE OBSERVATION OF DIRAC PLASMON POLARITONS IN TOPOLOGICAL INSULATORS

In the previous chapter, we discussed the epitaxial growth of topological insulator thin films with a $(\text{Bi}_{1-x}\text{In}_x)_2\text{Se}_3$ buffer, and we showed that the TI thin films grown with such a buffer layer have a reduced number of bulk carriers. It is now the time to move onto the ultimate goal of this dissertation: the TI spin plasmons.

Theoretically, the spin plasmons in TI surfaces are both charge density waves and spin density waves, as introduced in chapter 1. However, this statement has not been experimentally proved since the direct observation of spin plasmons is quite challenging. In the original theoretical work where the collective spin oscillations of TI surface carriers were described[49], the authors proposed to use a transient spin grating (TSG) to generate the spin wave. This method, shown in figure 4.1, two noncollinear femtosecond laser beam are needed to incident onto the surface of TI.

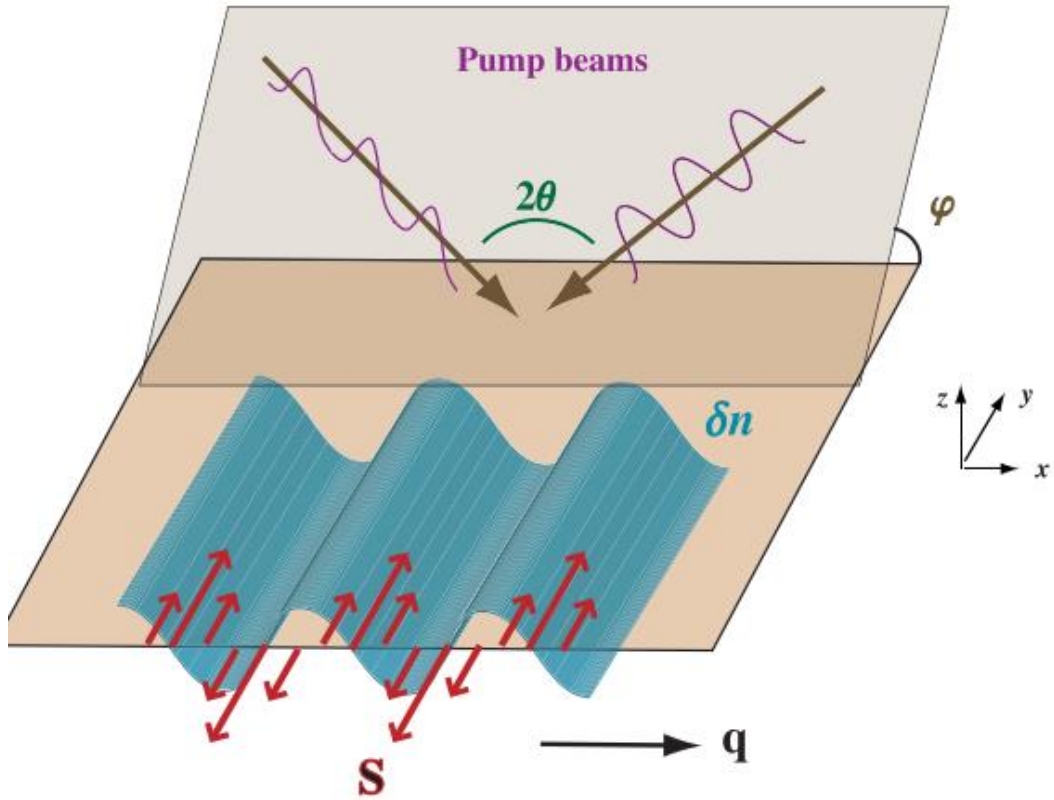


Figure 4.1. A schematic of the spin plasmon: a spin density fluctuation (green surface) and the transverse spin amplitude S (red arrows). The angles of the two incident pump beams (brown arrows and purple curves) are defined by θ and ϕ . \mathbf{q} is the grating vector required to compensate the mismatch between the plasmons and the light wavevector. Figure used with permission from [49].

In this proposal, the two pump beams are linearly polarized, and their wave vectors are defined as $(\pm\sin\theta, -\cos\theta\cos\phi, -\cos\theta\sin\phi)$. We will have to keep the two beams' polarization orthogonal and intensity equal to avoid the generation of charge density waves. The amplitude of the grating vector \mathbf{q} can be tuned by manipulating the θ and ϕ , and the relative phase between the two interfering beams. The spin plasmon

waves will be propagating along the direction of \mathbf{q} . Then reflectance measurements can be used to detect the plasmons with a probe beam. Unfortunately, we have not seen any of the experimental observations of such a detection setup. This is understandable given the complexity of the experiment and the damping of signals due to phonons, bulk carriers and other defects. For our purpose, it is then reasonable to think of the problem in the other way. Since the spin plasmons of the TI surface carriers are also charge carrier waves, we can either launch a spin wave and detect a plasmon wave or vice versa. The propagating charge density waves of TI surface electrons can also be called Dirac plasmon polaritons (DPP). As introduced in chapter 1, the way to excite DPPs will be the same as of surface plasmon polaritons (SPP) in non-Dirac systems: to use grating couplers on top of the TI surfaces and a single light beam with a polarization transverse to the grating coupler. Therefore, the experiments will be greatly simplified. Eq. 4.1 describes the wavevector q created by diffraction through a linear grating coupler with a periodicity of W .

$$q = \frac{\pi}{W} \quad \text{Eq. 4.1}$$

Figure 4.2 demonstrates a schematic of a typical device that we proposed for the excitation of Dirac plasmon polaritons. This device includes a BIS-Bi₂Se₃-BIS heterostructure epitaxially grown on an Al₂O₃(0001) substrate. The BIS layer on the bottom is the buffer layer, and the top layer serves as a protection layer to prevent surface degradation and charge redistribution caused by the metals atop the TI. The linear Au arrays with certain periodicity on the top of the thin film is the grating coupler.

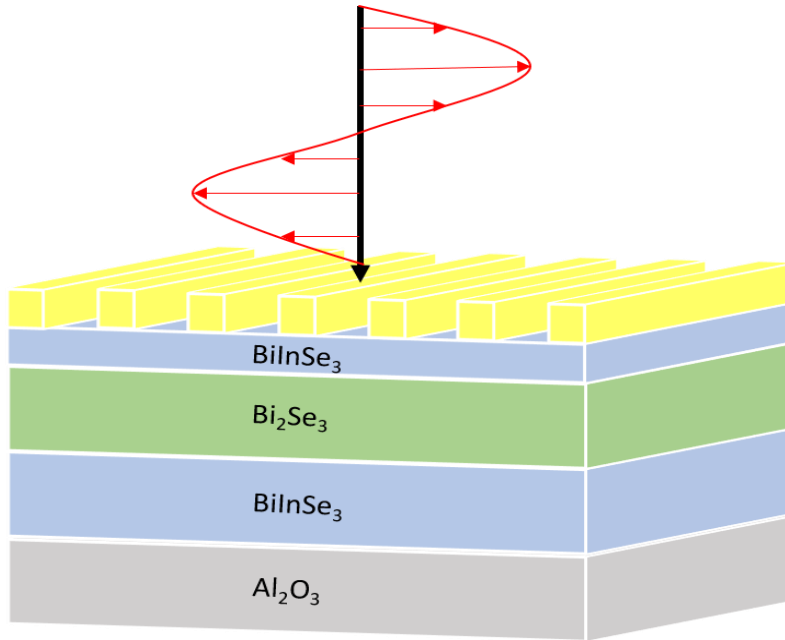


Figure 4.2. A schematic of a device for the excitation of Dirac plasmon polaritons. The black arrow is the incident light with the electric field (red curve and red arrows) polarized perpendicular to the grating couplers.

Two problems remain in such a proposal. Unlike Bi_2Se_3 , which is a well-studied material with many of the optical parameters like the bandgap and the permittivity widely reported in the literature, systematic studies of the optical properties of BIS alloy systems are underreported. This limits our ability to analyze the optical responses of the devices to the light. The other problem is that, there is no report in the observation of the DPPs with the grating coupler structures. This means that the effectiveness of such a structure in generating the DPPs is still questionable. This chapter answers questions regarding these two problems.

4.1 Optical properties of $(\text{Bi}_{1-x}\text{In}_x)_2\text{Se}_3$ thin films

To get a better understanding of the optical properties of the BIS alloy system, we conducted a series of characterizations on the epitaxial BIS films with a variety of indium content. Five films are studied in this section, denoted as A, B, C, D, and E. These films have indium concentrations (and thicknesses) of $x = 0$ (100nm), 0.32 (79nm), 0.55 (109nm), 0.73 (116nm), and 1 (100nm), respectively, as determined by RBS. The thicknesses of pure binary samples are determined by the calibrated growth rate ($\sim 1\text{nm}/\text{min}$). We used the sequential growth method for all five samples as described in chapter 3. It is worth noting that in our structural analysis, the In_2Se_3 sample is at β phase, which has a consistent crystal structure with other alloys.

4.1.1 Optical bandgaps

A Perkin-Elmer Lambda-750 UV-visible-IR spectrophotometer is used for measuring transmission spectra with normal light incidence. The transmission spectra, shown in figure 4.3, can be then analyzed to extract the optical bandgaps. The original data were in the form of transmission (percentage of light transmitted through the sample, with a unit of %). The data were then transformed into absorption coefficients,

$$\alpha = -\frac{1}{d} \ln \left(\frac{T}{T_0} \right) \quad \text{Eq. 4.2}$$

where d is the film thickness, T is the transmission through the film and the substrate, and T_0 is the transmission through the substrate only.

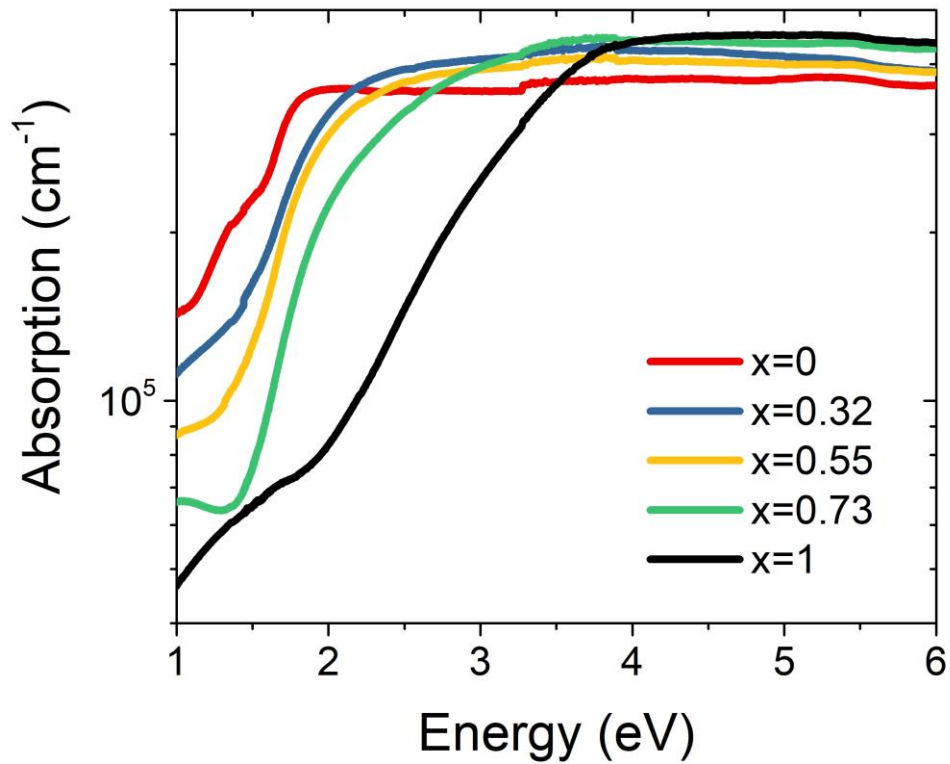


Figure 4.3. The absorption coefficients as a function of the energy of the light ranging across 1eV (visible) to 6eV (ultraviolet). x is the content of indium in the BIS alloys. Figure used with permission from [128].

As we move from lower to higher energies, the absorption coefficient increases due to absorption across the optical bandgap. It is clear in the plot that the optical bandgap increases with increasing indium content. To verify this trend quantitatively, we created the Tauc plots for all five samples. The Tauc plot method is a common practice in analyzing the optical bandgap of semiconductors[129].

The basic idea of this analysis is to plot the $(\alpha E)^{1/r}$ as a function of E , where α is the absorption coefficients, and E is the energy of the light. The value of the

exponent r depends on whether we expect a direct or indirect optical transition: $r=1/2$ for an indirect transition while $r=2$ for a direct transition. The transmission data processed in such way is supposed to appear linear. We fit the linear part of the plot with a linear function, and then the optical bandgap is determined by the interception of the fitted curve with the E (energy) axis. The Tauc plots for the five samples with both $r=2$ and $r=1/2$ are shown in figure 4.4 (a)-(j).

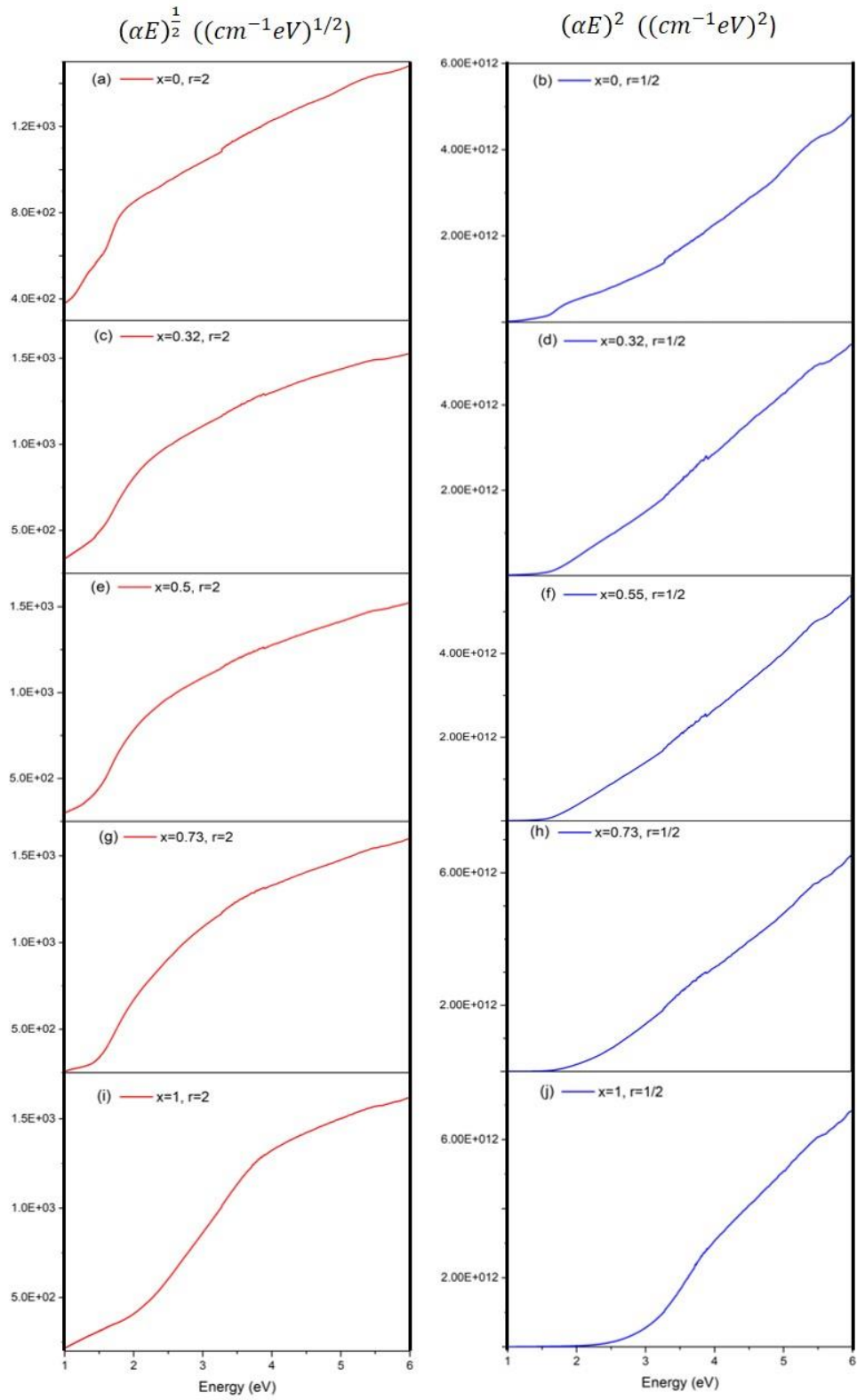


Figure 4.4. (a)-(j) The Tauc plots for all five samples with both $r=2$ (red lines) and $r=1/2$ (blue lines).

From figure 4.4, we observed both indirect and direct optical transitions for all samples; the extracted data is shown in figure 4.5. The indirect transition occurred at lower energies, while the direct transition occurred at higher energies. For sample A (pure Bi_2Se_3), the lowest energy optical bandgap is an indirect transition at 0.298eV, consistent with other results of $\sim 0.3\text{eV}$ [33]. The higher energy transition occurs at 1.26eV. There is a debate over whether Bi_2Se_3 has a direct bandgap or indirect bandgap at the Γ point[130], [131]. For sample E (pure In_2Se_3), we observe an indirect optical bandgap at 1.35eV and a direct optical bandgap at 2.46eV. The lower energy transition is consistent with results for bulk $\beta\text{-In}_2\text{Se}_3$, which has a bandgap of 1.3eV at 523K[132]. Colloidal $\beta\text{-In}_2\text{Se}_3$ sheets were reported to have a bandgap of 1.55eV[133], while sheets grown by vapor deposition have bandgaps (for thick sheets) of around 1.44eV[134]. In particular, band structure calculations for $\beta\text{-In}_2\text{Se}_3$ indicate that the fundamental indirect gap is 0.46eV, and the direct gap at Γ point is 1.76eV. However, their analysis also shows that the lowest energy direct transition at the L-point corresponds to a forbidden optical transition, leading to an optical gap much larger than the fundamental gap. Noticeably, their calculations show much lower absorption coefficients than our data at energies close to 1eV[135]. This large disagreement can be attributed to the background absorption. As the absorption from In_2Se_3 films is low, the absorption from the backgrounds gets dominant, especially when it comes to the lower energy limit of the instrument.

For BIS alloys (sample B, C, D), we observe a linear increase in both the low energy indirect and high energy direct bandgaps as the indium content increases. The

dashed lines are the linear fits to both direct and indirect gaps. The equations are given here:

$$E_{indirect} = 0.993x + 0.358 \quad \text{Eq. 4.3}$$

$$E_{direct} = 1.20x + 1.18 \quad \text{Eq. 4.4}$$

The units of the bandgaps are in eV and x is the indium content in the films. A linear shift in optical bandgap with alloy concentration is commonly observed in a variety of other semiconductor systems, including AlGaAs and InGaAs.

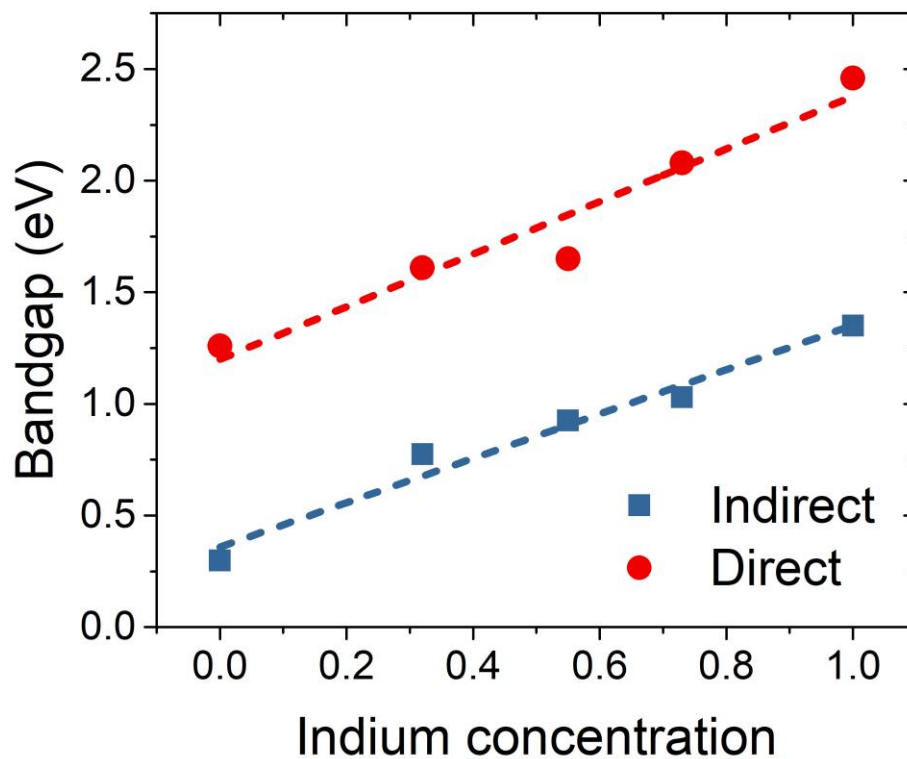


Figure 4.5. The direct and indirect bandgap as a function of indium concentration in the alloys extracted from the Tauc plots. Figure used with permission from [128].

4.1.2 The simulation of permittivity in IR

A common method to extract the frequency dependent permittivity of a material is to simulate the reflection spectra with a Drude model. In this section, we obtained infrared reflection spectra for all five samples as a function of polarization (TE, electric field parallel to the surface of the sample vs TM, electric field has a perpendicular component to the surface of the sample) and angle (25° to 55° with a step of 5°). An example of the experimental data is plotted in figure 4.6 (a) and (b), showing the reflection spectra for sample B ($x=0.32$) for TE and TM polarizations. The data for other samples have very similar curves. All the reflection spectra are showing $5\mu\text{m}$ to $15\mu\text{m}$, as the detection of wavelength shorter than $5\mu\text{m}$ is limited by the equipment ability, and the light with wavelength longer than $15\mu\text{m}$ will be strongly reflected by the Al_2O_3 substrates.

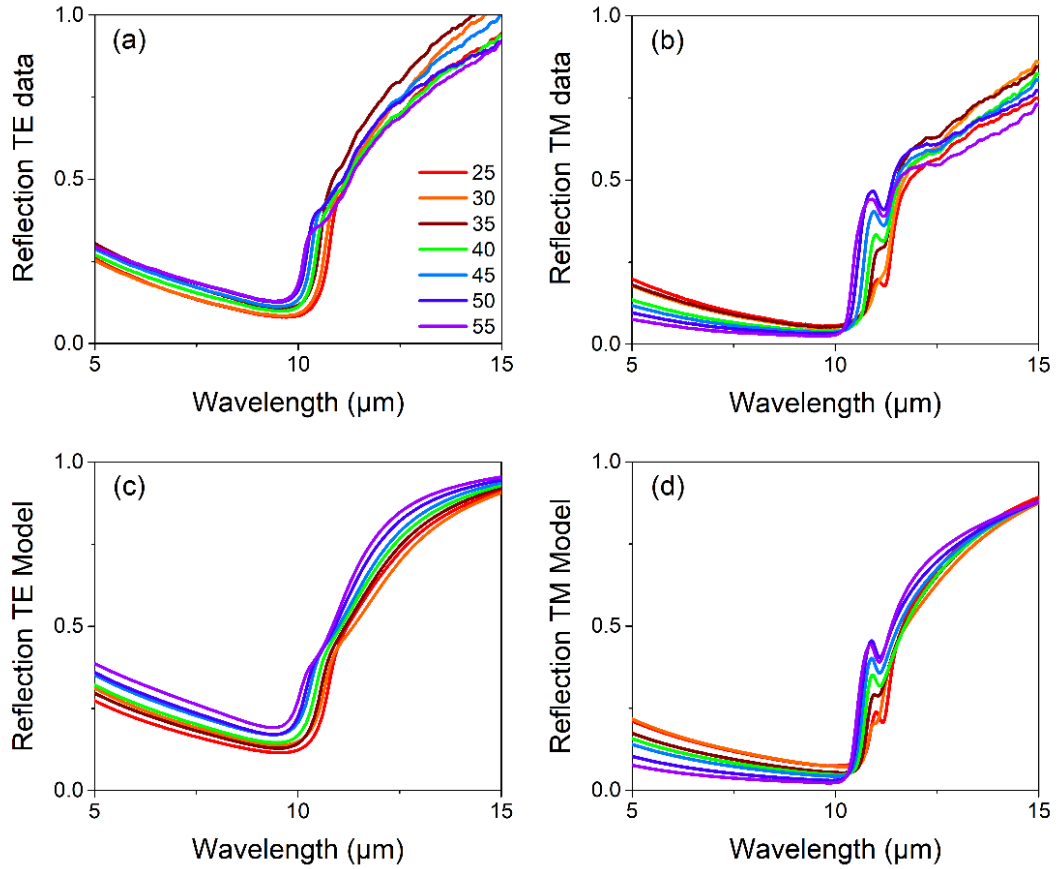


Figure 4.6. (a) Reflection spectra for sample B ($x=0.32$) with TE polarization and (b) TM polarization. (c) Fitted curve for sample B with TE polarization and (d) TM polarization at different incident angles. Figure used with permission from [128].

We modeled the optical response of the samples using a 4×4 transfer matrix method[136]. Both the permittivity of the BIS films and $\text{Al}_2\text{O}_3(0001)$ substrates were assumed to be anisotropic, with ϵ_{xy} the permittivity in the x - y plane and ϵ_z the permittivity in the z direction. Here we define the x - y plane as the hexagonally bonded plane in the BIS crystals and z direction as along the growth direction.

Unlike the common 2×2 transfer matrix method which assumes isotropic responses, elements for xy and z plane were both considered in the propagation matrix of the n th layer P_n , n is an integer:

$$P_n = \begin{bmatrix} e^{-i k_{xyn} d_n} & 0 & 0 & 0 \\ 0 & e^{-i k_{xyn} d_n} & 0 & 0 \\ 0 & 0 & e^{-i k_{zn} d_n} & 0 \\ 0 & 0 & 0 & e^{-i k_{zn} d_n} \end{bmatrix}$$

where k_{zn} is the wavevector along z direction, k_{xyn} is the wavevector along x - y plane, d_n the thickness of the n th layer. The dynamic matrix

$$M_n^{n+1} = \frac{1}{2} \begin{bmatrix} 1 + \frac{k_{xyn}}{k_{xyn+1}} & 1 - \frac{k_{xyn}}{k_{xyn+1}} & 0 & 0 \\ 1 - \frac{k_{xyn}}{k_{xyn+1}} & 1 + \frac{k_{xyn}}{k_{xyn+1}} & 0 & 0 \\ 0 & 0 & \frac{\sqrt{k_0^2 + k_{zn}^2}}{\sqrt{k_0^2 + k_{zn+1}^2}} + \frac{k_{zn} \sqrt{k_0^2 + k_{zn+1}^2}}{k_{zn+1} \sqrt{k_0^2 + k_{zn}^2}} & \frac{\sqrt{k_0^2 + k_{zn}^2}}{\sqrt{k_0^2 + k_{zn+1}^2}} - \frac{k_{zn} \sqrt{k_0^2 + k_{zn+1}^2}}{k_{zn+1} \sqrt{k_0^2 + k_{zn}^2}} \\ 0 & 0 & \frac{\sqrt{k_0^2 + k_{zn}^2}}{\sqrt{k_0^2 + k_{zn+1}^2}} - \frac{k_{zn} \sqrt{k_0^2 + k_{zn+1}^2}}{k_{zn+1} \sqrt{k_0^2 + k_{zn}^2}} & \frac{\sqrt{k_0^2 + k_{zn}^2}}{\sqrt{k_0^2 + k_{zn+1}^2}} + \frac{k_{zn} \sqrt{k_0^2 + k_{zn+1}^2}}{k_{zn+1} \sqrt{k_0^2 + k_{zn}^2}} \end{bmatrix}$$

where k_0 is the wavevector of the incident light.

Then the total matrix Q can be defined as

$$Q = M_n^{n+1} P_n M_{n-1}^n P_{n-1} \cdots M_1^2 P_1 \quad \text{Eq. 4.5}$$

The TE and TM reflection R_{ss} and R_{pp} is then calculated in the following way:

$$R_{ss} = \frac{Q_{24} Q_{41} - Q_{21} Q_{44}}{Q_{22} Q_{44} - Q_{24} Q_{42}} \quad \text{Eq. 4.6}$$

$$R_{pp} = \frac{Q_{23} Q_{42} - Q_{22} Q_{43}}{Q_{22} Q_{44} - Q_{24} Q_{42}} \quad \text{Eq. 4.7}$$

One should note that the matrix can be extended even larger if more degrees of anisotropy show up, which is beyond the topic of this dissertation.

The damped harmonic oscillator functions, Eq. 4.8, were used to model the frequency dependent permittivity of $\text{Al}_2\text{O}_3(0001)$ substrates.

$$\varepsilon(\omega) = \varepsilon_{\infty} \prod_i \frac{\omega_{LOi}^2 - \omega^2 - i\omega\gamma_{LOi}}{\omega_{TOi}^2 - \omega^2 - i\omega\gamma_{TOi}} \quad \text{Eq. 4.8}$$

where ε_{∞} is the high frequency permittivity, ω_{LO} and γ_{LO} are the frequencies and scattering rates of the longitudinal phonon modes, ω_{TO} and γ_{TO} are the frequencies and scattering rates of the transverse phonon modes. The method and corresponding parameters were adopted from M. Schubert[137], and then slightly refined with our transfer matrix method to fit the reflection data on the substrates that we used for the BIS growths. The correlation coefficients between the fitted curve and the raw data were used as indicators of fitting reliability. In the case of Al_2O_3 substrates, the correlation coefficients are 0.9984 and 0.9983 for TE and TM polarizations, respectively. This shows good agreement in the simulation and the data. As an example of the data compared with simulation, we plotted both the data and simulation results of TE reflection for 45° reflection of the substrate in figure 4.7.

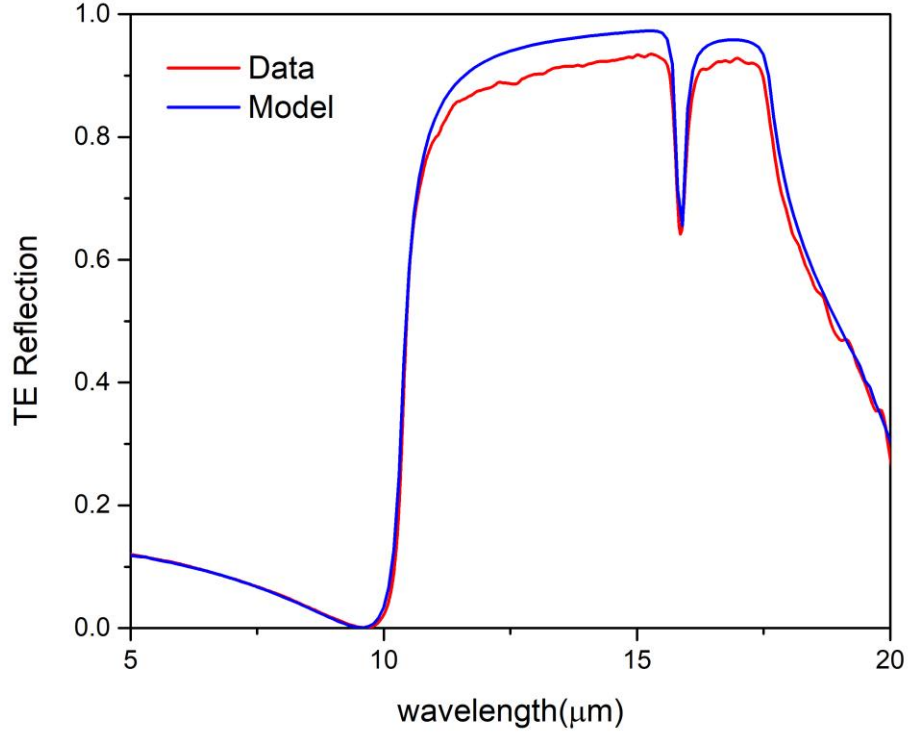


Figure 4.7. The data (red line) and simulation results (blue line) of the 45° TE reflection of a substrate.

With the refined permittivity of sapphire substrate, the permittivity of BIS films can be then simulated with a Drude model, with a BIS/sapphire configuration.

The Drude model is described in Eq. 4.9.

$$\varepsilon(\omega) = \varepsilon_{\infty} \left(1 - \frac{\omega_D^2}{\omega^2 + i\gamma_D \omega} \right) \quad \text{Eq. 4.9}$$

where ε_{∞} is the high frequency permittivity, ω_D the Drude frequencies, and γ_D the Drude losses. All the BIS films were treated as anisotropic, with different fitting parameters for the x - y plane and z direction. The geometry of the modelling is a layer of BIS film with experimentally determined thickness and a layer of 0.5mm

Al₂O₃(0001) substrate embedded in two semi-infinite air layers. Table 1 shows all the parameters obtained from the data modelling. For each parameter of each sample listed in the table, mean values and the standard deviations (SD) among all seven incident angles were calculated. The units of all the frequencies and losses are cm⁻¹. Again, the correlation coefficients between the fitted curve and the raw data were used as indicators of fitting reliability. We tried to refine the parameters to get the correlation coefficients as close to 1 as possible. The smallest correlation coefficient we got in the fitting is 0.9906, occurring in Bi₂Se₃ TM 40°. Most of the correlation values lie around 0.998, which means a good agreement between the data and the fitted curve. Examples of the fitted curves are shown in Fig. 4.6(c) for TE polarization and 4.6(d) for TM polarization. One may notice larger deviations from the experimental data when the wavelength gets close to 15µm. That is the region over which the sapphire substrate becomes close to 100% reflective. The reflection data in that region is therefore somewhat noisier, leading to a slight deviation from the predicted reflection data.

Table 4.1. Mean values and standard deviations of all the fitting parameters for all the samples.

	Bi ₂ Se ₃		(Bi _{0.70} In _{0.32}) ₂ Se ₃		(Bi _{0.49} In _{0.55}) ₂ Se ₃		(Bi _{0.26} In _{0.73}) ₂ Se ₃		In ₂ Se ₃	
	Mean	SD	Mean	SD	Mean	SD	Mean	SD	Mean	SD
$\varepsilon_{\infty,xy}$	22.4	0.6	15.3	0.8	12.3	1.5	9.7	0.8	5.0	0.2
$\omega_{D,xy}$	315	32	277	38	201	48	111	13	207	63
$\gamma_{D,xy}$	696	183	799	93	897	37	346	125	548	90
$\varepsilon_{\infty,z}$	26.5	2.0	24.2	1.8	23.2	1.1	17.8	1.9	16.9	1.4
$\omega_{D,z}$	914	18	908	10	906	8	918	16	918	13
$\gamma_{D,z}$	67	38	60	27	55	23	67	23	54	19

In figure 4.8, we show the x - y and z direction high frequency permittivities plotted as a function of the indium concentration. In one case, the error bar is smaller than the size of the data point. As can be seen from this figure, within the error bars the high frequency permittivity decreases linearly with indium concentration for both x - y plane and z direction. We do not see a similar trend for Drude frequencies or Drude losses shown in Table 4.1. For $\omega_{D,z}$ and $\gamma_{D,z}$, the values are relatively constant across all indium concentrations. For $\omega_{D,xy}$ and $\gamma_{D,xy}$, however, the values do change with concentration but not with any particular trend. The x - y Drude frequency in particular is quite far away from the fitting range. As such, the model is not very sensitive to the precise values of these parameters.

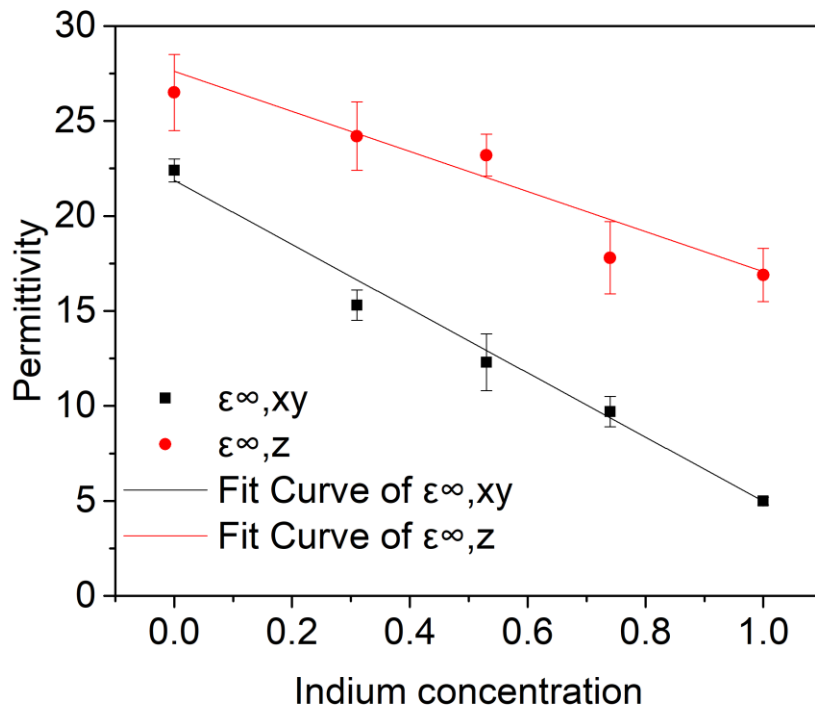


Figure 4.8. The fitted high frequency permittivity as a function of indium concentration. The black and red lines are the linear fittings of $\epsilon^{\infty,xy}$ and $\epsilon^{\infty,z}$, respectively. Figure used with permission from [128].

We compared our high frequency permittivity values for pure binary Bi_2Se_3 and In_2Se_3 to those reported in the literature. Different methods have been used to approximate the optical response of these materials, and the optical data were measured with different techniques, making these results inconsistent. In some electrical transport studies, the static dielectric constant of Bi_2Se_3 is taken to be extremely large, approximately 100[138], [139]. Some optical studies have reported 29[140] and ~ 25 [141] for $\epsilon_{\infty,xy}$ of Bi_2Se_3 , much closer to what we have derived (22.4). While we are reporting a larger value of 26.5 for $\epsilon_{\infty,z}$, other reports indicate smaller values of ~ 17.4 [141]. When it comes to indium selenide, discussions of the same phase and polytype ($\beta\text{-In}_2\text{Se}_3$) are limited. There is a publication where $\epsilon_{\infty,xy} = 9.53$ is extracted from far-IR ($>25 \mu\text{m}$) reflection spectra for $\alpha\text{-In}_2\text{Se}_3$ single crystal[142]. Another paper reported values of 9.51, 7.23 and 8.09 for α , β and $\gamma\text{-In}_2\text{Se}_3$ single crystals, respectively[132]. Among all three polytypes, their value for $\beta\text{-In}_2\text{Se}_3$ is the closest to that we observe, which is consistent with our structural evidences showing that we are growing the β type.

4.2 The observation of the Dirac plasmon polaritons

From the discussion of the previous chapter, we now have a better understanding of the optical properties (optical bandgaps and frequency dependent permittivity) of the epitaxial BIS films, which answers the first question raised in the beginning of this chapter. This section is to answer the second question: can we generate and observe Dirac plasmon polaritons in TIs?

There have been multiple works reporting the observation of the Dirac plasmons in TIs[46]–[48]. However, these studies mainly focused on the localized modes which were enabled by etching the TI films into stripe arrays. We believe that

the Dirac plasmon modes that were observed in their research are not propagating, thus not applicable in the study of the spin plasmons. As was stated in the beginning of the chapter, we propose to use a grating coupler to generate DPPs on top of a multilayer structure. Some studies have shown that the grating coupler method successfully generates DPPs in graphene[6], [143].

We first grew a series of 50nm Bi_2Se_3 films. The films had the following configuration: a layer of 5nm BiInSe_3 (BIS) on the top, 50nm Bi_2Se_3 TI in the middle, and 50nm BIS buffer layer between the TI and the $\text{Al}_2\text{O}_3(0001)$ substrate as shown schematically in figure 4.2. After growth, 100nm gold/10nm titanium gratings with different grating periodicity are fabricated on the surface of the film using standard techniques including photolithography, electron beam lithography, electron beam deposition, and liftoff (for a description of the fabrication process, please see chapter 2). The period of the gratings ranges from 400nm to 700nm. The width of the metal stripes was kept at 50% of the grating period for all samples. Figure 4.9 shows an SEM image of a typical sample with a grating period of 550nm.

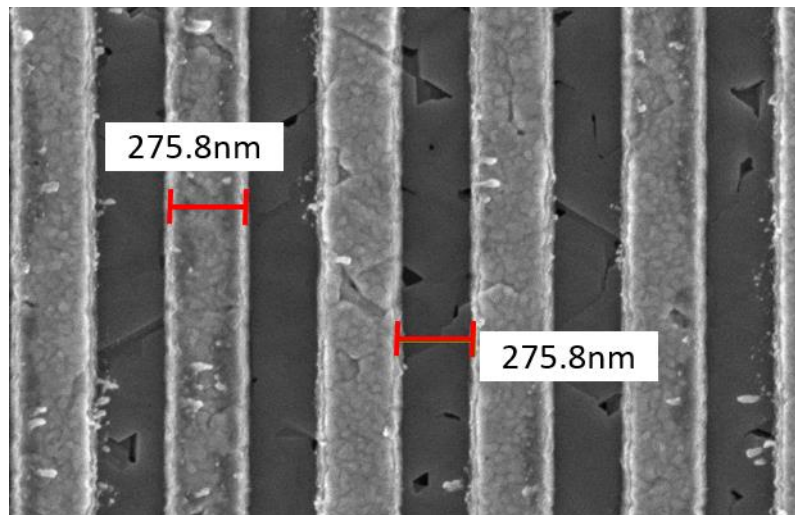


Figure 4.9. An SEM image of a typical sample with a grating period of 550nm.

After patterning, TM transmission spectra (the electric field perpendicular to the grating couplers) were taken with our FTIR system. Spectra were normalized to transmission through an unpatterned sapphire substrate.

The TM extinction spectra for the samples with grating periods of 400nm (sample A, black diamond), 450nm (sample B, green up-triangle), 500nm (sample C, blue circle), 550nm (sample D, yellow square) and 700nm (sample E, red hexagons) are shown in figure 4.10. The extinction spectra were calculated by Eq. 4.10:

$$E = 1 - \frac{T_S}{T_{sub}} \quad \text{Eq. 4.10}$$

where T_S is the transmission of the sample, and T_{sub} is the transmission of the substrate.

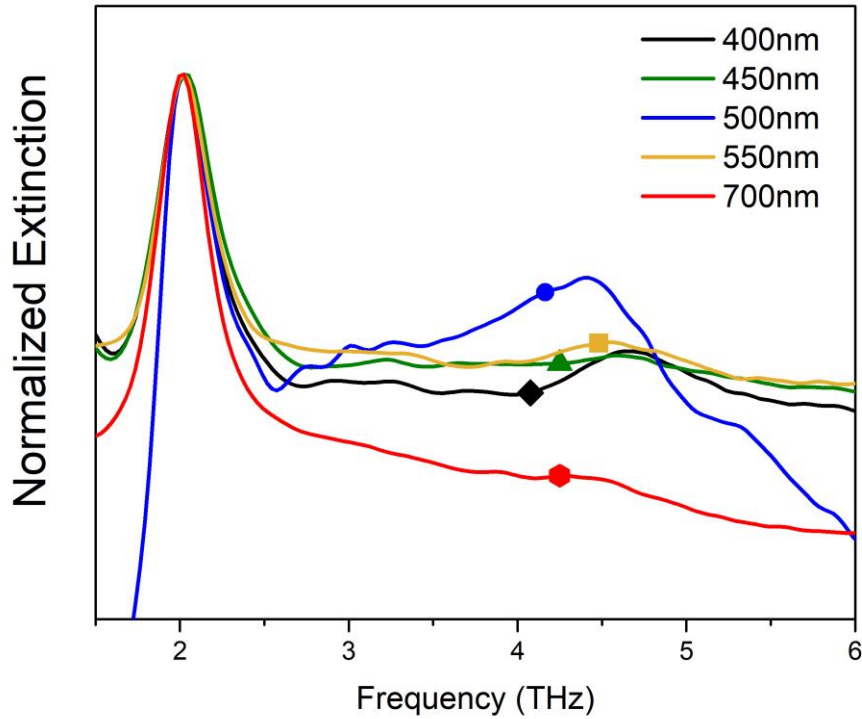


Figure 4.10. The normalized extinction spectra for samples A-E.

Since the gold gratings are covering half of the surface of the film, the extinction spectra are always above 0.5. The largest absorption feature is the α -phonon of Bi_2Se_3 appearing near 2THz. In order to make the plasmon absorption peak more obvious, we normalized the extinction spectra to the extinction of the α -phonon peak as shown in Eq. 4.11:

$$E = \frac{1 - \frac{T_S}{T_{sub}}}{E_\alpha} \quad \text{Eq. 4.11}$$

where E_α is the extinction of the sample at the α phonon frequency.

In figure 4.10, we see a series of peaks shifting to lower frequencies as the grating periodicity increases. This behavior is consistent with expectations for Dirac plasmons: as the grating period increases, the wavevector decreases, which will cause the plasmon frequency to decrease (recall chapter 1, Eq. 1.4). The zoomed in spectra for all the samples A-E in the range of 3-5THz can be found in figure 4.11. The colored arrows are indicators of the peak positions of each spectrum.

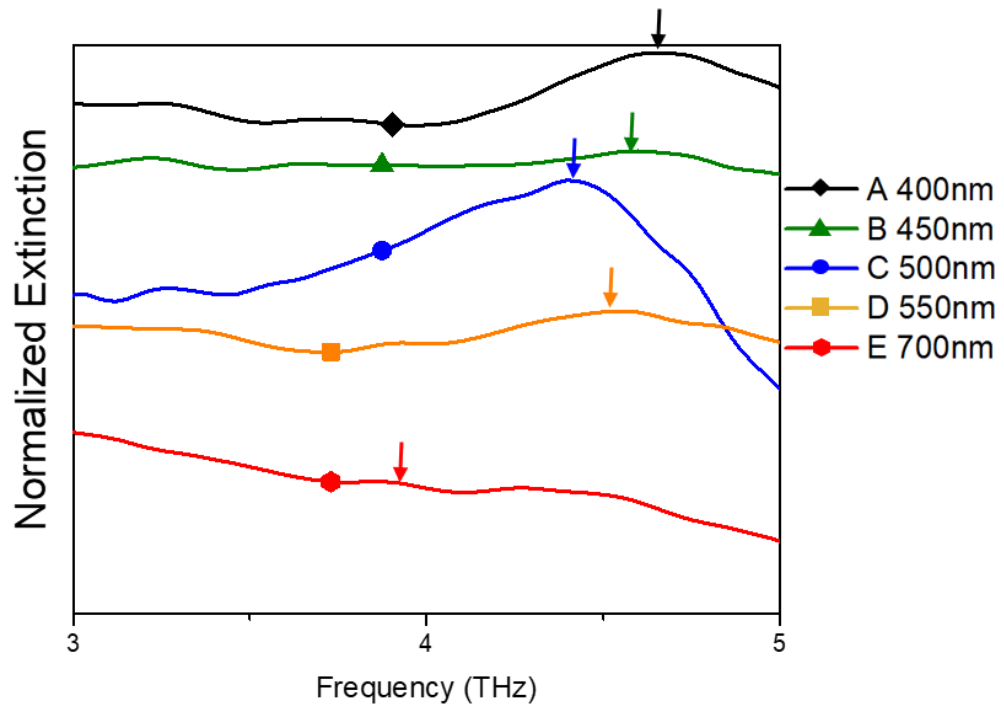


Figure 4.11. The zoomed in of the extinction spectra for samples A-E in the range of 3-5 THz. Data are offset so each peak can be seen clearly. Colored arrows are the maxima of each spectra around the probable DPP frequency.

Although these results are consistent with propagating DPPs, we must rule out any confounding effects. We therefore performed measurements on a series of control

samples. These included a bare sapphire substrate with 500nm grating (sample F), a 50nm BiInSe₃ film grown on sapphire with no grating (sample G), and a complete multilayer film with no grating (sample H). The extinction spectra for samples F (red down-triangle), G (blue pentagon) and H (black star) are shown in figure 4.12. For samples F and G, we do not observe any distinct peaks. For sample H, we see two peaks at ~2THz and ~4THz, which can be attributed to the α and β phonons, respectively, in the multilayer sample. These phonon frequencies are fixed by the material and will not change with the grating period.

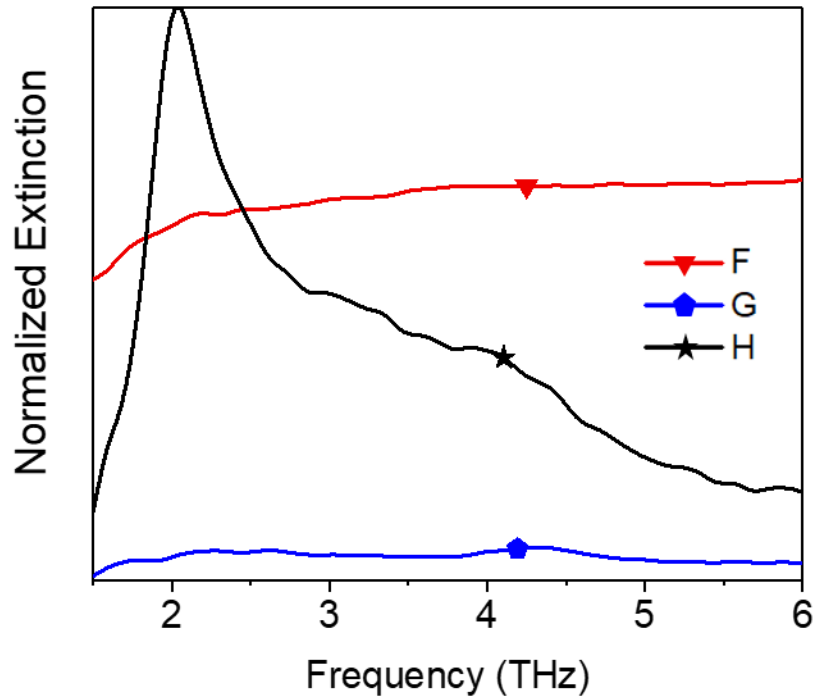


Figure 4.12. Extinction spectra for sample F-H.

By comparing the extinction spectra for the samples shown in figure 4.10 and 4.11 with that of sample F, we can conclude that the absorption peaks in figure 4.10 and 4.11 do not arise from a pure grating coupler diffraction mode. If they did, we would expect to observe a peak in the extinction spectrum of sample F. The extinction spectra for samples G and H indicate that the absorption peaks that we observe in samples A-E above ~ 2 THz are not from the bare materials but are caused by an interaction of light with the grating. Hence, a propagating plasmon mode would be the most probable explanation for the extra absorption peaks that we see in the terahertz range.

In order to be sure that these absorption peaks are caused by the excitation of DPPs, we need to plot the dispersion of the mode position. As there are no detailed models of the shape of a coupled propagating DPP mode, the peak positions were determined by picking the maxima of the extinction spectra indicated by the colored arrows shown in figure 4.11. In 4.11, the spectra are offset so that each sample can be distinguished easily. These extracted peak positions are plotted as colored symbols in figure 4.13. They are compared to the theoretical dispersion curve, shown as a gray line.

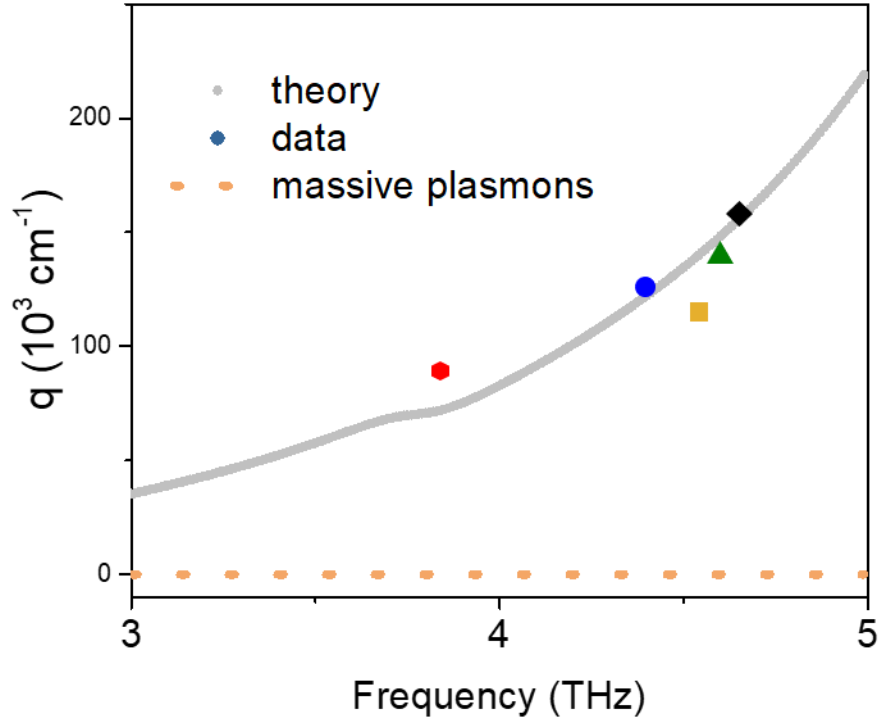


Figure 4.13. Dispersion relation (wavevector q as a function of frequency) of data extracted from extinction spectra in figure 4.11 (color dots), simulation results for coupled Dirac plasmons (gray line), and simulation results for 2D massive plasmons (orange line).

The theoretical dispersion curve is generated from the dispersion relationship for the optical mode for coupled Dirac plasmons. Eq. 1.3 describes the dispersion for a Dirac plasmon excited from a single surface, like graphene. In the case of a 50nm TI thin film, a coupling term that considers the contribution from both the top and bottom surfaces will be needed as discussed in chapter 1. Recall the coupled Dirac plasmon dispersion relation in Eq.1.5:

$$\omega_{Dirac}^2 = \frac{e^2}{4\epsilon_0\epsilon_r} \frac{v_F\sqrt{2\pi n_D}}{h} \frac{q}{\epsilon_T + \epsilon_b + q\epsilon_{TI}d} \quad \text{Eq. 1.5}$$

where ϵ_T is the permittivity of the material on top of TI, ϵ_B the permittivity of the material below the TI, ϵ_{TI} is the permittivity of the TI material itself, and d is the thickness of TI thin film. For our TI films, the thickness d is 50nm, the Fermi velocity $v_F = 5.0 \times 10^5 m/s$, and the carrier density $n_D = 1.4 \times 10^{13} cm^{-2}$ from room-temperature Hall measurements [48]. The frequency-dependent permittivity of the TI thin film is generally well-known. However, the permittivity of the BIS material in the terahertz regime is less well-known; this material is found both above and below the TI.

In the previous section we modeled the permittivity of BIS. However, the data were simulated in the range of 5-15 μm , which were not as helpful as we expected in this case. Since the BIS layers are much thinner than the wavelength of the terahertz light, it is likely that the excitation samples both the BIS permittivity as well as the permittivity of the sapphire substrate and the permittivity of the air/gold grating. This adds an additional complexity in determining the effective permittivities above and below the TI thin film. In addition, we expect that the grating coupler will influence the effective permittivity of the material above the TI in an unknown way. Thus, a simplified method is shown here: rather than guessing at the magnitude of these effects, we chose to use a constant value of the effective permittivity, ϵ_{eff} , as shown in Eq. 4.12.

$$\omega_{Dirac}^2 = \frac{e^2}{4\epsilon_0\epsilon_r} \frac{v_F\sqrt{2\pi n_D}}{h} \frac{q}{\epsilon_{eff} + q\epsilon_{TI}d} \quad \text{Eq. 4.12}$$

Through the simulation, we found that the theory fits the best with data at $\epsilon_{eff} = 20.3$, with a correlation value of 0.90. The simulation results with $\epsilon_{eff} = 20.3$ are plotted in figure 4.12 as the gray line, while the extracted resonance frequencies are shown as filled symbols. Each symbol represents the sample with the same color

as shown in figure 4.10 and figure 4.11. Despite the fact that the permittivity of BIS in this frequency range (1THz~6THz) will be largely affected by the phonon modes, the effective permittivity that we derived from our plasmon simulation is similar to what we extracted from the IR data. For detailed information, please see section **3.2**.

Furthermore, to demonstrate that we are not exciting the 2D massive plasmons resulted from the 2D electron gas on the TI surface, we plotted the dispersion relation of 2D massive plasmons, shown as the orange line in Fig. 3(b). The line was created according to Eq. 1.2:

$$\omega_{massive}^2 = \frac{e^2}{4\epsilon_0\epsilon_r} \frac{n_M}{m^*} q \quad \text{Eq. 1.2}$$

where n_M is the density of the 2D massive electrons ($1.4 \times 10^{13} \text{ cm}^{-2}$) with an effective mass of m^* ($1.37 \times 10^{-31} \text{ kg}$). We used $\epsilon_r = \frac{\epsilon_{eff}}{2}$ as an approximation of the average permittivity of the materials surrounding the 2D electrons. It is shown that the plasmon modes that we were seeing are not likely to be the 2D massive plasmons, since the wavevectors of the 2D massive plasmons are orders of magnitudes lower than that of the coupled Dirac plasmons. The density of the 2D carriers would need to be unrealistically low to get close to the experimental data.

We can see in figure 4.13 that the experimental resonant positions match reasonably well with the theoretical curve (gray line). The sample with a 500nm grating width does deviate somewhat from the expected value. We do not believe this is caused by an incorrect grating period as these were all checked using scanning electron microscopy as shown in figure 4.9. It is likely that this deviation is caused by measurement difficulties. The frequencies of the plasmons that we are launching fall into the same range as the β phonon of Bi_2Se_3 (~4THz); interactions between the plasmon and phonon could make it more difficult to extract the plasmon peak position.

This will be especially problematic as the grating period increases and moves the plasmon resonance closer to the β phonon frequency.

In addition, the signal to noise ratio of the data is limited by the FTIR instrument in this frequency range, which also makes it difficult to determine the exact position of the peak. One way to mitigate this difficulty would be to try to launch the plasmons in a different frequency regime where the optical measurements are easier. However, shifting the plasmon frequency is likely to be challenging. According to the simulated dispersion relation of the DPP, we would need a grating with a smaller period ($<400\text{nm}$) to push the plasmon to higher frequencies, which is challenging in terms of device fabrication. The sapphire substrates are also not transparent above $\sim 8\text{THz}$, so measurements at these frequencies would require shifting to a different substrate. Pushing the plasmon frequency lower to below the α phonon ($\sim 2\text{THz}$) would also be difficult since a grating in the range of micrometers is required, which will cause large grating diffraction features in the terahertz range. Such effect is shown in figure 4.14.

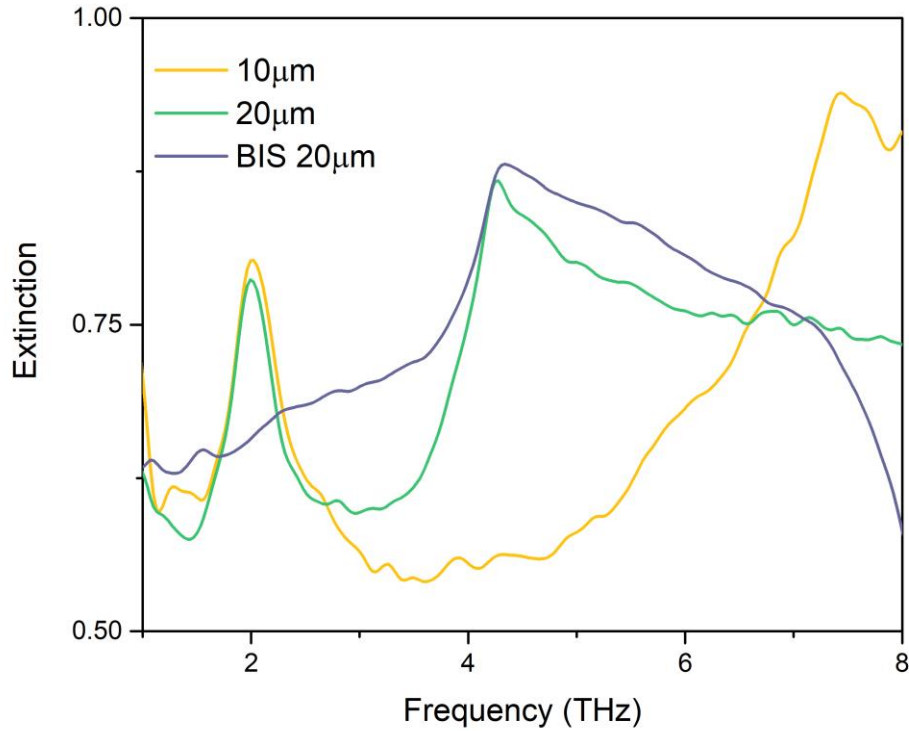


Figure 4.14. The extinction spectra for sample I (yellow line), J (green line) and K (blue line).

The extinction spectra for three samples were plotted: sample I (yellow line), a BIS/BS/BIS structure with a grating period of $10\mu\text{m}$; sample J (green line), a BIS/BS/BIS structure with a grating period of $20\mu\text{m}$; sample K (blue line), a single layer 50nm BIS with a grating period of $20\mu\text{m}$. In all three samples we see a large extinction peak higher than 4THz . By comparing this peak of I and J, we see a similar shifting trend as was discussed previously. We used to be confused by these set of peaks as they resembled the actual DPP peaks. However, by comparing J and K, we can clearly conclude that this set of peaks exist no matter whether the TI layers are

present. Thus, this set of extinction peaks cannot be from the DPPs. Instead, we attribute these peaks to the pure effect of the grating couplers.

Despite the limitations in our optical data, the good match between experiment and theory indicates that we have successfully demonstrated the launching of propagating DPPs in TI thin films.

4.3 Summary

Section 4.1 and 4.2 answers the two questions that were raise at the beginning of this chapter. We demonstrated the optical properties of the epitaxially grown BIS films, providing a good understanding of the optical responses of such a material system. We demonstrated the launching and observation of the Dirac plasmon polaritons in TI thin films, enabling us to detect the spin plasmons with a simplified pump-probe method.

In the next chapter, we will move onto the direct detection of the correlated propagating spin wave by a magneto-optics Kerr effect (MOKE) system. Other applications of the TIs in some of the collaborative projects will also be discussed in the next chapter.

Chapter 5

THE SPIN PLASMONS

In the previous chapter, we demonstrated the excitation and detection of Dirac plasmon polaritons in the THz range, which are also propagating spin plasmons theoretically. In this chapter, we will introduce our methods in the direct observation of the propagating spin plasmons.

Figure 5.1 shows a simple schematic of the proposed spin plasmon detection method. Based on the discussions in chapter 4, a grating coupler (yellow stripes)/TI sample (green bulk) and a THz beam (red curves) will be used for the excitation of propagating Dirac plasmons on the surface of the TI. This time, only half of the sample will be covered by gold gratings, allowing the propagation of the plasmon wave (black arrow and black curve) into the bare part of the sample for a certain distance. Then the spin features of the propagating plasmon wave can be detected by a probe beam with a magneto-optical Kerr effect (MOKE) setup. Detailed introductions about the THz source and the MOKE system will be found in the following sections (section **5.1** and **5.2**). Although persuasive evidences have not been found in our experiments, some analysis of the current progress will be provided in section **5.3**.

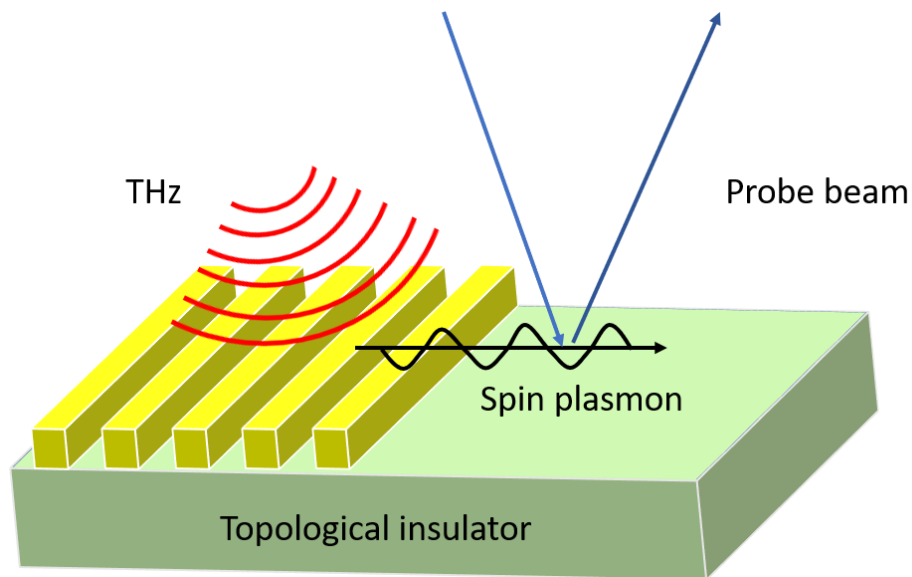


Figure 5.1. A schematic of the spin plasmon detection method.

5.1 THz source

In chapter 4, we launched and detected the propagating Dirac plasmons with an FTIR instrument where an IR beam with a wide spectral range (including THz) was used. On the one hand, such a method greatly reduced the difficulty in setting up the measurements. On the other hand, the intensity of THz in this IR beam is so weak that a low scan speed and thousands of rounds of scans were needed to improve the signal-to-noise ratio. For example, each of the extinction spectra shown in figure 4.10 and 4.11 took ~20 hours, while the analysis of the plasmons were still disturbed by noises. A specialized THz emitter will be needed to make the plasmons easier to be detected.

Among many of the techniques using different ways to generate THz radiation, photoconductive emitters have been popular for their high efficiency in converting visible/near-IR pulses to THz radiation[144]–[146], and have been widely used for THz spectroscopy and imaging[147]–[149]. In this technique, electron-hole pairs are

generated in the semiconductor crystal using an above-band gap femtosecond pulse, and these photoexcited carriers are then accelerated by an applied electric field. The physical separation of the electrons and holes forms a macroscopic field opposite to the biasing field. The fast rise and decay of this electric field produces a transient current, which generates a pulse of electromagnetic radiation in the THz frequency range[149]. Low temperature grown (LT) GaAs or InGaAs is widely used as the semiconductor in these photoconductive emitters due to high dark resistivity and short photocarrier lifetimes (<1ps).

Following this path, we used a commercial photoconductive THz emitter from BATOP Optoelectronics. This product is designated to have a THz emission from 0.2THz to ~4THz with a pulsed laser of ~800nm (~100fs pulse duration, 100MHz repetition rate), and a bias voltage of 10V. A FemtoFiber pro NIR laser from TOPTICA Photonics was used to generate a pulsed laser with a wavelength of 780nm, a pulse duration of <100fs, and a repetition rate of 80MHz. A schematic of the THz emission setup is shown in figure 5.2.

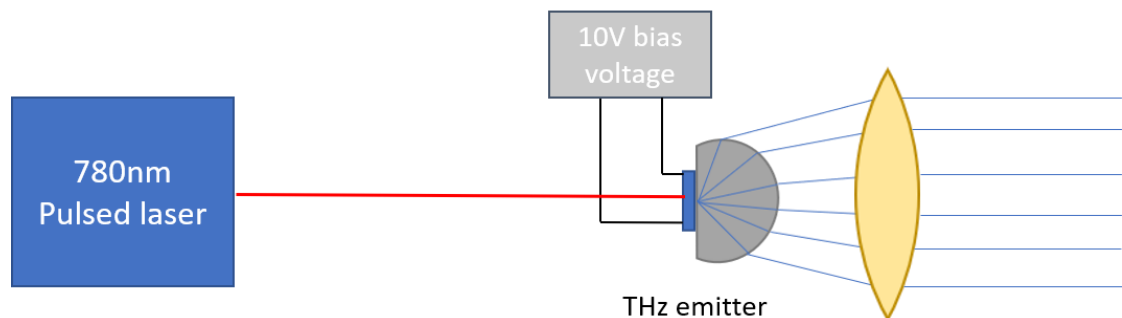


Figure 5.2. A schematic of the THz emission setup.

5.2 Magneto-optical Kerr effect (MOKE)

The magneto-optical Kerr effect was originally described by John Kerr in 1877, in his article *On Rotation of the Plane of Polarization by Reflection from the Pole of a Magnet*[150]. The title itself describes what he observed in his early experiments. In a view of the present day, this effect can be described as such: light that is reflected from a magnetized surface can change in polarization and intensity[151]. A schematic of the Kerr effect is shown in figure 5.3. To quantitatively describe the rotation of the polarization, a complex Kerr angle is introduced as $\Phi_K = \theta_K + i\epsilon_K$, where θ_K is the change in rotation angle, and ϵ_K is the change in ellipticity. Measurements of the Kerr rotation angle will give us information about the magnetization of materials. Depending on the orientation of magnetization relative to the plane of incidence and the orientation of the polarization of light, three fundamental types of geometries are defined: longitudinal (magnetization parallel to both the incident plane and the reflection surface), polar (magnetization perpendicular to the reflection surface but parallel to the incident plane), and transverse MOKE (magnetization perpendicular to the incident plane but parallel to the surface).

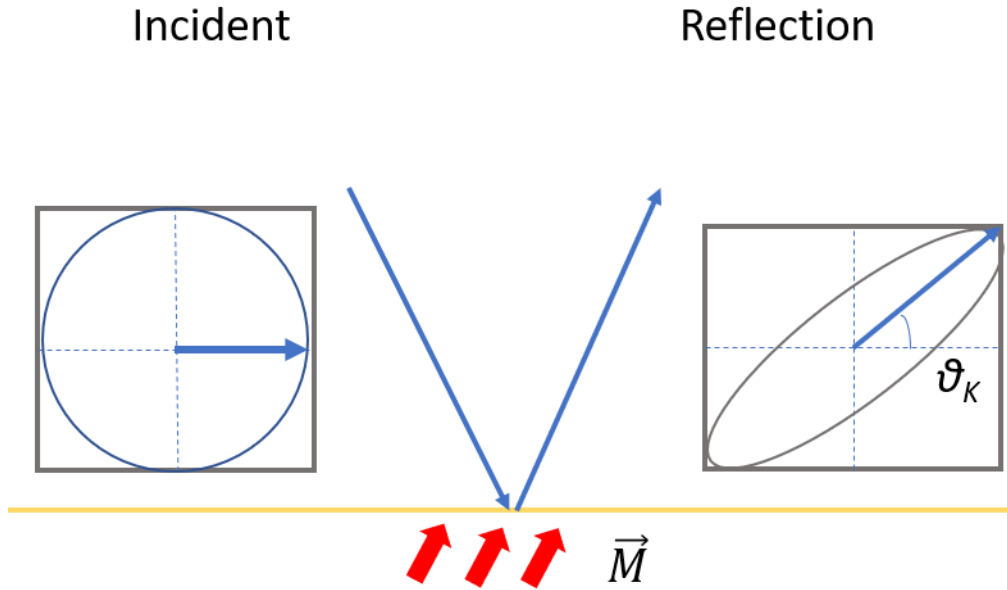


Figure 5.3. A schematic showing the Kerr rotation angle θ_K of a light beam reflected from a surface with a magnetization \vec{M} .

MOKE has given rise to many applications, such as magneto-optical drives[152], and magneto-optical microscopy for imaging magnetic domains[153]. More importantly, time resolved MOKE measurements have been widely used in spin dynamics studies where spin features on a time scale of femtoseconds are observed[154]–[156]. In these studies, a ‘pump’ laser beam is used to trigger excitation in the samples, and then a ‘probe’ laser beam is used to detect the Kerr rotation after reflection from the sample at a certain time delay[156]. Time resolved MOKE enables us to study the spin features of a sample on a femtosecond-picosecond time scale, making it a promising technique for the observation of spin plasmons. In this dissertation, we will describe the development of a time resolved THz-MOKE setup to study the spin plasmons in TIs.

A simplified schematic of the MOKE measurement setup is shown in figure 5.4. A 780nm femtosecond laser beam (pulse duration <100fs, repetition rate 80MHz) is generated by a FemtoFiber pro NIR laser from TOPTICA Photonics. The laser beam is separated into two beams by a beam splitter: one for THz emission (THz line), and the other for MOKE detection (MOKE line). The THz emission part was discussed in section 5.1. A delay line was used on the MOKE detection beam to control the time delay between the THz line and the MOKE line. The polarization of the MOKE line is set to s-polarization (electric field perpendicular to the incident plane) by a polarizer. After reflection from the samples, the beam is then decomposed into two beams with s-polarization and p-polarization (electric field parallel to the plane of incident on the TI sample). The difference of intensity between the two beams are detected by a balanced detector to determine the Kerr rotation of the TI samples.

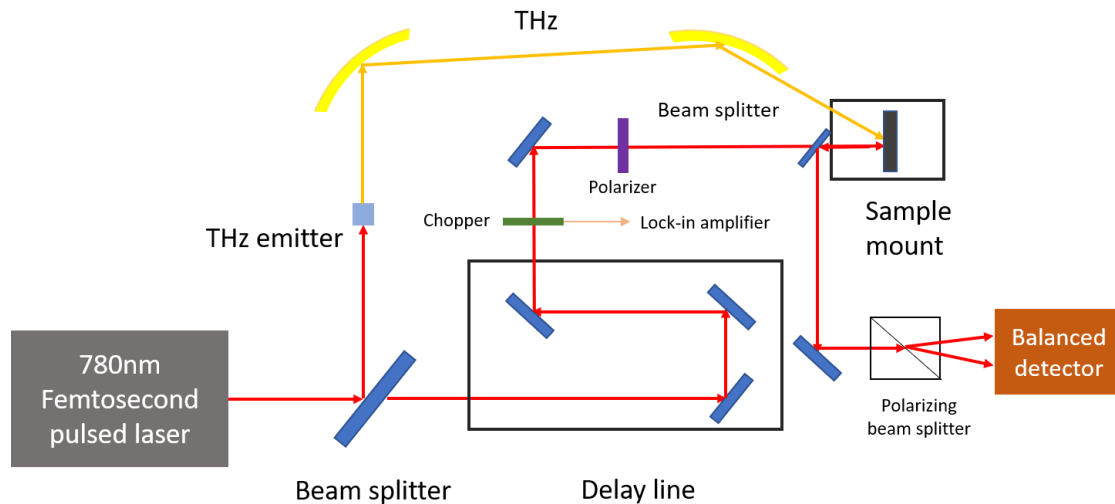


Figure 5.4. A simplified schematic of the MOKE measurement setup.

For the simplicity of understanding the measurement, now we consider an ideal case: a sinusoidal propagating spin plasmon wave. The frequency of the spin plasmon wave will be the same as the Dirac plasmon that we discussed in the last chapter. Figure 5.5 is created with an assumption of a sinusoidal wave function with a frequency of 4THz (250fs, 75 μ m). The Kerr rotation as a function of time delay is also expected to be a sinusoidal function.

As is shown in figure 5.5, we can either scan the sample with a fixed delay time (5.5 (a)) or scan the delay time at a fixed distance from the grating couplers (5.5(b)). In figure 5.5, d_1, d_2, d_3, d_4 are different distances from the gold grating couplers, and t_1, t_2, t_3, t_4 are different delay times between the THz line and MOKE line. We are expecting the MOKE signals to be sinusoidal functions of both the distance (at a fixed delay time t_1) and the delay time (at a fixed distance d_1). Even if the assumption of sinusoidal function is not accurate, and a decay of the spin oscillation intensity is present, we will still be able to map out the MOKE signals as a function distance and delay time by such a method.

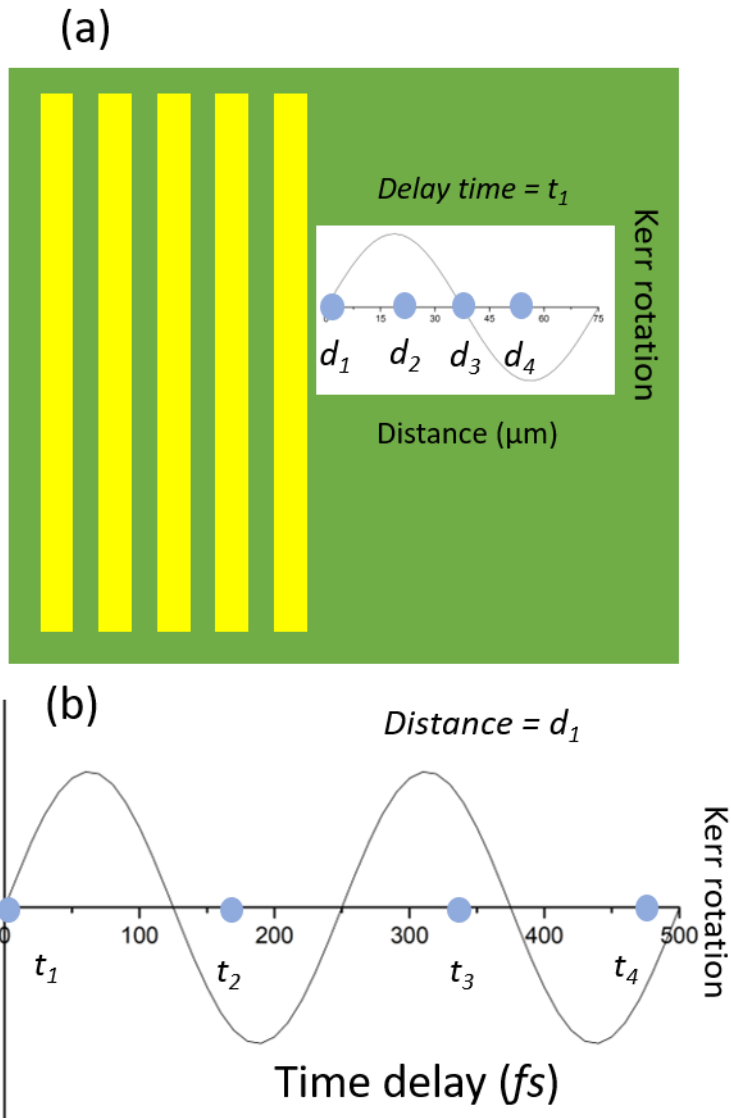


Figure 5.5. Expected MOKE signal – delay time function assuming sinusoidal spin wave. (a) Scanning of the distance at a fixed time delay t_1 . (b) Scanning of the delay time at a fixed distance d_1 .

5.3 Progress in the detection of spin plasmons

Although the proposed time resolved MOKE measurement is applicable in theory, the expected spin plasmon features have not been observed in actual experiments. In our early attempts in the MOKE measurements, we have encountered a few technical problems which may cause large errors to the collected data.

First, according to the data sheet from the manufacturer, the THz emission intensity of the photoconductive emitter at 4THz was about an order of magnitude smaller than that at 0.5THz (the frequency where the emitter exhibits the strongest emission). This means that the intensity of the THz beam that we used to generate spin plasmons may not be strong enough for the later MOKE detection. We will be able to boost the spin plasmon signals for ~10 times by pushing the plasmon frequency to below 2THz. As was discussed in the last chapter, this may be challenging in terms of sample preparation.

The second problem is the identification of the distance. As was discussed in the previous section, we plan to scan the distance d (the distance from the gold grating coupler to the spot where the probe laser beam hits the sample). An optical imaging system is used to determine the spot where the probe laser hits the sample, and to minimize the spot size of the probe laser. However, due to the high power of the laser beam, the imaging camera will be saturated even when we filter the laser power to the lowest level. In a typical imaging attempts, the beam spot size is estimated to be ~10 μm with an error of similar magnitude (the wavelength of the plasmon is 75 μm). This significantly reduces the resolution of a distance scan, and our ability in controlling the exact scanning position on the sample.

Secondly, the scan of the time delay is also limited by the temporal resolution. Based on the geometry of the beam line and parameters of the delay stage, the smallest

temporal resolution of the delay time scan is estimated to be ~ 60 fs, which is $\sim 1/4$ of the periodicity of the plasmon wave. This temporal resolution is still far from enough to observe the features of the spin plasmons.

5.4 Summary

In this chapter, we introduced the detailed THz excitation MOKE measurement setup for the direct observation of spin plasmons in TIs. A commercial photoconductive THz emitter was used to generate a THz beam (0.5THz~4THz) for the excitation of spin plasmons. A time resolved MOKE setup was used to detect the spin features of the plasmons excited by the THz beam. However, persuasive evidences have not been found in our experiments with this setup. Three technical problems that we encountered in the measurements were discussed. These problems were believed to be the major limitations of our early attempts. Future works can be proposed based on these problems, which will be covered in the next chapter.

Chapter 6

CONCLUSIONS AND FUTURE WORKS

Previous chapters of this dissertation mainly focused on the research works in search of the spin plasmons in topological insulators. We briefly reviewed some basic concepts of topological insulators and spin plasmons in chapter 1, and introduced the growth, characterization, and fabrication techniques that were used in the whole dissertation in chapter 2.

We started the discussion with the optimization of the epitaxial growth of topological insulators in chapter 3. Two ways to reduce the carrier density of epitaxial TI films were discussed: by growing TI $\text{Bi}_2(\text{Se}_{1-x}\text{Te}_x)_3$ ternary alloys and by growing TI Bi_2Se_3 on $(\text{Bi}_{1-x}\text{In}_x)_2\text{Se}_3$ buffer layers. The growth of $\text{Bi}_2(\text{Se}_{1-x}\text{Te}_x)_3$ did not turn out to be as ideal as expected, while the Bi_2Se_3 samples grown on $(\text{Bi}_{1-x}\text{In}_x)_2\text{Se}_3$ buffers exhibited a significantly reduced carrier density. This optimized growth method was then used in the later discussions of TI plasmons.

In chapter 4, we first demonstrated the optical properties of the epitaxially grown $(\text{Bi}_{1-x}\text{In}_x)_2\text{Se}_3$ films, providing a good understanding of the optical responses of such a material system. We then discussed the launching and observation of the Dirac plasmon polaritons in TI thin films, which is a prerequisite step for the observation of spin plasmons in TIs. This is also the first demonstration of a propagating Dirac plasmons in topological insulators.

Chapter 5 discussed the method to directly detect the spin plasmons in TIs. A photoconductive THz emitter was used to excite the spin plasmons, and a time

resolved MOKE setup was used to measure the spin features of the plasmons. Promising evidences for the existence of spin plasmons in TIs have been found in the MOKE measurements. The major technical challenges of the current measurement method were discussed.

Future works

Following this path, we could propose a few improvements in the MOKE detection of the spin plasmons for future works. Based on the discussions in chapter 5, an obvious way to improve the signal-to-noise ratio is to lower the TI plasmon frequency. According to the data sheet from the manufacturer, the THz emission intensity of the photoconductive emitter at 4THz was about an order of magnitude smaller than that in the range of 0.2THz~2THz, with 0.5THz being the frequency where the emitter exhibits the strongest emission. Hence, moving the plasmon frequency to the range of 0.2THz~2THz will significantly enhance the efficiency of the plasmon excitation.

We can figure out the grating coupler periodicity if we revisit eq. 4.1 and eq. 4.11.

$$q = \frac{\pi}{W} \quad \text{Eq. 4.1}$$

$$\omega_{Dirac}^2 = \frac{e^2}{4\varepsilon_0\varepsilon_r} \frac{v_F\sqrt{2\pi n_D}}{h} \frac{q}{\varepsilon_{eff} + q\varepsilon_{TI}d} \quad \text{Eq. 4.11}$$

Based on these equations, the grating coupler periodicity for plasmon frequencies 0.2THz, 0.5THz, and 2THz are 155.7 μm , 28.8 μm , and 4.8 μm , respectively. This frequency range was not covered in the discussion of the coupled Dirac plasmon due to the dominant effect of the Bi₂Se₃ phonon mode at 2THz. However, since we expect limited effect from the phonon modes in the MOKE

measurements, we could potentially fabricate samples aiming for the plasmon frequency in this range.

Furthermore, improvements of the optical components could also help us improve the resolution of the MOKE measurements. For example, a delay stage with a finer step size would help us improve the temporal resolution, and a better imaging setup would help us determine the probe laser spot size and position more precisely.

Despite the technical challenges arising from the THz excitation MOKE measurement setup, we believe that the significance of observing the TI spin plasmons still hold strong. The observation of the spin plasmons in TIs will not only complete our understandings of the TI plasmons, but also open up the possibilities to devices with both terahertz responses as well as memory and computing abilities.

REFERENCES

1. R. F. Oulton, V. J. Sorger, D. A. Genov, D. F. P. Pile, and X. Zhang, *Nat. Photonics*, **2**, 8(2008).
2. X. Lin and X. Huang, *Opt. Lett.*, **33**, 23(2008).
3. D. Ansell, I. P. Radko, Z. Han, F. J. Rodriguez, S. I. Bozhevolnyi, and A. N. Grigorenko, *Nat. Commun.*, **6**:8846(2015).
4. F. Rana, *IEEE Trans. Nanotechnol.*, **7**, 1(2008).
5. G. Acuna, S. F. Heucke, F. Kuchler, H. T. Chen, A. J. Taylor, and R. Kersting, *Opt. Express*, **16**, 23(2008).
6. L. Ju *et al.*, *Nat. Nanotechnol.*, **6**, 10(2011).
7. P. H. Siegel, *IEEE Trans. Microw. Theory Tech.*, **50**, 3(2002).
8. S. S. Dhillon, *J. Phys. D Appl. Phys.*, **50**, 043001(2017).
9. S. A. Wolf, A. Y. Chtchelkanova, and D. M. Treger, *IBM J. Res. Dev.*, **50**, 1(2006).
10. M. N. Baibich, J. M. Broto, A. Fert, F. Nguyen Van Dau, and F. Petroff, *Phys. Rev. Letts*, **61**, 21(1988).
11. G. Binasch, P. Grünberg, F. Saurenbach, and W. Zinn, *Phys. Rev. B*, **39**, 7(1989).
12. J. A. Katine, F. J. Albert, and R. A. Buhrman, *Phys. Rev. Lett.*, **84**, 1(2000).
13. J. Linder and J. W. A. Robinson, *Nat. Phys.*, **11**, 4(2015).
14. A. Fert, *Rev. Mod. Phys.*, **80**, 4(2008).
15. K. Uchida *et al.*, *Nat. Commun.*, **6**:5910(2015).
16. W. L. Barnes, A. Dereux, and T. W. Ebbesen, *Insight Rev. Artic.*, **424**(2003).

17. L. I. Magarill, A. V Chaplik, and M. V Éntin, *J. Exp. Theor. Phys.*, **92**, 1(2001).
18. A. O. Govorov, *Phys. Rev. B*, **52**, 155322(2010).
19. X. F. Wang, *Phys. Rev.B*, **72**, 085317(2005).
20. B. A. Bernevig and S. Zhang, *Phys. Rev. Lett.*, **96**, 106802(2006).
21. M. Z. Hasan and C. L. Kane, *Rev. Mod. Phys.*, **82**, 4(2010).
22. I. Appelbaum, H. D. Drew, and M. S. Fuhrer, *Appl. Phys. Lett.*, **98**, 023103(2011).
23. A. R. Akhmerov, J. Nilsson, and C. W. J. Beenakker, *Phys. Rev. Lett.*, **102**, 216404(2009).
24. T. Stauber, and G. Gómez-Santos, *Phys. Rev. B*, **88**, 205427(2013).
25. T. Stauber, *J. Phys. Condens. matter*, **26**, 123201(2014).
26. K. V. Klitzing, G. Dorda, and M. Pepper, *Phys. Rev. Lett.*, **45**, 6(1980).
27. D. J. Thouless, M. Kohmoto, M. P. Nightingale, and M. den Nijs, *Phys. Rev. Letts*, **49**, 6(1984).
28. M. Nakahara, *Geometry, Topology and Physics, Second Edition*(Taylor&Francis, 2003).
29. C. L. Kane and E. J. Mele, *Phys. Rev. Lett.*, **95**, 22(2005).
30. B. Andrei Bernevig, T. L. Hughes, and S. Zhang, *Science* **314**, 15(2006).
31. M. König, et. al, *Science* **318**, 766(2010).
32. T. Ginley, Y. Wang, Z. Wang, and S. Law, *MRS Commun.*, **8**, 3, (2018).
33. H. Zhang, C. Liu, X. Qi, X. Dai, Z. Fang, and S. Zhang, *Nat. Phys.*, **5**, 438(2009).
34. D. Hsieh, D. Qian, L. Wray, Y. S. Hor, R. J. Cava, and M. Z. Hasan, *Nature* **452**, 970(2008).
35. Y. Xia *et al.*, *Nat. Phys.*, **5**, 398(2009).

36. T. Ginley, Y. Wang, and S. Law, *Crystals*, **6**, 11(2016).
37. D. Pines and D. Bohm, *Phys. Rev.*, **85**, 2(1952).
38. D. Bohm and D. Pines, *Phys. Rev.*, **92**, 3(1953).
39. D. Pines, *Phys. Rev.*, **92**, 3(1953).
40. S. Law, V. Podolskiy, and D. Wasserman, *Nanophotonics*, **2**, 2(2013).
41. H. M. Hiep *et al.*, *Sci. Technol. Adv. Mater.*, **8**, 4(2007).
42. E. Ozbay, *Science* **311**, 189(2012).
43. T. Stauber, G. Gómez-Santos, and L. Brey, *Phys. Rev. B*, **88**, 205407(2013).
44. T. Stauber, G. Gómez-Santos, and L. Brey, *ACS Photonics*, **4**, 12(2017).
45. Y. Lai, I. Lin, K. Wu, and J. Liu, *Nanomater. Nanotechnol.*, **4**, 13(2014).
46. P. Di Pietro *et al.*, *Nat. Nanotechnol.*, **8**, 556(2013).
47. M. Autore *et al.*, *ACS Photonics*, **2**, 1231(2015).
48. T. P. Ginley and S. Law, *Adv. Opt. Mater.*, **6**, 1800113(2018).
49. S. Raghu, S. B. Chung, X. Qi, and S. Zhang, *Phys. Rev. Lett.*, **104**, 116401(2010).
50. M. D. Johnson *et al.*, *Phys. Rev. Lett.*, **72**, 1(1994).
51. B. A. Joyce, *Reports Prog. Phys.*, **48**, 1637(1985).
52. T. P. Ginley and S. Law, *J. Vac. Sci. Technol. B*, **34**, 02L105(2016).
53. R. Köhrbrück, S. Munnix, D. Bimberg, E. C. Larkins, and J. S. Harris, *Appl. Phys. Lett.*, **54**, 623(1989).
54. D. Bimberg *et al.*, *Thin Solid Films*, **267**, 32(1995).
55. B. R. Bennett, R. Magno, J. B. Boos, W. Kruppa, and M. G. Ancona, *Solid. State. Electron.*, **49**, 1875(2005).
56. B. Heying, E. J. Tarsa, C. R. Elsass, P. Fini, S. P. DenBaars, and J. S. Speck, *J. Appl. Phys.*, **85**, 9(1999).

57. D. L. Rode, W. R. Wagner, and N. E. Schumaker, *Appl. Phys. Lett.*, **30**, 2(1977).
58. A. P. Mackenzie *et al.*, *Phys. Rev. B*, **58**, 20(1998).
59. D. G. Schlom, *APL Mater.*, **3**, 062403(2015).
60. R. A. Betts and C. W. Pitt, *Electron. Lett.*, **21**, 21(1985).
61. Y. Fukuda and Y. Kohama, *J. Cryst. Growth*, **81**, 451(1987).
62. Y. Zhu and J. Yang, *J. Phys. Conf. Ser. Ser.*, **864**, 012037(2017).
63. H. J. Liu *et al.*, *2D Mater.*, **2**, 034004(2015).
64. L. He, X. Kou, and K. L. Wang, *Phys. Status Solidi RRL*, **7**, 50(2013).
65. A. Pimpinelli and J. Villain, *Physics of Crystal Growth*(Cambridge University Press, 1998).
66. K. Oura, V. G. Lifshits, A. A. Saranin, A. V. Zotov, and M. Katayama, *Surface Science: An Introduction*(Springer, 2003).
67. A. Raviswaran, C. Liu, J. Kim, D. G. Cahill, and J. M. Gibson, *Phys. Rev. B - Condens. Matter Mater. Phys.*, **63**, 125314(2001).
68. J. Venables, *Introduction to Surface and Thin Film Processes*(Cambridge University Press, 2000).
69. D. Leonard, M. Krishnamurthy, S. Fafard, J. L. Merz, and P. M. Petroff, *J. Vac. Sci. Technol. B*, **12**, 2(1994).
70. A. Koma, K. Sunouchi, and T. Miyajima, *Microelectron. Eng.*, **2**, 129(1984).
71. L. A. Walsh and C. L. Hinkle, *Appl. Mater. Today*, **9**, 504(2017).
72. W. Braun, *Applied RHEED Reflection High Energy Electron Diffraction During Crystal Growth*(Springer-Verlag Berlin Heidelberg, 1999).
73. C. I. Fornari, P. H. O. Rappl, S. L. Morelhão, and E. Abramof, *J. Appl. Phys.*, **119**, 165303(2016).
74. L. F. Thompson, *An introduction to lithography in ACS symposium series*(American Chemical Society, 1983).

75. A. A. Ramadan, R. D. Gould, and A. Ashour, *Thin Solid Films*, **239**, 272(1994).
76. S. K. Mishra, S. Satpathy, and O. Jepsen, *J. Phys. Condens. Matter*, **9**, 461(1997).
77. V. B. Nascimento, V. E. De Carvalho, R. Paniago, E. A. Soares, L. O. Ladeira, and H. D. Pfannes, *J. Electron Spectros. Relat. Phenomena*, **104**, 99(1999).
78. C. H. Champness, and A. L. Kipling, *Can.J.Phys.*, **44**, 769(1966).
79. K. J. John, B. Pradeep, and E. Mathai, *Solid State Commun.*, **85**, 10(1993).
80. Y. R. Sapkota, and D. Mazumdar, *J. Appl. Phys.*, 124, 105306(2018).
81. L. Sun, Z. Lin, J. Peng, J. Weng, Y. Huang, and Z. Luo, *Sci. Rep.*, **4**, 4794(2014).
82. B. Pejova, and I. Grozdanov, *Thin Solid Films*, **408**, 6(2002).
83. X. Yang, X. Wang, and Z. Zhang, *J. Cryst. Growth*, **276**, 566(2005).
84. Y. Xia *et al.*, *Nat. Phys.*, **5**, 398(2009).
85. J. G. Checkelsky, Y. S. Hor, M. H. Liu, D. X. Qu, R. J. Cava, and N. P. Ong, *Phys. Rev. Lett.*, **103**, 246601(2009).
86. H. Peng *et al.*, *Nat. Mater.*, **9**, 225(2010).
87. T. Zhang *et al.*, *Phys. Rev. Lett.*, **103**, 266803(2009).
88. Y. Zhang *et al.*, *Nat. Phys.*, **6**, 584(2010).
89. C. Chang *et al.*, *Science*, **340**, 167(2013).
90. C. Z. Chang *et al.*, *Spin*, **1**, 1(2011).
91. Z. Zeng *et al.*, *AIP Adv.*, **3**, 072112(2013).
92. X. He *et al.*, *Appl. Phys. Lett.*, **101**, 123111(2012).
93. C. I. Fornari, P. H. O. Rappl, S. L. Morelhão, and E. Abramof, *J. Appl. Phys.*, **119**, 165303(2016).

94. C. Weyrich *et al.*, *J. Phys. Condens. Matter*, **28**, 495501(2016).
95. N. V. Tarakina *et al.*, *Adv. Mater. Interfaces*, **1**, 1400134(2014).
96. A. Richardella *et al.*, *Appl. Phys. Lett.*, **97**, 262104(2010).
97. S. Schreyeck *et al.*, *Appl. Phys. Lett.*, **102**, 041914(2013).
98. J. Wang *et al.*, *Phys. Rev. B.*, **83**, 245438(2011).
99. A. Hashibon, and C. Elsässer, *Phys. Rev. B*, **84**, 144117(2011).
100. G. R. Miller, and C. Y. Li, “*J. Phys. Chem. Solids*, **26**, 173(1965).
101. J. Navrátil, Z. Starý, and T. Plecháček, *Mater. Res. Bull.*, **31**, 12(1996).
102. H. Zou, D. M. Rowe, and G. Min, *J. Cryst. Growth*, **222**, 82(2001).
103. M. Goto, M. Sasaki, Y. Xu, T. Zhan, Y. Isoda, and Y. Shinohara, *Appl. Surf. Sci.*, **407**, 405(2017).
104. M. Neupane *et al.*, *Phys. Rev. B*, **88**, 165129(2013).
105. Z. Ren, A. A. Taskin, S. Sasaki, K. Segawa, and Y. Ando, *Phys. Rev. B*, **82**, 241306(2010).
106. J. H. Dycus *et al.*, *Microsc. Microanal.*, **21**, 946(2015).
107. Y. Wang, T. P. Ginley, C. Zhang, and S. Law, *J. Vac. Sci. & Technol B*, **35**, 02B106(2017).
108. H. Maaß *et al.*, *J. Appl. Phys.*, **116**, 193708(2014).
109. Y. Tung *et al.*, *J. Appl. Phys.*, **119**, 055303(2016).
110. Y. Chen, G. Brill, and N. K. Dhar, *J. Cryst. Growth*, **252**, 270(2003).
111. F. S. Turco-Sandroff *et al.*, *J. Cryst. Growth*, **111**, 762(1991).
112. Y. Wang, T. P. Ginley, C. Zhang, and S. Law, *J. Vac. Sci. & Technol B*, **35**, 02B106(2017).
113. H. D. Li *et al.*, *New J. Phys.*, **12**, 103038(2010).

114. N. Bansal, Y. S. Kim, M. Brahlek, E. Edrey, and S. Oh, *Phys. Rev. Lett.*, **109**, 116804(2012).
115. S. E. Harrison, S. Li, Y. Huo, B. Zhou, Y. L. Chen, and J. S. Harris, *Appl. Phys. Lett.*, **102**, 171906(2013).
116. L. Wu *et al.*, *Nat. Phys.*, **9**, 7(2013).
117. M. Brahlek, N. Koirala, M. Salehi, N. Bansal, and S. Oh, *Phys. Rev. Lett.*, **113**, 026801(2014).
118. Z. Y. Wang, X. Guo, H. D. Li, T. L. Wong, N. Wang, and M. H. Xie, *Appl. Phys. Lett.*, **99**, 023112(2011).
119. Y. Zhao *et al.*, *Nano Lett.*, **14**, 5244(2014).
120. N. Koirala *et al.*, *Nano Lett.*, **15**, 8245(2015).
121. H. D. Lee *et al.*, *Thin Solid Films*, **556**, 322(2014).
122. M. Brahlek *et al.*, *Phys. Rev. Lett.*, **109**, 186403(2012).
123. C. Julien, M. Eddrief, M. Balkanski, E. Hatzikraniotis, and K.Kambas, *Phys. Stat. Sol.*, **88**, 687(1985).
124. N. D. Raranskii, V. N. Balazyuk, Z. D. Kovalyuk, N. I. Mel’Nik, and V. B. Gevik, “*Inorg. Mater.*”, **47**, 11(2011).
125. J. Jasinski *et al.*, *Appl. Phys. Lett.*, **81**, 4356(2002).
126. Y. Wang, T. P. Ginley, and S. Law, *J. Vac. Sci. Technol. B*, **36**, 02D101(2018).
127. Y. Liu, M. Weinert, and L. Li, *Phys. Rev. Lett.*, **108**, 115501(2012).
128. Y. Wang and S. Law, *Opt. Mater. Express*, **8**, 9(2018).
129. J. Tauc, *Mater. Res. Bull.*, **3**, 37(1968).
130. I. A. Nechaev *et al.*, *Phys. Rev. B*, **87**, 121111(2013).
131. S. Kim *et al.*, *Phys. Rev. Lett.*, **107**, 056803(2011).
132. C. Julien, A. Chevy, and D. Siapakas, *Phys. stat. sol.*, **118**, 553(1990).

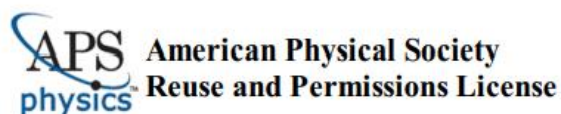
133. G. Almeida *et al.*, *J. Am. Chem. Soc.*, **139**, 8(2017).
134. N. Balakrishnan *et al.*, *2D Mater*, **3**, 025030(2016).
135. W. Li, F. P. Sabino, F. Crasto De Lima, T. Wang, R. H. Miwa, and A. Janotti, *Phys. Rev. B*, **94**, 165134(2018).
136. J. Hao, and L. Zhou, *Phys. Rev. B*, **77**, 094201(2008).
137. M. Schubert, T. E. Tiwald, C. W. Herzinger, *Phys. Rev. B*, **61**, 12(2013).
138. D. Culcer, E. H. Hwang, T. D. Stanescu, and S. Das Sarma, *Phys. Rev. B*, **82**, 155457(2010).
139. D. Kim *et al.*, *Nat. Phys.*, **8**, 459(2012).
140. W. Richter, H. Köhler, and C. R. Becker, *Phys. Stat.Sol b*, **84**, 619(1977).
141. M. Stordeur, K. K. Ketavonc, A. Priemuth, H. Sobotta, and V. Riede, *Phys. Stat. Sol. b*, **169**, 505(1992).
142. K. Kambas, and J. Spyridelis, *Mat.Res.Bull.*, **13**, 7(1978).
143. W. Gao *et al.*, *Nano Lett.*, **13**, 3698(2013).
144. I. Brener, D. Dykaar, A. Frommer, L. Pfeiffer, and K. West, *Opt. Letts.*, **21**, 23(1996).
145. G. Zhao, R. N. Schouten, N. Van Der Valk, W. T. Wenckebach, and P. C. M. Planken, *Rev. Sci. Instrum.*, **73**, 4(2002).
146. X. C. Zhang, B. B. Hu, J. T. Darrow, and D. H. Auston, *Appl. Phys. Lett.*, **56**, 11(1990).
147. P. H. Siegel, *IEEE Trans. Microw. Theory Tech.*, **50**, 3(2002).
148. G. Segschneider *et al.*, *Phys. Rev. B*, **65**, 125205(2002).
149. Y. C. Shen, P. C. Upadhyya, E. H. Linfield, H. E. Beere, and A. G. Davies, *Appl. Phys. Lett.*, **83**, 15(2003).
150. J. Kerr, *Phil. Mag. S.*, **3**, 19(1877).
151. P. Weinberger, *Philos. Mag. Lett.*, **88**, 12(2008).

152. K. Kayanuma *et al.*, *Opt. Data Storage*, **1316**, 35(1990).
153. N. O. Urs *et al.*, *AIP Adv.*, **6**, 055605(2016).
154. J. Y. Bigot, M. Vomir, and E. Beaurepaire, *Nat. Phys.*, **5**, 515(2009).
155. R. Mondal, M. Berritta, and P. M. Oppeneer, *J. Phys. Condens. Matter*, **29**, 194002(2017).
156. K. D. Lee, J. Kim, J. Jeong, D. Kim, and S. Shin, *J. Korean Phys. Soc.*, **49**, 6(2006).

Appendix

FIGURE REPRINT PERMISSION

Permission for figure 1.1



23-Jul-2020

This license agreement between the American Physical Society ("APS") and Yong Wang ("You") consists of your license details and the terms and conditions provided by the American Physical Society and SciPris.

Licensed Content Information

License Number:	RNP/20/JUL/028694
License date:	23-Jul-2020
DOI:	10.1103/RevModPhys.82.3045
Title:	Colloquium
Author:	M. Z. Hasan and C. L. Kane
Publication:	Reviews of Modern Physics
Publisher:	American Physical Society
Cost:	USD \$ 0.00

Request Details

Does your reuse require significant modifications:	No
Specify intended distribution locations:	United States
Reuse Category:	Reuse in a thesis/dissertation
Requestor Type:	Student
Items for Reuse:	Figures/Tables
Number of Figure/Tables:	1
Figure/Tables Details:	Figure 1
Format for Reuse:	Electronic

Information about New Publication:

University/Publisher:	University of Delaware
Title of dissertation/thesis:	BRIDGING BETWEEN PLASMONICS AND SPINTRONICS: THE SPIN PLASMONS IN TOPOLOGICAL INSULATORS
Author(s):	Yong Wang
Expected completion date:	Jul. 2020

License Requestor Information

Name:	Yong Wang
Affiliation:	Individual
Email Id:	yongw@udel.edu
Country:	United States

Permission for figure 1.2

THE AMERICAN ASSOCIATION FOR THE ADVANCEMENT OF SCIENCE LICENSE TERMS AND CONDITIONS

Jul 23, 2020

This Agreement between Dr. Yong Wang ("You") and The American Association for the Advancement of Science ("The American Association for the Advancement of Science") consists of your license details and the terms and conditions provided by The American Association for the Advancement of Science and Copyright Clearance Center.

License Number	4874940241298
License date	Jul 23, 2020
Licensed Content Publisher	The American Association for the Advancement of Science
Licensed Content Publication	Science
Licensed Content Title	Quantum Spin Hall Insulator State in HgTe Quantum Wells
Licensed Content Author	Markus König,Steffen Wiedmann,Christoph Brüne,Andreas Roth,Hartmut Buhmann,Laurens W. Molenkamp,Xiao-Liang Qi,Shou-Cheng Zhang
Licensed Content Date	Nov 2, 2007
Licensed Content Volume	318
Licensed Content Issue	5851
Volume number	318
Issue number	5851
Type of Use	Thesis / Dissertation
Requestor type	Scientist/individual at a research institution
Format	Electronic
Portion	Text Excerpt
Number of pages requested	1
Title	BRIDGING BETWEEN PLASMONICS AND SPINTRONICS THE SPIN PLASMONS IN TOPOLOGICAL INSULATORS
Institution name	University of Delaware
Expected presentation date	Jul 2020
Portions	Image in Author's summary
Requestor Location	Dr. Yong Wang 127 the Green 201 Dupont Hall NEWARK, DE 19716 United States Attn: University of Delaware
Total	0.00 USD

Permission for figure 1.4

SPRINGER NATURE LICENSE TERMS AND CONDITIONS

Jul 23, 2020

This Agreement between Dr. Yong Wang ("You") and Springer Nature ("Springer Nature") consists of your license details and the terms and conditions provided by Springer Nature and Copyright Clearance Center.

License Number	4874940696148
License date	Jul 23, 2020
Licensed Content Publisher	Springer Nature
Licensed Content Publication	Nature Physics
Licensed Content Title	Topological insulators in Bi ₂ Se ₃ , Bi ₂ Te ₃ and Sb ₂ Te ₃ with a single Dirac cone on the surface
Licensed Content Author	Haijun Zhang et al
Licensed Content Date	May 10, 2009
Type of Use	Thesis/Dissertation
Requestor type	academic/university or research institute
Format	electronic
Portion	figures/tables/illustrations
Number of figures/tables/illustrations	1
High-res required	no
Will you be translating?	no
Circulation/distribution	1 - 29
Author of this Springer Nature content	no
Title	BRIDGING BETWEEN PLASMONICS AND SPINTRONICS THE SPIN PLASMONS IN TOPOLOGICAL INSULATORS
Institution name	University of Delaware
Expected presentation date	Jul 2020
Portions	Figure 4
Requestor Location	Dr. Yong Wang 127 the Green 201 Dupont Hall NEWARK, DE 19716 United States Attn: University of Delaware
Total	0.00 USD

Permission for figure 2.8

AIP PUBLISHING LICENSE TERMS AND CONDITIONS

Jul 23, 2020

This Agreement between Dr. Yong Wang ("You") and AIP Publishing ("AIP Publishing") consists of your license details and the terms and conditions provided by AIP Publishing and Copyright Clearance Center.

License Number	4874950712903
License date	Jul 23, 2020
Licensed Content Publisher	AIP Publishing
Licensed Content Publication	Journal of Applied Physics
Licensed Content Title	Structural properties of Bi ₂ Te ₃ topological insulator thin films grown by molecular beam epitaxy on (111) BaF ₂ substrates
Licensed Content Author	Celso I. Fornari, Paulo H. O. Rappl, Sérgio L. Morelhão, et al
Licensed Content Date	Apr 28, 2016
Licensed Content Volume	119
Licensed Content Issue	16
Type of Use	Thesis/Dissertation
Requestor type	Student
Format	Electronic
Portion	Figure/Table
Number of figures/tables	1
Title	BRIDGING BETWEEN PLASMONICS AND SPINTRONICS THE SPIN PLASMONS IN TOPOLOGICAL INSULATORS
Institution name	University of Delaware
Expected presentation date	Jul 2020
Portions	Figure 2
Requestor Location	Dr. Yong Wang 127 the Green 201 Dupont Hall NEWARK, DE 19716 United States Attn: University of Delaware
Total	0.00 USD
Terms and Conditions	

Permission for figure 3.2, 3.5, 3.6, and 3.7

AIP PUBLISHING LICENSE TERMS AND CONDITIONS

Jul 23, 2020

This Agreement between Dr. Yong Wang ("You") and AIP Publishing ("AIP Publishing") consists of your license details and the terms and conditions provided by AIP Publishing and Copyright Clearance Center.

License Number	4874951268172
License date	Jul 23, 2020
Licensed Content Publisher	American Vacuum Society
Licensed Content Publication	Journal of Vacuum Science & Technology B
Licensed Content Title	Transport properties of Bi ₂ (Se _{1-x} Tex) ₃ thin films grown by molecular beam epitaxy
Licensed Content Author	Yong Wang, Theresa P. Ginley, Chiyu Zhang, et al
Licensed Content Date	Mar 1, 2017
Licensed Content Volume	35
Licensed Content Issue	2
Type of Use	Thesis/Dissertation
Requestor type	Student
Format	Electronic
Portion	Figure/Table
Number of figures/tables	2
Title	BRIDGING BETWEEN PLASMONICS AND SPINTRONICS THE SPIN PLASMONS IN TOPOLOGICAL INSULATORS
Institution name	University of Delaware
Expected presentation date	Jul 2020
Portions	Figure 3 and figure 4
Requestor Location	Dr. Yong Wang 127 the Green 201 Dupont Hall NEWARK, DE 19716 United States Attn: University of Delaware
Total	0.00 USD

Permission for figure 3.14, 3.15, 3.16, and 3.17

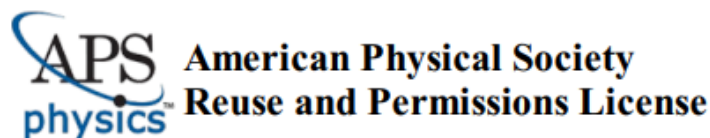
AIP PUBLISHING LICENSE TERMS AND CONDITIONS

Jul 23, 2020

This Agreement between Dr. Yong Wang ("You") and AIP Publishing ("AIP Publishing") consists of your license details and the terms and conditions provided by AIP Publishing and Copyright Clearance Center.

License Number	4874951442362
License date	Jul 23, 2020
Licensed Content Publisher	American Vacuum Society
Licensed Content Publication	Journal of Vacuum Science & Technology B
Licensed Content Title	Growth of high-quality Bi ₂ Se ₃ topological insulators using (Bi _{1-x} In _x) ₂ Se ₃ buffer layers
Licensed Content Author	Yong Wang, Theresa P. Ginley, Stephanie Law
Licensed Content Date	Mar 1, 2018
Licensed Content Volume	36
Licensed Content Issue	2
Type of Use	Thesis/Dissertation
Requestor type	Original Author Representative
Format	Electronic
Portion	Figure/Table
Number of figures/tables	4
Title	BRIDGING BETWEEN PLASMONICS AND SPINTRONICS THE SPIN PLASMONS IN TOPOLOGICAL INSULATORS
Institution name	University of Delaware
Expected presentation date	Jul 2020
Portions	Figure 2, 3, 4, 5
Requestor Location	Dr. Yong Wang 127 the Green 201 Dupont Hall NEWARK, DE 19716 United States Attn: University of Delaware
Total	0.00 USD

Permission for figure 4.1



23-Jul-2020

This license agreement between the American Physical Society ("APS") and Yong Wang ("You") consists of your license details and the terms and conditions provided by the American Physical Society and SciPris.

Licensed Content Information

License Number:	RNP/20/JUL/028695
License date:	23-Jul-2020
DOI:	10.1103/PhysRevLett.104.116401
Title:	Collective Modes of a Helical Liquid
Author:	S. Raghu et al.
Publication:	Physical Review Letters
Publisher:	American Physical Society
Cost:	USD \$ 0.00

Request Details

Does your reuse require significant modifications:	No
Specify intended distribution locations:	United States
Reuse Category:	Reuse in a thesis/dissertation
Requestor Type:	Student
Items for Reuse:	Figures/Tables
Number of Figure/Tables:	1
Figure/Tables Details:	Figure 2
Format for Reuse:	Electronic

Information about New Publication:

University/Publisher:	University of Delaware
Title of dissertation/thesis:	BRIDGING BETWEEN PLASMONICS AND SPINTRONICS THROUGH SPIN PLASMONS IN TOPOLOGICAL INSULATORS
Author(s):	Yong Wang
Expected completion date:	Jul. 2020

License Requestor Information

Name:	Yong Wang
Affiliation:	Individual
Email Id:	yongw@udel.edu
Country:	United States